Dylan Mickael Marques

Bachelor degree in Sciences of Physics Engineering

Ellipsometry and differential interference contrast microscopic imaging of cellular exo- and endocytosis: modelling and experiments

Dissertation submitted in partial fulfillment
of the requirements for the degree of

Master of Science in
Physics Engineering

Adviser: Prof Dr Ana Gomes Silva,
Assistant professor,
Universidade Nova de Lisboa

Co-adviser: Dr Pieter De Beule,
Group leader,
International Iberian Nanotechnology Laboratory

FACULDADE DE
CIÊNCIAS E TECNOLOGIA
UNIVERSIDADE NOVA DE LISBOA

September, 2017

Ellipsometry and differential interference contrast microscopic imaging of cellular exo- and endocytosis: modelling and experiments

This document was created using the (pdf)LaTeX processor, based in the "novathesis" template[1], developed at the Dep. Informática of FCT-NOVA [2].
[1] https://github.com/joaomlourenco/novathesis [2] http://www.di.fct.unl.pt

Acknowledgements

I want to start this manuscript to express my gratitude to some important persons that directly or indirectly were important for the realization of my master thesis.

To Dr Pieter De Beule, group leader of the Applied Nano-Optics group at Iberian International Nanotechnology Laboratory (INL), I want to acknowledge him for all the support that he gave me during these last months. In special for helping me in the development not only of the work but also in all my soft skills that will be fundamental in my future. I also want to recognize him for all the opportunities that he gave me during my master's project.

To Prof Dr Ana Gomes Silva, I want to highlight her importance in the project and express my gratitude for always being available and for the multiple useful discussions over these last months.

To Dr Adelaide Miranda, I want to say thanks not only for all the precious work made by her and for her expertise which was indispensable for this project but also for all the support and positive attitude that she gave me since the beginning.

To Dr Peter R. T. Munro, which kindly integrated the project bringing his expertise in the modulation field, I want to acknowledge him for all the support and indispensable help provided and also for gently receiving me in London.

To Dr Aline Fernandes, Dr Ana Gomez and Dr Rosana Alves, which are members of the Applied Nano-Optics group, for all the support provided and for always being available.

To Dr Thomas Germer, who developed the SCATMECH library, for his help regarding how to use it.

I also want to recognize INL for all the financial support provided as well the opportunity to elaborate my master's project in their facilities.

From a more personal point of view, I want to acknowledge all my friends which gave me an indispensable support not only during this work but during these five years. A big thanks to them. I want to highlight my friend Ricardo Adão for being a great flatmate during these six months and, in partnership with João Fernandes, for making my time in Braga much more enjoyable.

At last but not least, I want to acknowledge my family for always being here since the day one. I want to mention my brother Christopher Marques for the wise advices that he gave me during this 23 years and for always being the helpful and respectful person that

he is. And in special to my parents which always supported me even when the mood was not the best and principally for transmitting me my values that make me the person that I am today.

Abstract

In this work it is presented a solution to Maxwell's equations for core-shell nanoparticle scattering near an isotropic substrate covered with an anisotropic thin film, based on an extension of the Bobbert-Vlieger (BV) solution for particle scattering near a substrate, delivering an exact solution in the near-field as well as far-field. It is applied successfully the developed scattering model to the calculation of light scattering on an optical model representing a lipid vesicle near a lipid bilayer, whereby the lipids are characterized through a uniaxial optical model. Hereby, it is paved the path for understanding quantitatively how light scatters during a cellular exo- or endocytosis event during microscopic observation taking into account lipid induced anisotropy. Through the application of ellipsometry angles it is effectively demonstrated that realistically small optical anisotropy values significantly alter far-field optical scattering in respect to an equivalent optical model for cellular endocytosis consisting of isotropic components only.

It is then calculated the impact of lipid-induced optical anisotropy on the experimental observation of exo- or endocytic microscopic imaging with e.g. Differential Interference Contrast (DIC) microscopy. Furthermore, it is integrated this extended BV scattering solution into a rigorous model of DIC image formation which allows for characterizing DIC, through simulation, as a tool for imaging of exo- or endocytosis events. It is also compared theoretical predictions with experimental high Numerical Aperture (NA) dic imaging of dielectric oxide nanoparticles with organic shell.

Keywords: Optical properties of nanostructures, optical anisotropy, nanomedicine

Resumo

Neste trabalho é apresentada a solução das equações de Maxwell para nanopartículas cobertas com um filme fino perto de um substrato isotrópico coberto com um filme fino anisotrópico baseando-se numa extensão da solução de Bobbert-Vlieger (BV) para uma partícula perto de um substrato, obtendo-se a solução exata tanto para o *near-field* bem como o *far-field*. O modelo de dispersão da luz é aplicado para calcular a interação da luz com um modelo ótico que representa um liposoma perto da uma membrana lipídica, onde os lípidos são caracterizados através de um modelo ótico uniaxial. Desta forma, é possível perceber como a luz é dispersa durante a exo- ou endocitose observável ao microscópio tendo em conta a anisotropia dos lípidos. Considerando os ângulos de elipsometria é demonstrado que pequenos valores de anisotropia alteram significativamente o *far-field* disperso comparando com um modelo ótico de endocitose onde apenas se consideram materiais isotrópicos.

Também é calculado o impacto da anisotropia dos lípidos numa observação microscópica utilizando Differential Interference Contrast (DIC). Além disso, é integrado a extensão do modelo de BV num modelo rigoroso de DIC para caracterizar DIC como ferramenta de observação da exo- or endocitose. Os resultados teóricos são também comparados com resultados experimentais de nanopartículas de sílica cobertas com lípidos obtidos num DIC de elevada Numerical Aperture (NA).

Palavras-chave: Propriedades óticas de nanopartículas, anisotropia óptica, nanomedicina

Contents

List of Figures

List of Tables

Listings

Chapter 1

Introduction

1.1 Motivation

The absorption of matter by a living cell through invagination of its own membrane to form a vacuole, *i.e* endocytosis, and the inverse process where the cell ejects vesicles to the extracellular medium, *i.e* exocytosis, are fundamental process in biology. The control of these dynamics allows to improve medical treatment using for example drug delivery at specific tissues which can be achieve through vesicles as carrier for *in situ* delivery [1].

Unfortunately, *in-vivo* monitorization of endocytosis represents a formidable challenge in microscopy due to small dimensions and small contrast of the components involved and principally the short duration of the event. The techniques used nowadays require external fluorescent agents [2] which can be experimentally troublesome due to phenomena of photobleaching and blinking [3].

In 1952, Smith introduced the DIC white light microscopy [4] that was a few years later improved by Nomarski and Weill [5]. This new type of microscopy is a widely-applied contrast enhancement mechanism in optical microscopy for life sciences [6, 7] due that it is very sensitive to the introduction of phase change, in contrast to bright field observation that monitors intensity variations only.

Video-DIC microscopy is a powerfully tool for observation of cellular processes because it combines the DIC capacities with an appropriate frame rate [8]. However, since that DIC microscopy is based on the interference of two polarised beam it is expected that the Supported Lipid Bilayer (SLB) anisotropy impacts the image formation [9]. Monitor endocytosis employing video-DIC is a challenge since the vesicles size is close to the microscope resolution and it is not well understood how optical anisotropy influence the image formation.

Recently, Chowdhury et al. showed how Structured Illumination (SI) data can be used

to create a Three Dimensional (3D) Refractive Index (RI) cellular map [10]. The reconstruction is based upon the definition of an isotropic scattering potential introduced by Wolf in the 1960s [11]. This potential is derived assuming an isotropic sample RI distribution and so the impact of an anisotropic sample RI is currently not understood. Therefore, once more, a quantification of how small optical anisotropy amounts affects how light is scattered could help to understand better if approximate the cellular components to the optical isotropic case is valid or not.

1.2 State of the Art

Imaging both endocytosis and exocytosis is currently made using external fluorescent agents. Anantharam et al. proved that polarized resolved Total Internal Reflectance Fluorescence Microscopy (TIRFM) can be a powerful technique for exocytosis observation, in particular to characterize the localized topological changes that occurs in the plasma membrane [12]. Within a different context, Hines et al. demonstrated how combined fluorescence Confocal Microscopy (CM) and video-DIC microscopy data can jointly contribute to the study of dynamic membrane remodelling process during nerve growth [2].

Since the introduction of DIC microscopy, multiple theoretical models have been introduced over the years [13, 14]. More recently, Munro and Török elaborate a rigorously Nomarski DIC model under coherent illumination considering high NA lens [15] employing the diffraction theory of Wolf and Richards [16, 17]. The calculation of theoretical images is made using microscopes models associated with a sample model which solves the Maxwell equations considering a specific geometry.

From an optical point of view it is valid to approximate endocytosis by a sphere coated with a SLB which approach a substrate with a SLB above. The Maxwell equations for this type of geometries were solved by Bobbert et al. [18, 19]. However, this model was developed considering only isotropic materials which limits its application for this work. To study rigorously endocytosis it is important to develop an extension of the original Bobbert-Vlieger (BV) model. The scattering of a sphere with a uniaxial anisotropic shell has been considered by De Beule to consider isotropic particles with an anisotropic shell where he also quantified, theoretically, the anisotropy impact in a ellipsometry measurement [20]. Viegas et al. compared the extended BV model data with experimental data [21].

Considering De Beule's BV model, to rigorously model endocytosis, it is necessary a new extension to include the anisotropy of the substrate's SLB. With this new extension, all anisotropy sources of the geometry in study are considered being possible a to quantify its impact.

1.3 Objectives

By the statements presented above, it is clear that actually it is missing a quantification of how small anisotropy amounts affects light interaction. To overcome this, the goal of this work is to provide this quantification considering, as a case of study, the biological situation of a cell and the anisotropy of its membrane.

The main steps of this master thesis are the following:

- Elaboration of a DIC model based on Munro and Török model [15];
- Elaboration of an extension to De Beule's BV model [20] that considers a substrate with anisotropic thin films;
- Study, theoretically, how the SLB anisotropy impacts in how light is scattered;
- Study, theoretically and experimentally, how the SLB and its anisotropy impacts the DIC image formation;
- Study, theoretically, how the SLB anisotropy impacts the endocytosis imaging process in video-DIC.

1.4 Overview

This manuscript approaches the work developed within the master thesis program. It is divided in four main chapters each one describing a specific part of the work as explained in the next paragraphs.

The chapter 2 explains the theory behind the modulation made in this thesis. It is essentially divided in two main parts, the first explaining the transformations made in the BV model to consider anisotropic materials and the last one all the theory necessary to modulate a DIC microscope.

The chapter 3 focus in all materials and methods used. It is also explained there the programs used in the numerical implementations and all the verifications steps required. The experimental protocol with the respective sample preparation and characterization as well as the specifications of the equipment used are also presented in this chapter. At last, it is also mentioned how the data is analyzed to have a quantification of the impact in the image.

The chapter 4 discuss SLB impact in light interaction. More precisely, it is studied the anisotropy impact in the electric scattered far field presented as modelled ellipsometry data and then, it is evaluated the SLB impact in DIC images. It is also presented ellipsometry and DIC modelled data of endocytosis.

The chapter 5 mentions all the conclusions and some further work that could be interesting to developed considering the results obtained in this work.

Chapter 2

Theory and models

As mentioned in previous pages, one of the goals of this work is to implement a DIC model that allows the characterization of the SLB anisotropy impact in the image. For this purpose, it is referred in this chapter the theory necessary to implement this model. It is important to enhance that the objective of this chapter is not to provide a deep and complete background in optics but to provide the necessary theory from the application point of view.

In appendix A are indicated the conventions, nomenclature and coordinate systems used in this dissertation.

This chapter is divided in two main sections: first, the section 2.1 explain the bases of light scattering with small particles, proceeding to the section 2.2 where it is explained how to create a DIC model. In this last section, it is also explained how to combine the light scattering and DIC's theory.

2.1 Scattering theory

In this section, it is presented briefly the theory of light scattering when light interact with a small sphere which is near a substrate. The section 2.1.1 introduces some general polarimetry definitions. Then the section 2.1.2 refers to how the light interacts with anisotropic thin film (as SLB) while section 2.1.3 explain how light interacts with a isolated sphere. The section 2.1.4 refers to the light interaction with a sphere near a substrate (BV and Anisotropic Bobbert-Vlieger (ABV) model).

2.1.1 Polarimetry

The models implemented are developed using Jones formalism regarding the representation of electric fields and the description of the light propagation and its interaction with

optical components used in a microscope as well as with samples.

2.1.1.1 Jones vector

As well known, light is an electromagnetic wave in which the electric and magnetic fields propagate perpendicular to each other and perpendicular to the direction of propagation $\mathbf{n_k}$.

The Jones vector is a simple way to represent the electric field of a polarized light beam. In the coordinate system (x, y, z) the electric field of a polarized beam can be then described as a 3D vector with the respective components as in equation 2.1 [22]. The time and position dependence of the light is omitted for convenience.

$$\mathbf{E} = \begin{bmatrix} E_x\, \mathbf{n_x} \\ E_y\, \mathbf{n_y} \\ E_z\, \mathbf{n_z} \end{bmatrix} \tag{2.1}$$

In polarimetry the electric is commonly describe in the coordinate system (s, p, k) being the s component the part perpendicular to the Plane Of Incidence (POI) and the p component the part parallel to the same plane. The POI is defined as the plane that contains the incident and scattered Poynting vector. The k component is always 0 due that the electric field is perpendicular to the direction of propagation. Figure 2.1 represents both coordinate systems.

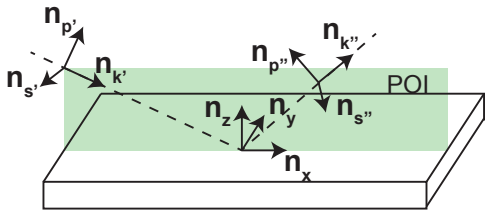

Figure 2.1: Representation of the (s, p, k) coordinate system of a light beam. The green plane represents the POI.

With the utilization of the unitary vectors of the respective coordinate systems it is possible to switch between them. The equation 2.2 allows to transform from the (s, p, k) to (x, y, z) coordinate system.

$$\begin{bmatrix} E_x\, \mathbf{n_x} \\ E_y\, \mathbf{n_y} \\ E_z\, \mathbf{n_z} \end{bmatrix} = E_s \mathbf{n_s} + E_p \mathbf{n_p} \tag{2.2}$$

The inverse transformation is represented in equation 2.3.

$$\begin{bmatrix} E_s\, \mathbf{n_s} \\ E_p\, \mathbf{n_p} \end{bmatrix} = \begin{bmatrix} \mathbf{E} \cdot \mathbf{n_s} \\ \mathbf{E} \cdot \mathbf{n_p} \end{bmatrix} \tag{2.3}$$

2.1.1.2 Jones Matrix

In this section, it is introduced the Jones matrix which consists in a mathematical representation of optical components or samples.

A Jones matrix's advantage is that allows the utilization of rotation matrix. That means that, if an optical component (such as polariser or compensator) is rotated relatively to the optical axis, mathematically in can be translate to the application of the rotation matrix to the respective Jones matrix (more detail and an example can be found in section 3.4 of reference [23]).

A Jones matrix is based on the Fresnel coefficients, which represent the ratio of the electric field's amplitude component a incident and scattered in the component b. The equation 2.4 consists in its mathematical representation.

$$f_{ab} = \frac{E_{sc,b}}{E_{i,a}} \tag{2.4}$$

A Fresnel coefficient consists in a complex number where the real part represents the amplitude scattered and the imaginary part the relative phase between the scattered and incident wave.

For example, considering the coordinate system (s, p, k), f_{ps} represents the ratio between the electric field amplitude scattered in the s component and the incident in the p component.

Considering the coordinate system (s, p, k) it makes sense to define four Fresnel coefficients which constitute the Jones matrix $\mathcal{J}$ represented in the equation 2.5.

$$\mathcal{J} = \begin{bmatrix} f_{pp} & f_{sp} \\ f_{ps} & f_{ss} \end{bmatrix} \tag{2.5}$$

It is also pertinent to highlight the fact that the Jones matrix depend in a set of parameters: wavelength, Angle Of Incidence (AOI), scattered angle, scatterer, ...

Another advantage of the Jones matrix is that allows to easily calculate the scattered electric field if it is multiplied by the Jones vector of the incident field, as in equation 2.6.

$$\mathbf{E_{sc}} = \mathcal{J}\mathbf{E_i} \tag{2.6}$$

2.1.1.3 Bidirectional scattered distribution function

A Bidirectional Scattered Distribution Function (BSDF) is a function used to characterize the light interaction with a scatterer. Taking into account the incoming direction of the beam and the outgoing direction of the scattered light, it returns the Fresnel coefficients which relate the incoming and outgoing electric field.

Figure 2.2 shows an example where an arbitrary scatterer scatters the light in multiple plane waves with different and specific directions.

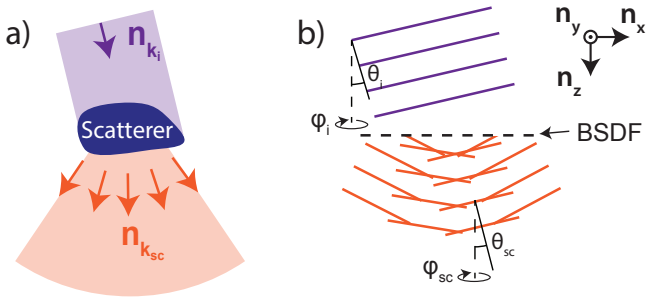

Figure 2.2: Representation of the BSDF for an arbitrary scatterer. a) and b) are the representation from a practical and mathematical point of view, respectively. $\mathbf{n}_{\mathbf{k}_i}$ and $\mathbf{n}_{\mathbf{k}_{sc}}$ stand for the incidence and scattered direction, respectively. They are related with the angles θ_i, ϕ_i, θ_{Sc} and ϕ_{Sc} by the equations 2.55 to 2.57 of page 26.

The BSDF is represented as a Jones matrix which is a function of the incident polar (θ_i) and azimuthal (ϕ_i) angles and the scattered polar (θ_{Sc}) and azimuthal (ϕ_{Sc}) angles, as equation 2.7 suggests.

$$\mathcal{J}(\theta_i,\phi_i,\theta_{Sc},\phi_{Sc}) = \begin{bmatrix} f_{pp}(\theta_i,\phi_i,\theta_{Sc},\phi_{Sc}) & f_{sp}(\theta_i,\phi_i,\theta_{Sc},\phi_{Sc}) \\ f_{ps}(\theta_i,\phi_i,\theta_{Sc},\phi_{Sc}) & f_{ss}(\theta_i,\phi_i,\theta_{Sc},\phi_{Sc}) \end{bmatrix} \tag{2.7}$$

It is more common to see the definition of Bidirectional Transmission Distribution Function (BTDF) and Bidirectional Reflection Distribution Function (BRDF). The BSDF consists in a more general function which take in account the reflection and transmission case, as equation 2.8 shows.

$$\text{BSDF} = \begin{cases} \text{BTDF}, & \text{if } 0 < \theta_{Sc} < \frac{\pi}{2} \\ \text{BRDF}, & \text{if } \frac{\pi}{2} < \theta_{Sc} < \pi \end{cases} \tag{2.8}$$

2.1.1.4 Ellipsometry angles

With the advances in nanotechnology and the increase in the use of thin-films, ellipsometry became a very common technique for characterization [24, 25]. This technique studies the polarized state of the scattered light when an incident polarized beam interacts with the respective sample.

Experimentally, the data is compared with theoretical models which allows to characterize many parameters of the sample: optical proprieties, thickness, roughness, etc.... The parameters are depended of the model used which is, of course, depended of the sample itself.

Traditionally, it is measured the angles Ψ and Δ which are related with the Fresnel coefficients presented above by the equation 2.9 [26].

$$\tan(\Psi)e^{i\Delta} = \frac{f_{pp}}{f_{ss}} \tag{2.9}$$

Ψ is related with the relative amplitude of the p and s component while Δ is related with relative phase between the p and s component. Traditionally an ellipsometry measurement is made resolving the AOI or the wavelength used.

The definition presented in equation 2.9 of the angles Ψ and Δ is only valid considering that f_{ps} and f_{sp} are null. If this condition is not satisfied there are more complex definitions for the ellipsometry angles but they are not required for the purpose of this work [23].

2.1.2 Polarized light interaction with anisotropic thin films

Materials with anisotropic optical properties (RI) are common in crystals, such as calcite, and in thin films of amphiphilic molecules like SLB [27].

An anisotropic material has different RI for each different direction that it is considered (N_x, N_y, N_z). An uniaxial material, as a SLB, has the same optical proprieties in two directions and a different one in the normal direction ($N_x = N_y = N_=$, $N_z = N_\perp$). The figure 2.3 represents the light interaction of a plane wave with this type of material.

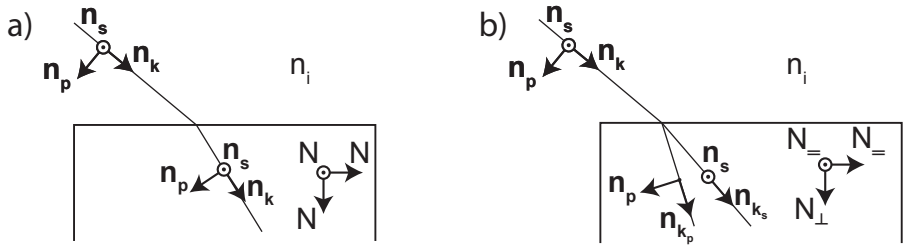

Figure 2.3: Representation of the light interaction with an isotropic material a) and an uniaxial anisotropic material b). It is here considered an isotropic material with RI as N and an uniaxial anisotropic material with RI as ($N_=$, $N_\perp$). The RI of the incident medium is considered as n_i.

It is possible to see in figure 2.3 that the p and s component experience different alteration in their directions due to their propagation in a medium with a different RI.

The anisotropy can be quantified by the birefringence of the material which is related with the difference between the anisotropic RI, according to the equation 2.10.

$$\Delta N = N_= - N_\perp \tag{2.10}$$

On a other hand, to quantify theoretically the effect of the anisotropy it can be defined an average RI based on the real parallel and perpendicular RI (equation 2.11) [28].

$$N_{avg} = \frac{2N_=}{3} + \frac{N_\perp}{3} \tag{2.11}$$

The definition of this average RI allows to have an isotropic reference to see the difference in how the light is scattered if it is considered or not the anisotropy.

2.1.2.1 Isotropic substrate with an anisotropic thin film above

The system that is studied in this work consists in small sphere coated with an anisotropic shell near an Isotropic Substrate with an Anisotropic Thin-Film above (ISATF). The total solution of this type of systems is mentioned in section 2.1.4. In this section, it is explained how to calculate the BSDF for an ISATF ($\mathcal{J}^{sub}$) which is required to calculate the BV solution.

The figure 2.4 represents a schematic of the light interaction with this of geometry.

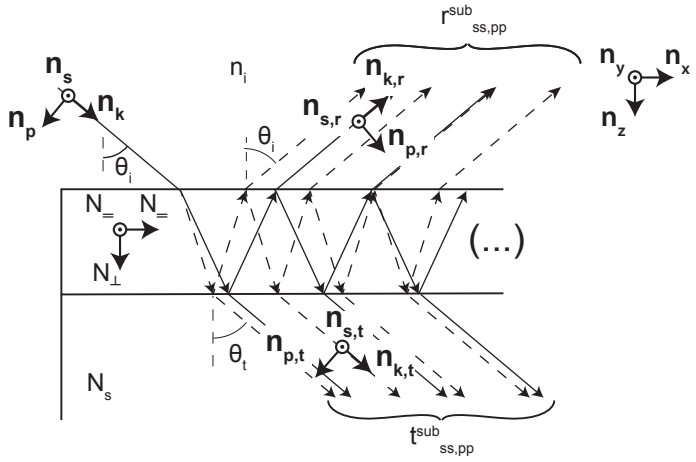

Figure 2.4: Representation of the light interaction with an ISATF. Based on reference [23].

As it well known in optics, each time that light suffers a change in the propagation medium, there is a part of the light which is transmitted and other reflected (section 1.5 of reference [29]). Dependent of the conditions, the light also suffers a change in its direction of propagation. The figure 2.4 represents these interaction for the system studied in this section. The figure also take in account the multiple reflections/transmissions and the interference between them.

In 1974, De Smet deduced the Fresnel coefficients for this type of geometry [30]. Considering an incident plane wave with direction θ_i, the light interaction in the interface of the incident medium with an uniaxial anisotropic layer is mathematically characterized by the Fresnel coefficients of equations 2.12 to 2.15.

$$r_{pp}^{ia} = \frac{N_= N_\perp \cos(\theta_i) - n_i (N_\perp^2 - n_i^2 \sin(\theta_i)^2)^{\frac{1}{2}}}{N_= N_\perp \cos(\theta_i) + n_i (N_\perp^2 - n_i^2 \sin(\theta_i)^2)^{\frac{1}{2}}} \tag{2.12}$$

$$r_{ss}^{ia} = \frac{n_i \cos(\theta_i) - (N_=^2 - n_i^2 \sin(\theta_i))^{\frac{1}{2}}}{n_i \cos(\theta_i) + (N_=^2 - n_i^2 \sin(\theta_i))^{\frac{1}{2}}} \tag{2.13}$$

$$t_{pp}^{ia} = \frac{2 n_i \cos(\theta_i)(n_i^2 \sin(\theta_i)^2 (N_=^2 - N_\perp^2) + N_\perp^4)^{\frac{1}{2}}}{N_\perp (N_\perp N_= \cos(\theta_i) + n_i (N_\perp^2 - n_i^2 \sin(\theta_i)^2)^{\frac{1}{2}}} \tag{2.14}$$

$$t_{ss}^{ia} = \frac{2 n_i \cos(\theta_i)}{n_i \cos(\theta_i) + (N_=^2 - n_i^2 \sin(\theta_i)^2)^{\frac{1}{2}}} \tag{2.15}$$

To calculate the direction that the light is propagating inside the substrate it is valid to use the Snell's law ($n_i \sin(\theta_i) = N_s \sin(\theta_t)$).

Equations 2.16 to 2.19 are the Fresnel coefficients in the interface between an uniaxial anisotropic thin film and the substrate.

$$r_{pp}^{as} = \frac{N_s(N_\perp^2 - n_i^2 \sin(\theta_t))^{\frac{1}{2}} - N_= N_\perp \cos(\theta_t)}{N_s(N_\perp^2 - n_i^2 \sin(\theta_t))^{\frac{1}{2}} + N_= N_\perp \cos(\theta_t)} \tag{2.16}$$

$$r_{ss}^{as} = \frac{(N_=^2 - N_s^2 \sin(\theta_t)^2)^{\frac{1}{2}} - N_s \cos(\theta_t)}{(N_=^2 - N_s^2 \sin(\theta_t)^2)^{\frac{1}{2}} + N_s \cos(\theta_t)} \tag{2.17}$$

$$t_{pp}^{as} = \frac{2N_\perp^2 N_= (N_\perp^2 - n_i^2 \sin(\theta_i)^2)^{\frac{1}{2}}}{(n_i^2 \sin(\theta_i)^2 (N_=^2 - N_\perp^2) + N_\perp^4)^{\frac{1}{2}} (N_= N_\perp \cos(\theta_t) + N_s (N_\perp^2 - n_i^2 \sin(\theta_i)^{\frac{1}{2}}))} \tag{2.18}$$

$$t_{ss}^{as} = \frac{2(N_=^2 - N_s^2 \sin(\theta_t)^2)^{\frac{1}{2}}}{(N_=^2 - N_s^2 \sin(\theta_t)^2)^{\frac{1}{2}} + N_s \cos(\theta_t)} \tag{2.19}$$

The phase variations of the p and s polarized waves inside the thin film can be calculate using the equations 2.20 and 2.21.

$$\beta_p = \frac{2\pi d}{\lambda} \frac{N_=}{N_\perp} (N_\perp^2 - n_i^2 \sin(\theta_i)^2)^{\frac{1}{2}} \tag{2.20}$$

$$\beta_s = \frac{2\pi d}{\lambda} (N_=^2 - n_i^2 \sin(\theta_i)^2)^{\frac{1}{2}} \tag{2.21}$$

Taking into account the interference of the multiple reflections and transmissions of the light (as suggested by figure 2.4) it is deduced the total solutions of the system represented by equations 2.22 to 2.25.

$$r_{pp}^{sub} = \frac{r_{pp}^{ia} + r_{pp}^{as} e^{i2\beta_p}}{1 + r_{pp}^{ia} r_{pp}^{as} e^{i2\beta_p}} \tag{2.22}$$

$$r_{ss}^{sub} = \frac{r_{ss}^{ia} + r_{ss}^{as} e^{i2\beta_s}}{1 + r_{ss}^{ia} r_{ss}^{as} e^{i2\beta_s}} \tag{2.23}$$

$$t_{pp}^{sub} = \frac{t_{pp}^{ia} + t_{pp}^{as} e^{i\beta_p}}{1 + t_{pp}^{ia} t_{pp}^{as} e^{i2\beta_p}} \tag{2.24}$$

$$t_{ss}^{sub} = \frac{t_{ss}^{ia} + t_{ss}^{as} e^{i\beta_s}}{1 + t_{ss}^{ia} t_{ss}^{as} e^{i2\beta_s}} \tag{2.25}$$

As mentioned before the goal of this section is to calculate the BSDF ($\mathcal{f}^{sub}$) for this geometry. To defined this function, it is required to defined the BRDF and BTDF. For this purpose, it is required to write the equations in function of the angles θ_{Sc} and ϕ_{Sc} defined as figure 2.2 suggests.

It is very well known in optics, that when an incident light beam with direction (θ_i, ϕ_i) interacts with an isotropic thin film above an isotropic substrate the reflected light is scattered as a plane wave with direction ($\pi - \theta_i$, ϕ_i). This is also valid for the case where

the thin film is an anisotropic uniaxial material [23]. Therefore, the BRDF can be defined as the equation 2.26.

$$\mathcal{R}^{sub} = \begin{cases} \begin{bmatrix} r_{pp}^{sub} & 0 \\ 0 & r_{ss}^{sub} \end{bmatrix}, & \text{if } \theta_{Sc} = \pi - \theta_i \wedge \phi_i = \phi_{Sc} \\ \begin{bmatrix} 0 & 0 \\ 0 & 0 \end{bmatrix}, & \text{otherwise} \end{cases} \tag{2.26}$$

On the other hand, it is required to define the BTDF to define the BSDF. For this purpose, it is also known that the direction of the transmitted light is given by the Snell's law therefore, applying the same rational that for the BRDF it is possible to arrive to the equation 2.27.

$$\mathcal{T}^{sub} = \begin{cases} \begin{bmatrix} t_{pp}^{sub} & 0 \\ 0 & t_{ss}^{sub} \end{bmatrix}, & \text{if } \theta_{Sc} = \sin^{-1}(\frac{n_i \sin(\theta_i)}{N_s}) \wedge \phi_i = \phi_{Sc} \\ \begin{bmatrix} 0 & 0 \\ 0 & 0 \end{bmatrix}, & \text{otherwise} \end{cases} \tag{2.27}$$

Using the definition of equation 2.8 it is completed the definition of the BSDF for this geometry ($\mathcal{F}^{sub}$).

2.1.3 Mie theory

In 1908, Mie solved the Maxwell's equations to find the solution of how a polarized light beam is scattered by a sphere [31]. This theory is not directly necessary for the work that is purposed but it is used as a comparison with the BV model to check if the implementation is correct.

A more detailed description of the Mie theory's deductions can be found in section 4.4.4 of reference [32].

Contrary to sections 2.1.4 and 2.1.2.1, in this section it is directly calculated the scattered far field (defined in section 2.2.1.2, page 19) instead of the BSDF. The relation between these two can be found in equation 2.46 present in page 22.

The figure 2.5 represents the geometry of the system modelled in this section.

Solving the Maxwell equations considering the boundary condition of a sphere, it is possible do calculate scattered far field $\mathbf{E_{sc}}^{\infty}(\theta_i, \phi_i, \theta_{Sc}, \phi_{Sc})$. For an incident plane wave that propagates parallel to the z axis, it can be calculated using equation 2.28 [33].

$$\mathbf{E_{sc}}^{\infty}(0,0,\theta_{Sc},\phi_{Sc}) = \frac{e^{ik'r^{\infty}}}{-ik'r^{\infty}} \begin{bmatrix} S_2\cos(\phi_{Sc})^2\cos(\theta_{Sc}) + S_1\sin(\phi_{Sc})^2 \\ (S_2\cos(\theta_{Sc}) - S_1)\cos(\phi_{Sc})\sin(\phi_{Sc}) \\ -S_2\cos(\phi_{Sc})\sin(\theta_{Sc}) \end{bmatrix} \tag{2.28}$$

Where S_1 and S_2 are the Mie's coefficients defined by the equation 4 of reference [33]. These coefficients are depended on the polar angle that is considered (θ_{Sc}), the relation

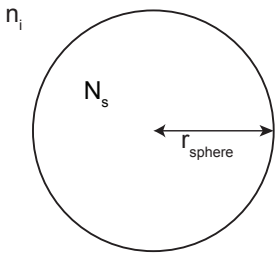

Figure 2.5: Representation of the Mie geometry. N_{sphere} and n_i stand for the RI of the sphere and the incident medium, respectively. r_{sphere} is the radius of the sphere.

between the incident medium and the sphere's RI and also the ratio between the wavelength considered and the radius of the particle.

r^{∞} represents the distance from the scatterer where the field is being evaluated (more detail in section 2.2.1.2 in page 19). For this equation to be valid the far field distance r^{∞} must satisfy the condition $r^{\infty} >> \lambda$.

2.1.4 Anisotropic Bobbert Vlieger theory

In this section, it is reported how is calculate BSDF of this type of geometries. There are two main goals in this section: first it is explained how to calculate the BSDF for a sphere coated with an anisotropic thin film close to an isotropic substrate with an anisotropic thin film above. Then it is explained how to calculate the BSDF considering the ABV model and the incident illumination.

In 1988, Bobbert and Vlieger found the exact solution of the Maxwell's equations for homogeneous isotropic sphere above an isotropic homogeneous substrate (figure 2.6 a)) [18, 19].

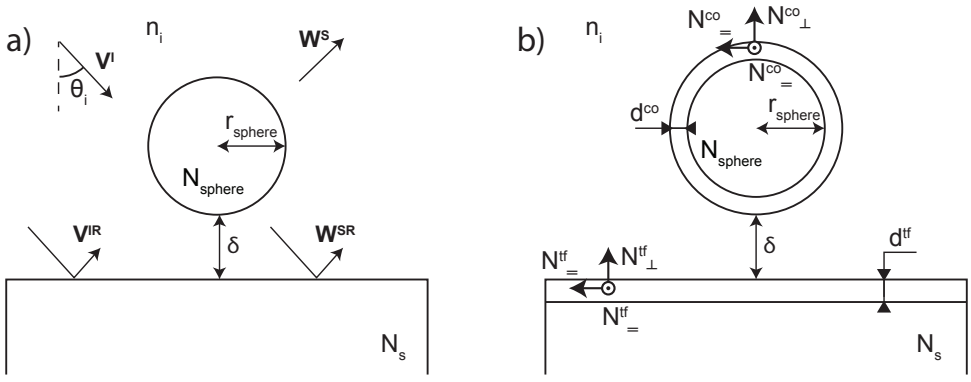

Figure 2.6: a) Representation of the traditional BV model. b) representation of the ABV. Based on reference [20].

To solve the Maxwell's equations for this geometry, Bobbert and Vlieger wrote the formal solution of their model as equation 2.29 [19].

$$\mathbf{W^S} = (1 - \mathscr{B}\mathscr{A})^{-1}\mathscr{B}(\mathbf{V^I} + \mathbf{V^{IR}}) \tag{2.29}$$

To find the total solution of the BV model it is required to take in account the multiple interactions sphere-substrate. Considering an incident electromagnetic plane wave $\mathbf{V^I}$ the scattered field is constituted by the component scattered by the sphere $\mathbf{W^S}$ and also by the component scattered by the sphere that interacts with the substrate $\mathbf{W^{SR}}$. The same approach is required regarding the incident wave: the incident wave interacts with the substrate and the light reflected by it interacts the with the sphere itself. This incident component is represented by $\mathbf{V^{IR}}$ [19].

The matrices $\mathscr{A}$ and $\mathscr{B}$ characterized the light interaction with the substrate and the sphere respectively. More precisely, the $\mathscr{B}$ consists in the Mie's solution [31].

Without going in details in the mathematics, Bobbert and Vlieger arrived to the Fresnel coefficients for the BV model (full mathematical derivation in reference [19]). Therefore, it is introduced the function $\mathcal{J}^{sphere'}$ which represents the BSDF of a sphere close to a substrate. In the case that there is no reflectivity in the interface incident medium-substrate, $\mathcal{J}^{sphere'}$ consists in Mie's solution.

The traditional BV model (figure 2.6 a)) is not a valid model to simulate the approach of a liposome to a cell because the SLB is characterized by an optical anisotropy which impacts how the light is scattered. To increase the precision of the modulation is, in this work, introduced the ABV model (figure 2.6 b)) which allows to model core-shell particles with anisotropic shell above an isotropic substrate with an anisotropic thin film.

An extension of the BV model was done by De Beule which allows to model core-shell particles with anisotropic shell above an isotropic substrate [20]. For this purpose, he replaced the Mie solution $\mathscr{B}$ for the Mie's solution that take in account anisotropic core-shell spheres, derived by Lange and Aragón [34]. It is important to highlight the fact that Lange and Aragón's solution assumes that $d^{co} >> r_{sphere}$.

To model what is purpose in this work, it is required to consider the ABV model which consists in a extension of De Beule's BV model. To calculate the Fresnel coefficients of the ABV, it was replaced the equations 8.7 a) and 8.7 b) of reference [19] by the reflection coefficients of an ISATF, presented in equation 2.22 and 2.23. Following then the same mathematical rational that Bobbert and Vlieger it can be calculated the BSDF for a core-shell particle with an anisotropic shell near an isotropic substrate with an anisotropic thin film ($\mathcal{J}^{sphere}$).

The BSDF $\mathcal{J}^{sphere}$ calculates how light is scattered from ABV model. It is important to highlight the fact that $\mathcal{J}^{sphere}$ also depends on the substrate's solution. To calculate the total solution of this type of geometry it is also required to take in account the impact of the incident illumination. For this purpose, it is required to study independently the transmission and reflection case.

Reflection mode

In the reflection mode, the total scattered light is given by the coherent superposition of the scattered light by the sphere and the reflected light by the substrate. Special attention must be taken in account in relation to the relative phase of both components. The total BRDF for a sphere centered in the origin is given by equation 2.30 [18].

$$\mathcal{R}^{total}(\theta_i, \phi_i, \theta_{Sc}, \phi_{Sc}) = \mathcal{R}^{sub}(\theta_i, \phi_i, \theta_{Sc}, \phi_{Sc}) e^{2iqk'\cos(\theta_i)} + \mathcal{F}^{sphere}(\theta_i, \phi_i, \theta_{Sc}, \phi_{Sc}) \tag{2.30}$$

where $q = r_{sphere} + \delta$ and k' is the wave number. The phase reference of the $\mathcal{F}^{sphere}$ is in the center of the sphere. The phase term appears because the reflection of the incident wave occurs at the substrate which is a distance $r_{sphere} + \delta$ of the reference phase.

The scattered field for a substrate seeded with a density M of uniform spheres can be calculated using the ABV solution. Assuming the specular conditions ($\theta_i = \pi - \theta_{Sc}$ and $\phi_i = \phi_{Sc}$) the respective solution was deduced by Bobbert et al. and it is represented in equation 2.31 [18].

$$\mathcal{F}'^{total}(\theta_i, \phi_i, \pi - \theta_i, \phi_i) = \mathcal{R}^{sub}(\theta_i, \phi_i, \pi - \theta_i, \phi_i) e^{2iqk'\cos(\theta_i)} + \frac{2\pi i M}{k'^2 \cos(\theta)} \mathcal{F}^{sphere}(\theta_i, \phi_i, \pi - \theta_i, \phi_i) \tag{2.31}$$

The optical theorem that deduce equation 2.31 ignore the interaction between the spheres therefore the condition $M \ll \frac{1}{4r_{sphere}^2}$ must be satisfied for accurate modeling.

Transmission mode

For the transmission mode, the total solution is also given by the coherent superposition of the incident and scattered illumination. But in this case is also necessary to take in account the refraction in the incident medium-substrate interface. A schematic of the transmission case is represent by figure 2.7.

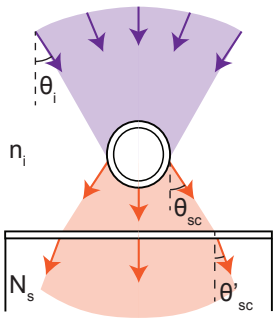

Figure 2.7: Representation of the ABV in the transmission case. The violet light represents the incident field and the orange light the incident field with the contribution of the scattered field by the sphere.

The transmission case can be divided in two different steps: the first between the center of the sphere and the substrate where the total solution is given by the coherent superposition of the incident light and the scattered light propagating with direction (θ_{Sc}, ϕ_{Sc}); and the second, inside the substrate, where the field is given by the field between the sphere and the substrate taking into account the refraction in the interface incident medium-substrate.

The equation 2.32 introduces the total solution for the transmission case.

$$\mathcal{T}^{total}(\theta_i,\phi_i,\theta_{Sc},\phi_{Sc}) = \left(\begin{bmatrix} B(\theta_i,\phi_i,\theta_{Sc},\phi_{Sc}) & 0 \\ 0 & B(\theta_i,\phi_i,\theta_{Sc},\phi_{Sc}) \end{bmatrix} + \mathcal{J}^{sphere}(\theta_i,\phi_i,\theta_{Sc},\phi_{Sc})\right)\begin{bmatrix} t_{pp}^{sub}(\theta_{Sc}) & 0 \\ 0 & t_{ss}^{sub}(\theta_{Sc}) \end{bmatrix} \quad (2.32)$$

where

$$B(\theta_i,\phi_i,\theta_{Sc},\phi_{Sc}) = \begin{cases} 1, & \text{if } \theta_i = \theta_{Sc} \wedge \phi_i = \phi_{Sc} \\ 0, & \text{otherwise} \end{cases} \quad (2.33)$$

The rational behind the function B is similar that for the equation 2.27 but in equation 2.32 is being considered immediately after the particle.

After the coherent sum of the scattered field and the incident illumination it is required to multiply by the Jones matrix of the substrate. It is important to highlight that the incident direction of the light in the substrate is (θ_{Sc}, ϕ_{Sc}), as figure 2.7 suggests. The last step is to consider the change in the direction of the light which is given by Snell's law (equation 2.34) [23].

$$\theta'_{Sc} = \sin^{-1}\left(\frac{n_i \sin(\theta_{Sc})}{N_s}\right) \quad (2.34)$$

For the case when $n_i \neq N_s$ it should be take in account the phase difference due to the propagation through a stratified media [35]. Since that the geometries considered in this work where $n_i \neq N_s$ the distance $r_{sphere} + \delta$ is relatively small and the difference between n_i and N_s is also relatively small it is worth neglecting the phase difference due to the stratified media propagation.

2.1.4.1 Endocytosis model

To take in matter, a cell can invaginate its membrane to form vacuoles, *i.e.* endocytosis. In the case that the cell is incorporating a liposome, the process starts with the approach of the respective to the cellular membrane. Then several invaginations occur in the cellular membrane in order to incorporate the liposome in the cell.

From a simulation point of view, it is hard to modulate the invaginations of the cellular membrane and its respective topographic alterations. Therefore, to simulate the

endocytosis process, it is just considered the approximation of a liposome to the cellular membrane. This is achieved considering the ABV model where the distance between the sphere and the substrate is decreasing as illustrated by figure 2.8.

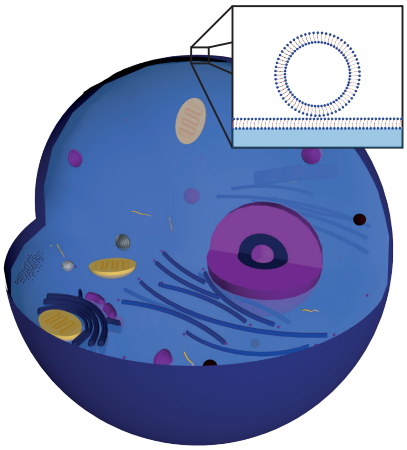

Figure 2.8: Representation of the endocytosis optical model. The square on the top represents a zoom in where the endocytosis is happening. 3D model made by 16-404 [36].

Figure 2.8 depicts the geometry chosen to modulate the endocytosis. The zoom in of the figure 2.8 represents an ABV model where the substrate and incident medium are both water (intracellular and extracellular mediums, respectively). Then the cellular membrane can be interpreted as a thin film with the optical proprieties of a SLB. The liposome is modulated considering a sphere with a water core and a SLB as a core-shell.

This consists in a rough approximation, since that the substrate is only made of water, so it is not considered the impact of the different cellular organelles or the glass substrate that would be required for experiments. Unless otherwise mentioned, the default parameters of the model are available in table 2.1.

Table 2.1: Default simulation parameters of endocytosis. The denominations agree with the figures 2.6 b) of page 13.

Model parameter	Value	Model parameter	Value
$N_{\parallel}^{co} = N_{\parallel}^{tf}$	1.45	r_{sphere}	95 nm
$N_{\perp}^{co} = N_{\perp}^{co}$	1.46	$d^{tf} = d^{co}$	5 nm
$N_s = N_{sphere} = n_i$	1.335	δ	0 nm

Based on the statements provided in this section about endocytosis, it was elaborated a geometry that approximate what occurs in endocytosis. This way, it is possible to study the optical scattering proprieties of this event and incorporate the model in a DIC model to calculate theoretical images. The DIC model elaboration is discussed in the next sections.

2.2 Image formation

In this section, it is presented briefly the main aspects regarding the theory applied in microscope modulation, in particular in section 2.2.1 and its application to model a standard wide field microscope in section 2.2.2 [37]. The last section 2.2.3 explains the modifications required to create a DIC model based on Munro and Török's theory [15].

The theory explained bellow is commonly expressed using rotation matrix instead of unitary vectors [33, 38]. However, in this work, it is used the second approach because from a computational point of view it requires less calculations and Random-Access Memory (RAM).

2.2.1 Fourier optics

The utilization of Fourier transforms is highly used in theoretical optics. Its strength is that the propagation of the electric field is relatively easy in this space, as explained bellow.

This section starts explaining the proprieties of the angular spectrum (section 2.2.1.1) and the second part explains the electric far field (section 2.2.1.2).

2.2.1.1 Angular spectrum

The angular angular spectrum can be interpreted as a mathematical way to describe an electric field decomposing the respective in plane (and evanescent) waves. This means that an electric field $\mathbf{E}(x, y, z)$ which is a function dependent of its spatial coordinates can be represented as the interference of multiple plane and evanescent waves with different directions. Assuming that is known the distribution of an electric field over a plane $z = 0$ the respective angular spectrum can be calculated by the equation 2.35.

$$\hat{\mathbf{E}}(k_x, k_y, 0) = \frac{1}{4\pi^2} \iint_{-\infty}^{\infty} \mathbf{E}(x, y, 0)\, e^{i(k_x x + k_y y)}\, dy\, dx \tag{2.35}$$

Considering now the angular spectrum, the function $\hat{\mathbf{E}}(k_x, k_y, 0)$ gives the amplitude (real part) and the phase (imaginary part) of the plane wave with direction (k_x, k_y, k_z) that constitute the electric field $\mathbf{E}(x,\ y,\ 0)$. Please note that $k_z = \sqrt{k'^2 - k_x^2 - k_y^2}$ and k' is the wave number ($\frac{2\pi}{\lambda}$).

The big advantage of the angular spectrum is that it allows to propagate the electric field over the z axis. Therefore, assuming the angular spectrum $\hat{\mathbf{E}}(k_x, k_y, 0)$, the respective angular spectrum in the plane z' can be calculated by the equation 2.36 (more detail in section 3.10 of reference [39]).

$$\hat{\mathbf{E}}(k_x, k_y, z') = \hat{\mathbf{E}}(k_x, k_y, 0) e^{\pm i k_z z'} \tag{2.36}$$

The ± symbol shows that there are two solutions that can be taken in account: the + symbol for the waves propagating in the positive direction of the z axis and the − symbol

that is for the waves propagate in the opposite direction. Dependent of the case in study it is required to take in account one or other.

It is then possible to transform from the Fourier space back to the spatial space using the inverse transformation represented in the equation 2.37.

$$\mathbf{E}(x,y,z') = \iint_{-\infty}^{\infty} \hat{\mathbf{E}}(k_x,k_y,z')e^{i(k_x x+k_y y)}\, dk_y\, dk_x \tag{2.37}$$

As said previously, the angular spectrum can be divide in plane and evanescent waves: the first one are waves that propagates to the infinite and without loss of amplitude over the distance. In contrary, the evanescent waves have a exponential decay along the z axis ($e^{-|k_z||z|}$). In a DIC microscope waves propagates over big distances when related with the wavelength of the light which allows to ignore the influence of evanescent waves. This reduce the interval of integration to $k_x^2 + k_y^2 \leq k'^2$ in equation 2.37 instead of $-\infty$ to ∞. More detail regarding evanescent waves can be found in section 2.15 of reference [37].

2.2.1.2 Far field

In this section, it is explained the principle behind the definition of the far field and its importance for microscope modulation.

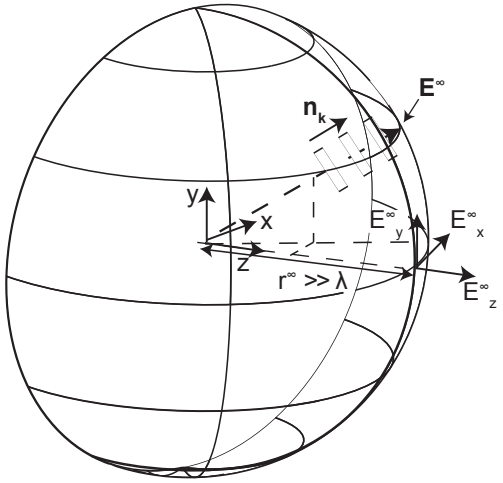

Figure 2.9: Far field representation. $\mathbf{E}^{\infty}$ represents the electric field over the sphere situated far away from the origin.

Assuming that is known the angular spectrum of an arbitrary electric field $\mathbf{E}$ in the plane $z = 0$, it is possible to calculate the electric field in a sphere at distance r^{∞} from the origin using the equation 2.37. The resultant equation is represented by the equation 2.38.

$$\mathbf{E}^{\infty} = \lim_{r^{\infty}k'\to\infty} \iint_{k_x^2+k_y^2\leq k'^2} \hat{\mathbf{E}}(k_x,k_y,0)e^{-i(k_x x+k_y y+k_z\sqrt{r^{\infty 2}-x^2-y^2})}dk_y dk_x \tag{2.38}$$

The range of integration can be reduced to $k_x^2+k_y^2 \leq k'^2$ because the field is being evaluated far away from the origin so there is no contribution of the evanescent waves.

Without going in details regarding the mathematics behind, the equation 2.38 can be transform in equation 2.39 using the method of *stationary phase* (more detail about this method can be found in section 3.3 of reference [40]).

$$\mathbf{E}^{\infty}(x,y) = -2\pi i k_z \hat{\mathbf{E}}(k_x,k_y,0)\frac{e^{ik'r^{\infty}}}{r^{\infty}} \tag{2.39}$$

The equation 2.39 shows that in the far field only the plane wave directed to the specific point in the sphere contributes to the electric field. This happen because the remaining plane waves are cancelled by destructive interference. This result validates the use of geometric optics allowing the application of rotations in the far field.

With the combination of equations 2.37 and 2.39 it is possible to calculate the field near of the origin based on a known far field (equation 2.40).

$$\mathbf{E}(x,y,z) = \frac{ir^{\infty}e^{ik'r^{\infty}}}{2\pi}\iint_{k_x^2+k_y^2\leq k'^2}\mathbf{E}^{\infty}(k_x,k_y)e^{i(k_x x+k_y y\pm k_z z)}\frac{1}{k_z}dk_y\ dk_x \tag{2.40}$$

The equation 2.40 allows the link between the far field and the near field. The importance of this relation is that geometric optics is valid in the far field but is not valid in the near field. It is therefore valid to propagate the field to the far field to apply geometric optics and then back-propagate to calculate the near field.

2.2.2 Microscope modulation

This section refers to the principles behind the modulation of a standard wide field microscope. The representation of a microscope with its working principal and its mathematical is available in figure 2.10.

The figure 2.10 a) represents the illumination path based on Köhler illumination [41]. The Köhler illumination has the advantages of minimizing the influence of the source light in the image. This is justified because, as it is possible to see in figure 2.10 a), the light from the source is out of focus in the image plane. Another advantage of using Köhler illumination is that it generates an even illumination of the sample reducing the image artefacts and increases the image contrast. The light path of the scattered light is illustrated by the figure 2.10 b) and, contrary to the illumination light, this is focused by the tube lens in the image plane allowing to form the image of the object.

At last, the figure 2.10 c) represents the theoretical representation of a wide field microscope based on plane waves. Due to the Köhler illumination, the incident light in the sample is propagating parallel to the z axis (represented by the violet plane wave in figure 2.10 c)). The BSDF calculated in section 2.1.4 already take in account the propagation of the incident illumination therefore the green plane/spherical waves already combined the figures 2.10 a) and b).

The next section refer to the implementation of the theory from section 2.2.1 to create a model of a wide field microscope. This section is elaborated following the light path of a microscope. Hence, it is first explained to model the incident light interaction with

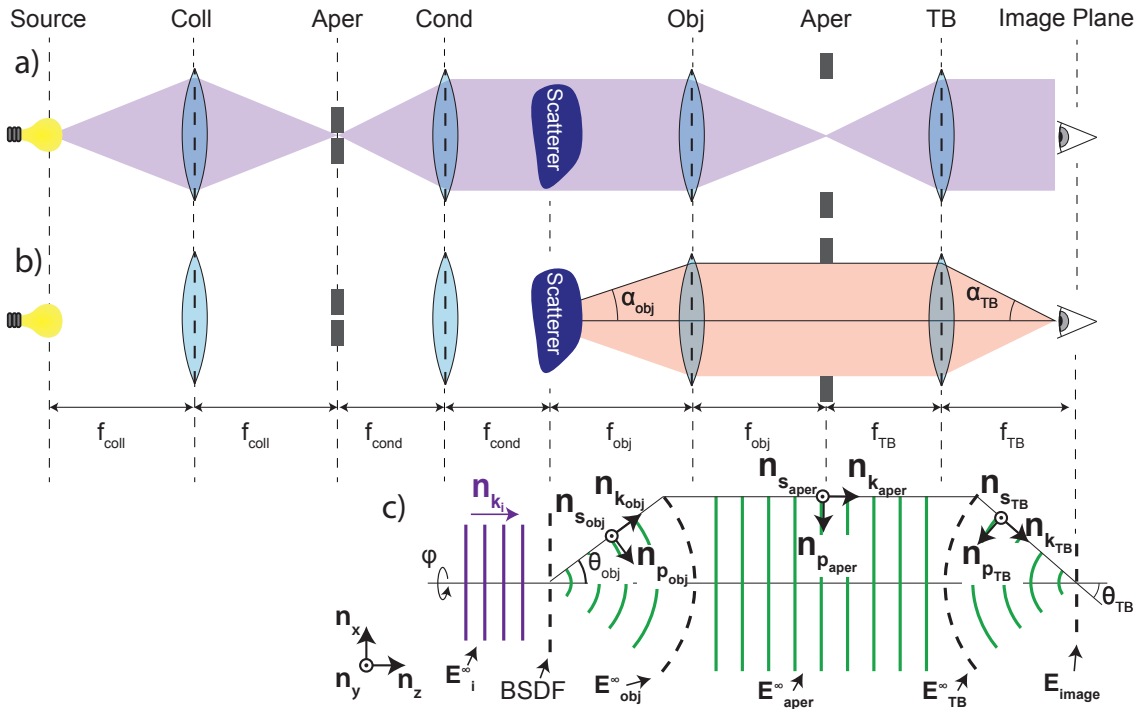

Figure 2.10: Representation of a wide field microscope. a) represents the illumination path. b) represents the scattered illumination path. c) represents the mathematical interpretation of a wide field microscope. The abbreviations stand for: Coll - Collector lens; Cond - Condenser; obj - Objective; Aper - Aperture; TB - Tube Lens. Based on references [37, 41].

the sample (section 2.2.1.1) then the objective's effect (section 2.2.2.2) and at last the tube lens's action (section 2.2.2.3) ending with the calculation of the microscope's image.

2.2.2.1 Scattered far field

The objective of this section is to provide the necessary theory used to calculate the scattered far field from an arbitrary sample. In this work, the model will be just applied to the Mie theory and ABV model but the theory explained can be applied for any scatterer which is interaction with the light is defined as a BSDF. In previous section 2.1 it was already explained how to calculate the BSDF for the geometries needed so in this section it will be assumed that the BSDF is known.

The figure 2.11 represents the light interaction with an arbitrary scatterer.

In section 2.1 the BSDF is defined in the coordinate system (s, p, k). To calculate in the (x, y, z) it is required to define the relations between these two coordinate systems. The relations can be found using the spherical unitary vector and are presented in equations 2.41 to 2.44. The definition of the spherical unitary vectors can be found in appendix A.1.

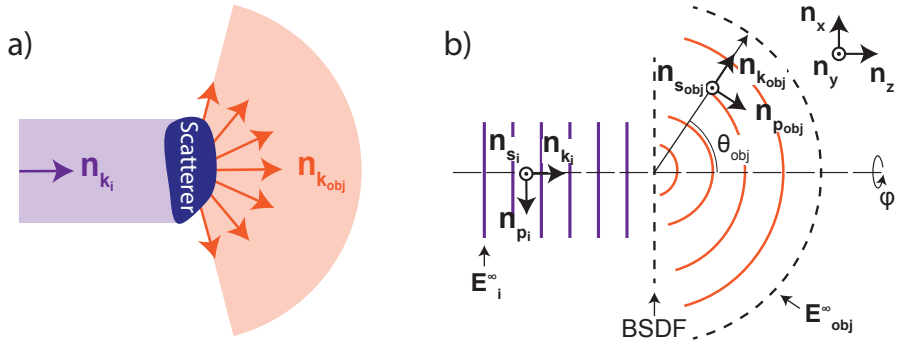

Figure 2.11: Representation of a practical and mathematical interpretation of the light interaction with an arbitrary scatterer. $\mathbf{E_i}^{\infty}$ is the incident far field in the sample and $\mathbf{E_{obj}}^{\infty}$ is the scattered far field. The BSDF consists in the mathematical representation of the scatterer.

$$\mathbf{n}_{\mathbf{s_i}} = \mathbf{n}_{\phi} \tag{2.41}$$

$$\mathbf{n}_{\mathbf{p_i}} = \mathbf{n}_{\theta} \tag{2.42}$$

$$\mathbf{n}_{\mathbf{s_{obj}}} = \mathbf{n}_{\phi} \tag{2.43}$$

$$\mathbf{n}_{\mathbf{p_{obj}}} = -\mathbf{n}_{\theta} \tag{2.44}$$

At this point, it is already possible to proceed for the calculation of the scattered far field $\mathbf{E_{obj}}^{\infty}$. For this lets consider the BSDF's definition (equation 2.7): the Fresnel coefficient $f_{ps}(\theta_i,\ \phi_i,\ \theta_{obj},\ \phi)$ represents the ratio between the incident p component $(\mathbf{E_i}^{\infty} \cdot \mathbf{n}_{\mathbf{p_i}})$ of an incident plane wave with direction $(\theta_i,\ \phi_i)$ scattered as s component $(\mathbf{n}_{\mathbf{s_{obj}}})$ of a scattered plane wave with direction $(\theta_{obj},\ \phi)$. In mathematical language, this definition is translate to equation 2.45 (section 3.3 of reference [32]).

$$\mathbf{E_{obj}}'^{\infty}(\theta_i,\ \phi_i,\ \theta_{obj},\ \phi) = f_{ps}(\theta_i,\ \phi_i,\ \theta_{obj},\ \phi)\ (\mathbf{E_i}^{\infty}(\theta_i,\phi_i) \cdot \mathbf{n}_{\mathbf{p_i}}(\theta_i,\phi_i))\ \mathbf{n}_{\mathbf{s_{obj}}}(\theta_{obj},\phi) \tag{2.45}$$

Using the same approach for the other three Jones matrix elements it is possible calculate the total scattered electric field (equation 2.46).

$$\begin{aligned}\mathbf{E_{obj}}^{\infty}(\theta_i,\phi_i,\theta_{obj},\phi) = \frac{e^{ik'f_{obj}}}{-k'f_{obj}} \\ (\mathbf{E_i}^{\infty}(\theta_i,\phi_i)\cdot\mathbf{n}_{\mathbf{p_i}}(\theta_i,\phi_i))f_{pp}(\theta_i,\phi_i,\theta_{obj},\phi)\mathbf{n}_{\mathbf{p_{obj}}}(\theta_{obj},\phi)+ \\ (\mathbf{E_i}^{\infty}(\theta_i,\phi_i)\cdot\mathbf{n}_{\mathbf{p_i}}(\theta_i,\phi_i))f_{ps}(\theta_i,\phi_i,\theta_{obj},\phi)\mathbf{n}_{\mathbf{s_{obj}}}(\theta_{obj},\phi)+ \\ (\mathbf{E_i}^{\infty}(\theta_i,\phi_i)\cdot\mathbf{n}_{\mathbf{s_i}}(\theta_i,\phi_i))f_{sp}(\theta_i,\phi_i,\theta_{obj},\phi)\mathbf{n}_{\mathbf{p_{obj}}}(\theta_{obj},\phi)+ \\ (\mathbf{E_i}^{\infty}(\theta_i,\phi_i)\cdot\mathbf{n}_{\mathbf{s_i}}(\theta_i,\phi_i))f_{ss}(\theta_i,\phi_i,\theta_{obj},\phi)\mathbf{n}_{\mathbf{s_{obj}}}(\theta_{obj},\phi)\end{aligned} \tag{2.46}$$

The term $\frac{e^{ik'f_{obj}}}{-k'f_{obj}}$ takes in account the propagation of the electric field until the far field distance where it is evaluated. In this case, the far field is being evaluated in a sphere situated at the focal distance of the objective for the reasons explained in the section 2.2.2.2.

Due that the goal of this work is to model a wide field microscope (contrary to confocal microscopy [33]) it is not necessary to consider a situation where θ_i and ϕ_i are different of 0 rad.

Example:

This section provides a checkpoint to give a practical example of the theory explained behind. It is here calculated the far field of a gold nanoparticle. More detailed information about the characteristic of the system can be found in table 2.2.

Table 2.2: Characteristic of the system modelled in figure 2.12. The denomination agrees with the figure 2.6 a) of page 13.

Parameter	Value	Parameter	Value
$\mathbf{E_i}$	(1, 0, 0)	λ	488 nm
r_{sphere}	250 nm	N_{sphere}	1.13 + 1.84i [42]
n_i	1	N_s	1
θ_i	0 rad	ϕ_i	0 rad

The theory of this sections consists in the application of equation 2.46 which require the utilization of the BSDF of a sphere defined in section 2.1.4 ($\mathcal{F}^{sphere}$). The graphs of the figure 2.11 represents the results considering the system of the table 2.2.

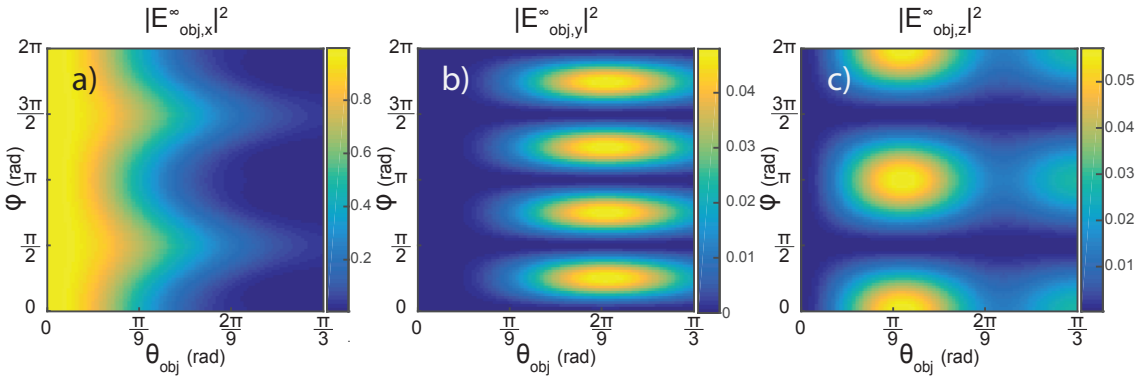

Figure 2.12: Scattered far field of a gold nanoparticle in vacuum. The graphs are normalized relatively to the x component maximum. For display purposes, the incident field is not being considered.

The graphs of the figure 2.12 shows the distribution of the scattered field over a sphere far away from the sample. The incident plane wave monochromatic and x-polarized that propagates parallel to the z axis is scattered in all directions originating a electric field in all components.

The ratio between the x components and the other are still considerable which highlight the necessity of considering the light's vectorial approach.

2.2.2.2 Objective

Many approach to calculate the interaction of an electromagnetic field with a lens can be applied. For example, it is possible to use geometric ray trace but this approach lack of precision if it is considered high NA lens. To rigorous model a high NA lens it is required to use Fourier optics and to take in account the full vectorial nature of the light to consider the longitudinal component of the electric field that this lens creates [38].

In 1959, Wolf and Richards studied the theory behind the focusing of an electromagnetic field by a lens using Fourier optics [16, 17]. In the respective references, it is possible to find the full mathematical justifications and deductions to the Debye-Wolf integral. In this dissertation, it is just explain the theory from a practical point of view based on the section 3.5 of reference [37].

To understand how to model the focusing of an electromagnetic field by a lens, it is required to introduce the term *Gaussian sphere*: Considering the objective, the *Gaussian sphere* is an imaginary sphere with radius f_{obj} as represented by the figure 2.13 b).

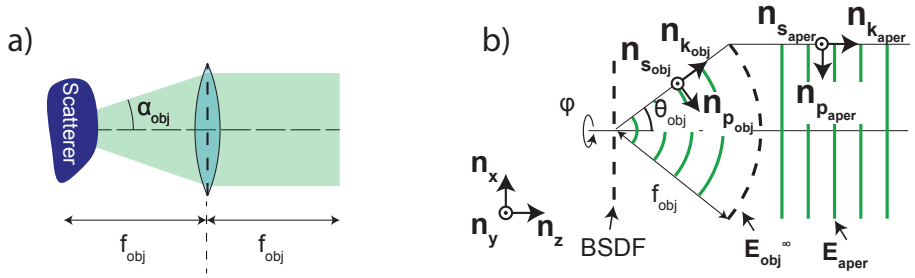

Figure 2.13: Representation of the objective's working principle. a) represents an objective from a practical point of view with α_{obj} being the maximum angle of convergence. b) represents the working principle of an objective from a mathematical point of view. The incident spherical wave is converted to a plane wave at the *Gaussian sphere*. $\mathbf{E_{obj}}^{\infty}$ and $\mathbf{E_{aper}}^{\infty}$ represents the electric field in the *Gaussian sphere* and the field that propagates after the objective, respectively. Based on reference [37].

As suggested by the figure 2.13, the action of the objective can be interpreted as a rotation of the electric field to the center of the respective *Gaussian sphere* centered in the objective's focus point. In the previous section 2.2.1.2 it was explained that geometric optics is valid in the far field ($f_{obj} >> \lambda$). On order words, a lens take an incident spherical/plane wave and transform it to a plane/spherical wave.

The rays rotation can be applied by transforming their direction from $\mathbf{n_{k_{obj}}}(\theta_{obj}, \phi)$ to the direction $\mathbf{n_{k_{aper}}}(\theta_{obj}, \phi)$. To perform this refraction on the *Gaussian sphere* it is advised to split the incident field in the respective p and s components. For this purpose, it is required to determine the relation between the respective unitary vectors and the

coordinate systems. These relations before the objective's *Gaussian sphere* are represented in the equations 2.47 and 2.48.

$$\mathbf{n}_{\mathbf{s}_{\mathbf{obj}}}(\theta_{obj},\phi) = -\mathbf{n}_{\phi}(\theta_{obj},\phi) \quad (2.47)$$

$$\mathbf{n}_{\mathbf{p}_{\mathbf{obj}}}(\theta_{obj},\phi) = \mathbf{n}_{\theta}(\theta_{obj},\phi) \quad (2.48)$$

After the objective's *Gaussian sphere* the unitary vectors of the coordinate system (s, p, k) are directly related with the cylindrical unitary vectors by the equations 2.49 and 2.50.

$$\mathbf{n}_{\mathbf{s}_{\mathbf{aper}}}(\theta_{obj},\phi) = -\mathbf{n}_{\phi}(\theta_{obj},\phi) \quad (2.49)$$

$$\mathbf{n}_{\mathbf{p}_{\mathbf{aper}}}(\theta_{obj},\phi) = \mathbf{n}_{\rho}(\theta_{obj},\phi) \quad (2.50)$$

With the equations above it is possible to calculate the p and s component (equation 2.3 on page 6) before the *Gaussian sphere* and then apply the respective transformation to the cylindrical coordinate system (equation 2.51).

$$\begin{aligned}\mathbf{E_{aper}}^{\infty}(\theta_{obj},\phi) = &\sqrt{\cos(\theta_{obj})}\; t_s(\theta_{obj},\phi)\; (\mathbf{E_{obj}}^{\infty}(\theta_{obj},\phi)\cdot\mathbf{n}_{\phi}(\theta_{obj},\phi))\; \mathbf{n}_{\phi}(\theta_{obj},\phi)\\ &+\sqrt{\cos(\theta_{obj})}\; t_p(\theta_{obj},\phi)\; (\mathbf{E_{obj}}^{\infty}(\theta_{obj},\phi)\cdot\mathbf{n}_{\rho}(\theta_{obj},\phi))\; \mathbf{n}_{\theta}(\theta_{obj},\phi) \quad (2.51)\end{aligned}$$

The introduction of the terms t_p and t_s take in account the Fresnel coefficients for p and s component (defined on page 7) of the lens. It also has been included the term $\sqrt{\cos(\theta_{obj})}$ due to the intensity law considering that the objective satisfied the sine condition [43].

It is important to highlight the fact that the dependence of $\mathbf{E_{aper}}^{\infty}$ to (θ_{obj}, ϕ) is related to the position of the ray in the plane xy and not to the direction of the ray which propagates parallel to the z axis.

2.2.2.3 Tube lens

At this point it is only required to model the action of the tube lens in order to get the resultant image. A schematic of the tube lens's action is represented in figure 2.14.

The principle to model the tube lens is the same that for the objective but instead of transforming from the spherical to the cylindrical unitary vectors the transformation is made from the cylindrical to the spherical unitary vectors. As said before, the dependence of $\mathbf{E_{aper}}^{\infty}$ is related with its position in the plane xy and not to its direction. To calculate the angle of rotation of each ray is necessary to calculate the angle θ_{TB} which can be obtain by matching the x and y position of the objective and tube lens's *Gaussian sphere*. The resultant relation between the angles is given by the equation 2.52.

$$\theta_{TB} = \sin^{-1}\left(\frac{\theta_{obj}\; f_{obj}}{f_{TB}}\right) \quad (2.52)$$

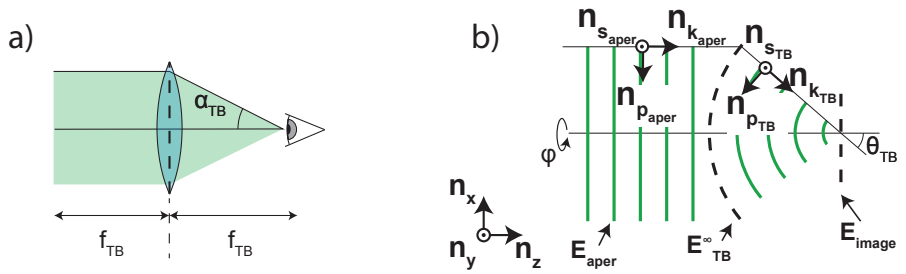

Figure 2.14: Representation of the tube lens's working principle. a) represents a tube lens from a practical point of view with α_{TB} being the maximum angle of convergence. b) represents the working principle of a tube lens from a mathematical point of view. The incident plane wave is converted to a spherical wave at the *Gaussian sphere* that converges to the focal point. $\mathbf{E_{aper}}^{\infty}$, $\mathbf{E_{TB}}^{\infty}$ and $\mathbf{E_{image}}$ represent the electric field incident in the tube lens, the field in the *Gaussian sphere* and the electric field near the focus point, respectively. Based on reference [37]

The transformation expressed in the equation 2.52 is what allows a microscope to amplify an image. The microscope's amplification β, theoretically, is only related to the f_{TB} and f_{obj} by the relation expressed in the equation 2.53.

$$\beta = \frac{f_{TB}}{f_{obj}} \tag{2.53}$$

The last step to calculate the tube lens's far field $\mathbf{E_{TB}}^{\infty}$ is to make the rays's rotation in the *Gaussian sphere* as it was done for the objective. Applying the same rational that for equation 2.51 it is deduced the equation 2.54.

$$\begin{aligned}\mathbf{E_{TB}}^{\infty}(\theta_{TB},\phi) = &\sqrt{\cos(\theta_{TB})}t_s\,(\theta_{TB},\phi)(\mathbf{E_{aper}}^{\infty}(\theta_{TB},\phi)\cdot\mathbf{n}_{\phi}(\theta_{TB},\phi))\,\mathbf{n}_{\phi}\,(\theta_{TB},\phi)\\ &+\sqrt{\cos(\theta_{TB})}\,t_p(\theta_{TB},\phi)\,(\mathbf{E_{aper}}^{\infty}(\theta_{TB},\phi)\cdot\mathbf{n}_{\theta}(\theta_{TB},\phi))\,\mathbf{n}_{\rho}(\theta_{TB},\phi)\end{aligned} \tag{2.54}$$

The equation 2.54 allows the calculation of the far field in the tube lens's *Gaussian sphere*. At this point, it is already possible to implement the equation 2.40 to calculate the field near the focal point. For convenience, the equation 2.40 can be rewritten in terms of angles (θ_{TB}, ϕ) instead of (k_x, k_y, k_z) using the equations 2.55 to 2.57. After the alterations it results in equation 2.58.

$$k_x = k'\sin(\theta)\cos(\phi) \tag{2.55}$$

$$k_y = k'\sin(\theta)\sin(\phi) \tag{2.56}$$

$$k_z = k'\cos(\theta) \tag{2.57}$$

$$\begin{aligned}\mathbf{E_{image}}(x,y,z) = &-\frac{ik' f_{TB} e^{-ik' f_{TB}}}{2\pi}\\ &\int_0^{\alpha_{TB}}\int_0^{2\pi}\mathbf{E_{TB}}^{\infty}(\theta_{TB},\phi)e^{ik'\cos(\theta_{TB})z}e^{ik'\sin(\theta_{TB})(\cos(\phi)x+\sin(\phi)y)}\sin(\theta_{TB})d\phi d\theta_{TB}\end{aligned} \tag{2.58}$$

Some changes has been done comparing to the equation 2.40: due that the field is being back propagating from the *Gaussian sphere* the far field distance (r^{∞}) has been substitute by the focal distance of the lens (f_{TB}); the - signal appears because the far field is being evaluated in $-f_{TB}$; in the factor $ik'\cos(\theta_{TB})z$ only the fields that propagate in the positive direction of the z axis must be considered so the - signal is ignored; the interval integration of θ_{TB} is reduced in 0 to α_{TB} according to the tube lens's maximum angle of convergence.

Example

As before, it is presented an example of the theory explained behind. This example consists in the resultant image of a gold nanoparticle as in section 2.2.2.1. The detailed input is presented in table 2.3.

Table 2.3: Characteristic of the system modelled in figure 2.15. The denomination of the scatterer's parameter agrees with the figure 2.6 a) of page 13.

Parameter	Value	Parameter	Value
$\mathbf{E_i}$	(1, 0, 0)	λ	488 nm
r_{sphere}	250 nm	N_{sphere}	1.13 + 1.84i [42]
n_i	1	θ_i	0 rad
ϕ_i	0 rad	β	40
α_{obj}	$\frac{\pi}{3}$ rad		

Contrary to the example 2.2.2.1, here is taken in account the contribution of the incident illumination in the final image.

Considering the objective's far field $\mathbf{E_{obj}}^{\infty}$ calculated in the previous example, it is possible to use the equation 2.51 to calculate how the electric field evolves between the objective and tube lens. Considering the equation 2.52 and with the application of equation 2.54 it is determined the electric field in the tube lens's *Gaussian sphere*. The last step, is the utilization of Debye-Wolf integral to back-propagate the far field from the *Gaussian sphere* to the image plane (equation 2.58). The results are represented by the figure 2.15 in which can be seen a gold nanoparticle wide field microscope image.

Usually the focal distance of the tube lens is relatively high in order to provide an high amplification to the microscope. The utilization of low NA generates a very small z component in the image plane as it is possible to see in figure 2.15 c). For this reason, in the next graphs of this type the z component is omitted.

Another particularity is the effect of the incident illumination. In wide field microscopy that uses Köhler illumination, the incident illumination generates an offset in the image. The image is then the interference of the scattered light and the offset generate by the incident light. A special attention is required in order to match correctly the incident illumination and the scattered light phases, as done in section 2.1.4.

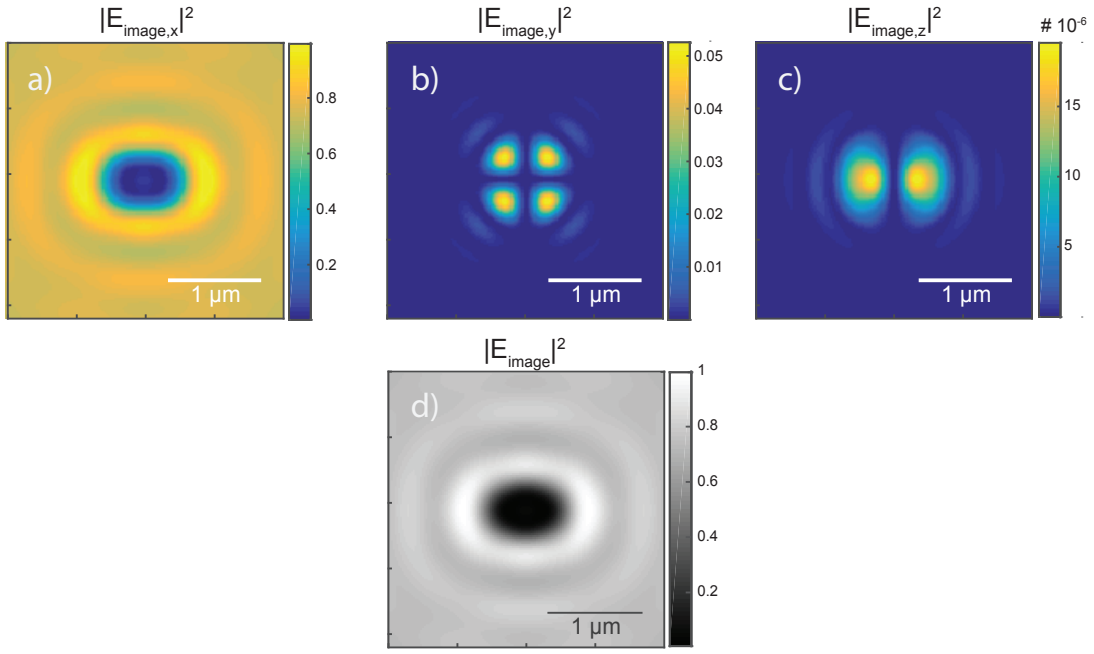

Figure 2.15: Wide field image of a gold nanoparticle in vacuum. a), b) and c) represent the three components of the electric field and d) represents the total intensity image. The graphs are normalized relatively to the $|\mathbf{E_{image}}|^2$'s maximum.

2.2.3 Differential interference contrast microscopy

The previous sections explain the theory to model a wide field microscope. The last step to create a wide field DIC model is to add the DIC's components to the model of the section 2.2.2. In 2005, Munro and Török create a vectorial confocal and wide field DIC's model that allows to rigorous simulate a DIC that uses high NA lens [15].

The figure 2.16 is a schematic of a standard Nomarski DIC.

As figure 2.16 a) suggests, the illumination path of a DIC microscope is very similar to the standard wide field microscope. The differences reside in the action of the Wollaston prism which split the incident light in two orthogonally polarized beams and the analyzer.

Considering the incident light path, the Wollaston prism in the front focal plane generates an angular split between the x and y polarized component. This split makes that the two beams illuminate the sample with a small sheer between them [44]. As in standard wide field microscopy, the incident plane waves propagate parallel to the z axis. The second Wollaston prism recombines the two orthogonally polarized beams into a single beam which is filtered by the analyzer reducing heavily the background.

As mentioned in the previous paragraph, the sample is illuminated by two beams therefore there are also two scattered field as figure 2.16 b) shows. The Wollaston prism in the back focal plane makes the interference between the two scattered beams. The resultant beam is then focused by the tube lens allowing the formation of the scatterer's image. The advantage of DIC is that due that is based on interference of two scattered beams, the image is highly sensible to the phase difference, which justify its application

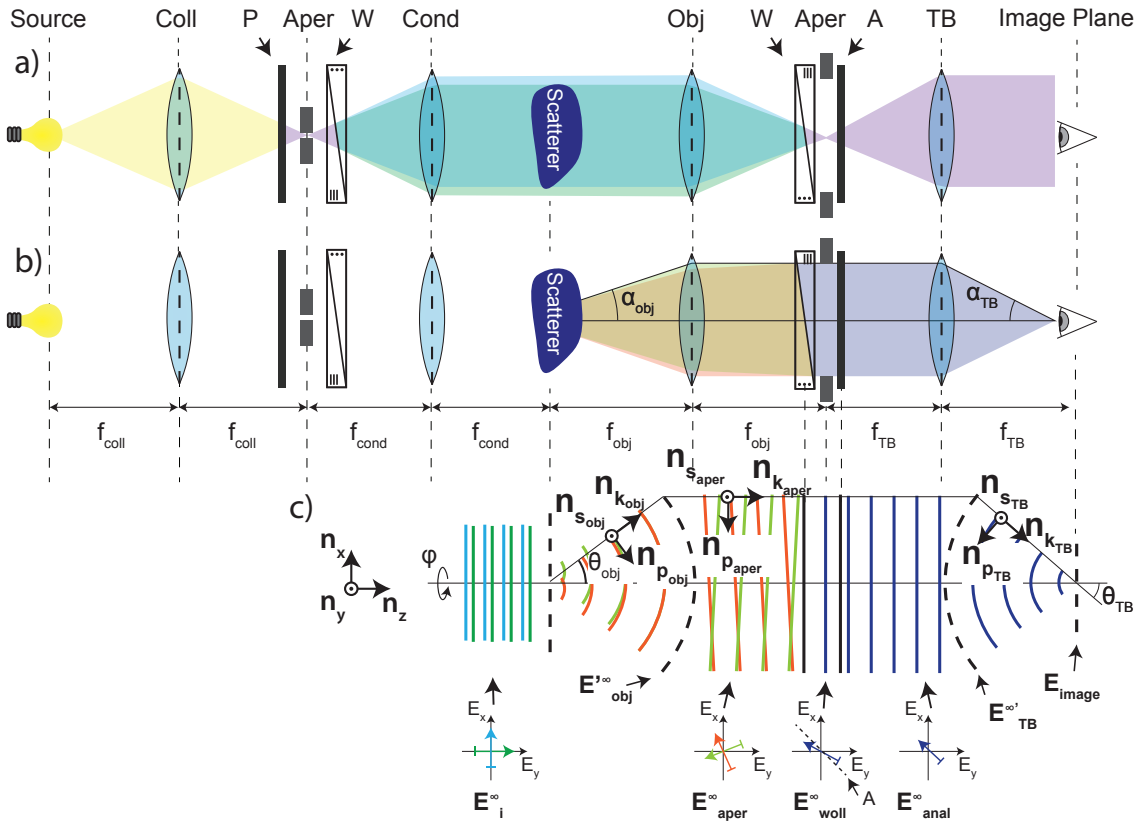

Figure 2.16: Representation of a wide field Nomarski DIC. a) represents the illumination path. b) represents the scattered light path. c) represents the mathematical interpretation of a Nomarski DIC. The four graphs in the bottom of the image represent the polarization state of the light in each part of the microscope. The abbreviations stand for: Coll - Collector lens; Cond - Condenser; obj - Objective; Aper - Aperture; TB - Tube Lens; A - Analyzer; W - Wollaston prism; P - Polariser.

in cells observation.

The schematic of the figure 2.16 c) shows the mathematical interpretation of a wide field DIC. Theoretically a Wollaston prism can be modelled considering that it generates a different phase shift in the x and y component. Therefore, the incident illumination can be interpreted as two plane waves (one x polarized and another y polarized) propagating parallel to the z axis with a phase shift between them. It is then necessary to propagate until the image plane the two-scattered field.

The modulation of the DIC components are explained in this section. It is first explained the modulation of the Wollaston prisms (section 2.2.3.1) and then the modulation of the analyzer (section 2.2.3.2). In the end, it is explained how to incorporate the changes in the model of a standard wide field microscope (section 2.2.2).

2.2.3.1 Wollaston prism

One of the main applications of Wollaston prisms consist in their application in DIC microscopy. As mentioned before they act like a polarising beam splitter inducing an angular divergence depended on the x or y polarised state of the incident beam. As Lessor et al. show, for modelling propose it is valid to consider that the Wollaston prism induces a phase shift instead of an angular shift [45]. Figure 2.17 represents the effect of a Wollaston prism.

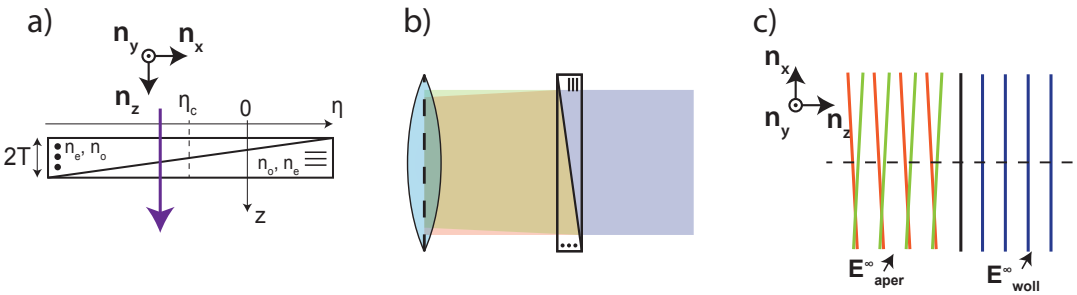

Figure 2.17: Representation of a Wollaston prism. a) Representation of the optical path for a ray propagating throw a Wollaston prism. Based on reference [15]. b) Wollaston prism in a practical point of view. c) Wollaston prism in a mathematical point of view with the phase shift, according to the incident polarization state.

The figure 2.17 b) shows the action of a Wollaston prism in a practical point of view. Taking in account two incident polarized beams, the Wollaston prism generate a different change in the direction according to the incident polarization. It is also possible the representation of this effect using the plane waves representation (figure 2.17 c)). From a mathematical point of view a plane wave with different direction can be interpreted as a proportional phase shift in one direction.

The figure 2.17 a) represents the optical path for a ray propagating parallel to the z axis in the position η. Taking in mind that a Wollaston prism is a uniaxial material with RI n_e and n_o and considering that its center is shifted η_c to the optical axis and that angle between the two parts is θ_w. In the first part of the Wollaston prism the x and y component are aligned with the n_e and n_o respectively and that in the second part it is the opposite. Therefore, calculating the optical path of the ray inside the Wollaston prism it is possible to calculate the phase different which is represented by the equations 2.59 and 2.60 [45].

$$\Phi_x(\eta) = k'(T(n_e+n_o) - \eta_c(n_o-n_e)\tan(\theta_w) + \eta(n_o-n_e)\tan(\theta_w)) \tag{2.59}$$

$$\Phi_y(\eta) = k'(T(n_e+n_o) + \eta_c(n_o-n_e)\tan(\theta_w) - \eta(n_o-n_e)\tan(\theta_w)) \tag{2.60}$$

After the determination of the phase shift and taking into account that $\eta = f_{obj}\sin(\theta_{obj})\cos(\phi)$, the electric field after the Wollaston prism can be calculated applying the phase shift to the respective component, as in equation 2.61.

$$\mathbf{E_{woll}} = \begin{bmatrix} {E_{aper,x}}^{\infty}\, e^{i\Phi_x} \\ {E_{aper,y}}^{\infty}\, e^{i\Phi_y} \\ 0 \end{bmatrix} \tag{2.61}$$

The Wollaston prism action can be resumed in the definition of two constants: the shear and the bias. They are both represented by equations 2.62 and 2.63 respectively [15].

$$x_s = 2f_{obj}(n_o - n_e)\tan(\theta_w) \tag{2.62}$$

$$\Phi_b = -2k'\eta_c(n_o - n_e)\tan(\theta_w) \tag{2.63}$$

The shear (x_s) characterize the angular split of the x and y polarized beam while the bias (Φ_b) is the phase difference of these two.

The equation 2.61 is valid to model the Wollaston prism in the back focal plane. As mentioned before, the incident field in the sample is propagating parallel to the z axis therefore to model the first Wollaston prism cannot be taken in account the term $\eta(n_o - n_e)\tan(\theta_w))$ of equations 2.59 and 2.60. In other words, the shear induced by the Wollaston prism is null.

2.2.3.2 Analyzer

An analyzer consists in a polariser which can be rotated about the optical axis. This way it allows to select the polarization angle that passes throw it.

The modulation of an analyzer is very well known in optics. Traditionally it is defined the Jones matrix and then it is multiplied by the respective incident Jones vector (section 3.3 of reference [23]). For the reasons explain above, in this work it is used unitary vectors instead of Jones matrix.

Considering that the analyzer is rotated by an angle γ about the optical axis the unitary vector that defines the analyzer is defined by equation 2.64.

$$\mathbf{n_{Analyzer}}(\gamma) = \begin{bmatrix} \cos(\gamma) & \sin(\gamma) & 0 \\ -\sin(\gamma) & \cos(\gamma) & 0 \\ 0 & 0 & 1 \end{bmatrix} \begin{bmatrix} 1 \\ 0 \\ 0 \end{bmatrix} \tag{2.64}$$

By the analysis of the figure 2.16 it is possible to see that the electric field before the analyzer is ${\mathbf{E_{woll}}}^{\infty}$ and calling the field after the analyzer ${\mathbf{E_{anal}}}^{\infty}$ their relation is given by the equation 2.65.

$${\mathbf{E_{anal}}}^{\infty} = ({\mathbf{E_{woll}}}^{\infty} \cdot \mathbf{n_{Analyzer}}(\gamma))\, \mathbf{n_{Analyzer}}(\gamma) \tag{2.65}$$

Substituting the tube lens's far field of section 2.2.2 by the far field considering the analyser and the Wollaston prism it is then conclude the modulation of a DIC microscope.

Example

In this section, it is provided an example of a DIC images calculated using the theory explained above. Taking the scattered far field of an incident field calculated using equation 2.61 it is calculated the far field at the objective reference sphere ($\mathbf{E_{obj}}^{\infty}$). Using the same approach that for a standard microscope it is modulated the effect of the objective.

At this point is required to use again equation 2.61 to simulate the second Wollaston prism. The field at the tube lens's reference sphere can be calculated using equation 2.65. At last it is only required to back-propagate the field to the image plane using equation 2.58 as before.

The characteristic of the system used as example are presented in table 2.4.

Table 2.4: Characteristic of the system modelled in figure 2.18. The denomination of the scatterer's parameter agrees with the figure 2.6 a) of page 13.

Parameter	Value	Parameter	Value
$\mathbf{E_i}$	(0.7071, 0.7071, 0)	λ	488 nm
r_{sphere}	250 nm	N_{sphere}	1.13 + 1.84i [42]
n_i	1	θ_i	0 rad
ϕ_i	0 rad	β	40
α_{obj}	$\frac{\pi}{3}$ rad	x_s	100 nm
Φ_b	$\frac{\pi}{3}$ rad	γ	$\frac{3\pi}{4}$ rad

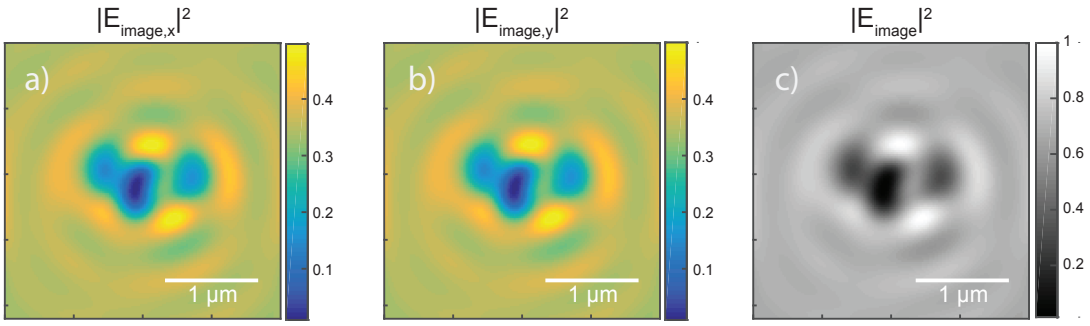

Figure 2.18: DIC image of a gold nanoparticle in vacuum. a), b) represent the x and y components while c) represents the total intensity of the electric field. The graphs are normalized relatively to the $|\mathbf{E_{image}}|^2$'s maximum.

By the figure 2.18 c) is possible to notice the characteristic DIC effect with the white and darker component. This occurs due to the interference between the scattered light of the two beams that generate the image.

Another particularity is that the x and y component are the same that occurs due to the analyzer angle. Controlling the analyzer angle and the bias induced by the Wollaston prism it is possible to control the background intensity [15].

Chapter 3

Materials and methods

This chapter introduces the methods, materials and equipment used in this work to achieve what is purposed and it is divided essentially in two main parts: one where it is explained the methods used to implement the DIC's simulation (section 3.1) and in the second part where it is described the methods used in the experimental part (section 3.2).

3.1 Models implementations and validations

This section explains mainly two principal points. How the implementation of the DIC's model was developed and then the many verifications that were made to make sure the correct implementation of the theory.

Nowadays, there are many programming languages available. Each one with its respective pros and cons. To model what is purposed in this work, it was used several languages trying to use the strength of each one and some code previously developed.

The core of the program was made using MATLAB (The MathWorks Inc., Natick, MA). This language consists in a high-level language ideal for numerical simulations because it provides a good relation between computational time and programmer time. Special attention was made to elaborate a full vectorized code which highly decreased the computational time [46].

The MATLAB script implements the theory explained in section 2.2 making an external link to a C++ library to calculated the scattered BSDF.

At National Institute of Standards and Technology (NIST), Germer elaborated an open-source polarized light interaction C++ library called SCATMECH [47]. This library provides multiple classes that allows to model various geometries which can be used for multiple optics applications. For example, Kim et al. compared the BV SCATMECH class results with experimental data [48] while Germer used SCATMECH to model the

scatterer to implement in an microscope's model [49].

In 2014, De Beule already made an extension of BV SCATMECH class to model core-shell particles with anisotropic shells [20]. To calculate the optical scattering of this system it is required to evaluate complex Bessel functions [34] therefore De Beule made a link between SCATMECH and Mathematica kernel (Wolfram Research, Champaign, Illinois, USA) which provides the evaluation of these type of functions. This extension was made in SCATMECH 6.00 which did not had implemented the BV model in transmission.

With the release of SCATMECH 7.00 in 2017, Germer updated the BV class allowing to model the transmission case. As the name indicates, to model a wide field transmission DIC it is required to consider this mode. Therefore, during this work it was considered the alterations that De Beule made and applied to SCATMECH 7.00.

To fully implement the ABV, it was created a new SCATMECH class which model the light interaction with an ISATF. This implementation was made considering the equations and the theory explained in section 2.1.2.1. At last, it was made a new extension to the BV model of De Beule to consider an ISATF, as described in section 2.1.4.

The author would like to express his gratitude over Laven for making his code to generate points uniformly distributed over a sphere available which was used in this work [50, 51].

The math behind this type of modulation is very complex and susceptible to small errors in its implementation. Hence it is important to make some checkpoints to give some confidence about the results obtained. In this section, it is mentioned the multiple checkpoints made until the implementation was complete and correct.

3.1.1 Bidirectional scatterer distribution function validation

Isotropic substrate with an anisotropic thin film above class validation

The first checkpoint mentioned in this section refers to the ISATF class. To verify if the implementation of the equations 2.23 and 2.22 were correct the results were compared with the data from Accurion EP4 Model version 1.7.3 (Accurion GmbH, Göttingen, Germany). Accurion software can calculate transmissivities and the reflectivities for this type of system allowing a full test to this class.

Anisotropic Bobbert Vlieger class validation

This model goes beyond the actual state of the art available nowadays thus it is not possible to test completely the class. However, it is possible to test some simplified versions of the geometry. It was used the ABV theory to model an isotropic BV geometry being the data compared with the data obtained using the original BV SCATMECH class. This test allowed to check if the implementation of the theory for the calculation of the Fresnel coefficients is well implemented, at least, the results for the isotropic case are correct.

3.1.2 MATLAB script validation

The MATLAB script is the core of the program and the main implementation made during this work. From the tests mentioned before it is assumed that the calculation of the BSDF are correct. It is then necessary to realize some checkpoints regarding the implementation of the image formation's theory. The MATLAB script had three main checkpoints: first it was confirmed if the calculation of the scattered far field is well implemented (equation 2.46, page 22) then, the second checkpoint is the image calculation of a standard wide field microscope (equation 2.58, page 26) and the last one is the complete test of the DIC's implementation (equations 2.61 and 2.65, page 31).

The system modelled consists in a 100 nm spherical scatterer and it is used only to validate the resultant data. The parameters of this system are purely theoretical. The geometry and the details of the optical system are fully described in table 3.1.

Table 3.1: Characteristic of the systems modelled to validate the MATLAB script. The denomination agrees with the figures 2.5, 2.6 a), 2.10, 2.16 and 2.17 of pages 13, 13, 21, 29 and 30.

Parameter	Value	Parameter	Value
$\mathbf{E_i}$	(1, 0, 0)	$\mathbf{E_i}'$	(0, 1, 0)
λ	488 nm	r_{sphere}	100 nm
N_{sphere}	4	n_i	1
N_s	1	β	100
θ_i	0 rad	ϕ_i	0 rad
α_{obj}	$\frac{\pi}{3}$ rad	x_s	20 µm
Φ_b	$\frac{\pi}{4}$ rad	γ	$\frac{3\pi}{4}$ rad

Be aware that only to model a DIC microscope the table 3.1 is used in its totality. In the first two checkpoints, the table is only used partially. $\mathbf{E_i}'$ is only used in for the DIC validation.

Scattered far field validation

The first test of the MATLAB script consists in comparing the scattered far field of the ABV geometry (figure 2.6 b)) in condition $N_s = n_i$ with the respective Mie's model (figure 2.5). Analysing the two geometries, it is clear that in this condition both models correspond to the same system. Therefore, on one side, it was implemented the theory from Török et al. which allows to calculate directly the scattered far field from a homogeneous sphere (equation 2.28, page 2.28) [33] and in the other side it was implemented the equation 2.46 of page 22 that calculates the far field using the BSDF. It is important to highlight the fact that these two theory calculates the same (in the condition $n_i = N_s$) using two different approaches which grant some confidence in the test itself.

The respective results of the scattered far field are shown in figure 3.1. The parameter of the system modelled are presented in table 3.1.

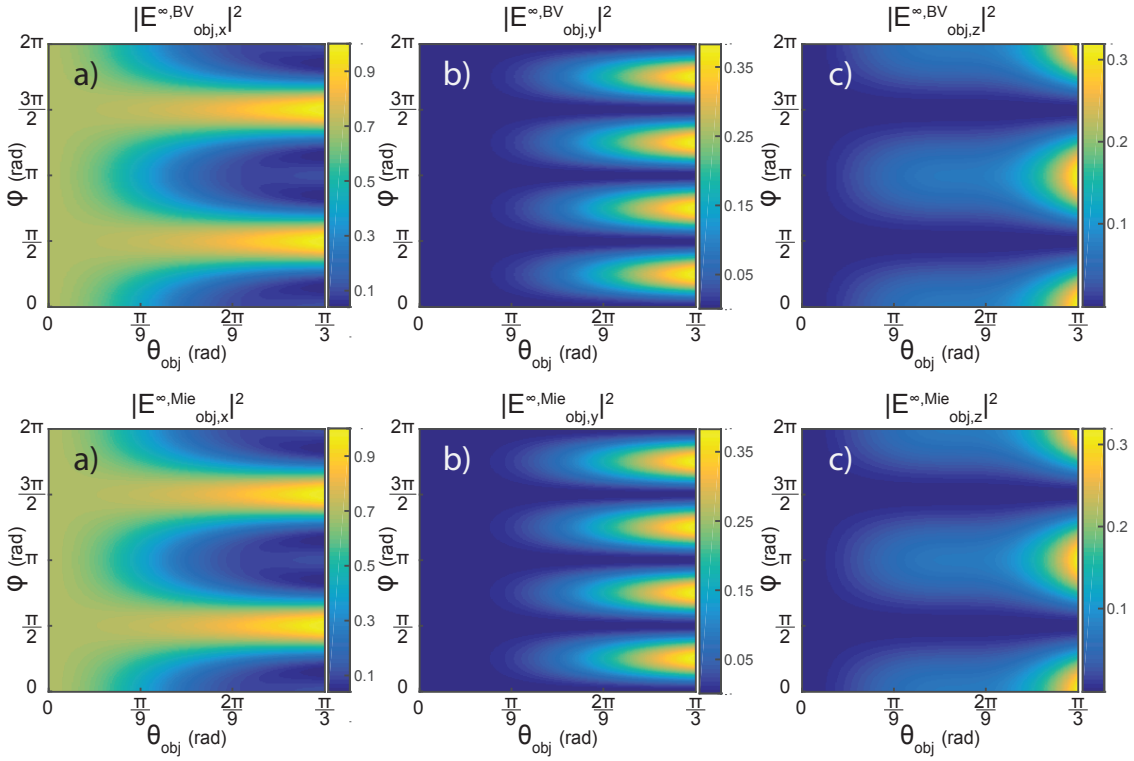

Figure 3.1: Scattered far field using Mie's theory [33] (bottom) and using ABV BSDF (top) for a spherical scatterer. Both electric fields (using Mie theory and ABV model) are normalized relatively to the maximum of the respective $|\mathbf{E_{obj}}^{\infty}|$ The characteristic of the system modelled are presented in table 3.1. For display purposes, the incident field is not being considered in this figure.

The figure 3.1 shows the same results between the two theories. Hence it can be concluded that the implementation of the scattered far field using ABV BSDF is correct. Even if just the absolute value is represented in the graphs of figure 3.1, the real and imaginary part also match between the models. Therefore, the light phase is also consistent and correct. For display purposes, the incident light is not being consider in figure 3.1.

Standard wide field microscope's model validation

Until this point it was validated all the implementations made to calculate the far field in the objective's *Gaussian sphere* ($\mathbf{E_{obj}}^{\infty}$). The next step is considering the modulation of a wide field microscope (section 2.10).

As a reference for the next verifications it was used well tested data send by Dr P. R. T. Munro. During his work in microscope modulation, he already implemented a full vectorial DIC's model which calculates the resultant image considering a Mie scatterer [15].

Using the MATLAB script developed during this work, the calculated resultant image from a wide field microscope with the characteristics presented in table 3.1 is represented by figure 3.2. For this example, just the incident plane wave x-polarized is considered.

The figure 3.2 shows the image originated from a 100 nm spherical scatterer. Only

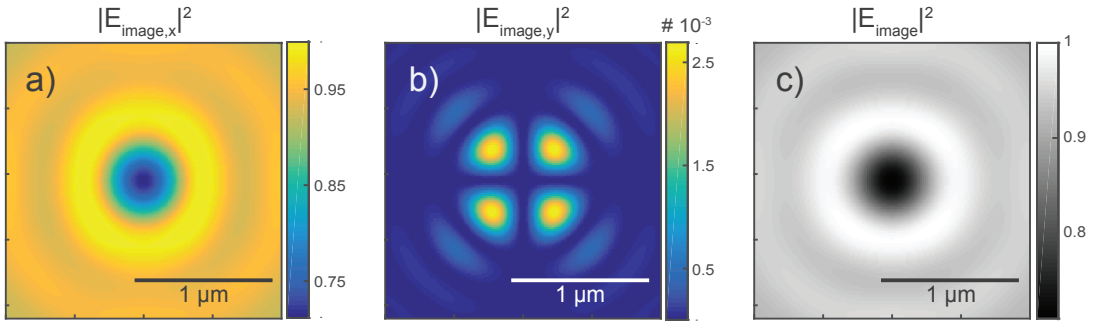

Figure 3.2: Electric field in the image plane of a standard wide field microscope considering a spherical scatterer. All graphs are normalized relatively to the max of $|\mathbf{E_{image}}|^2$. The characteristic of the system modelled are presented in table 3.1.

the data calculating in this work is shown but the results agrees with the data sent by Dr P. R. T. Munro. Hence, with this test it is validated that the implementation of the theory from section 2.2.2 is correct.

Differential interference contrast microscope's model validation

The last step to validate the MATLAB script is to certificate that the DIC's alterations are well implemented. The same approach that to validate the results for a wide field microscope was made. Dr P. R. T. Munro's data was used as reference to validate the model developed during this work.

The figure 3.3 represent the results from this validation step.

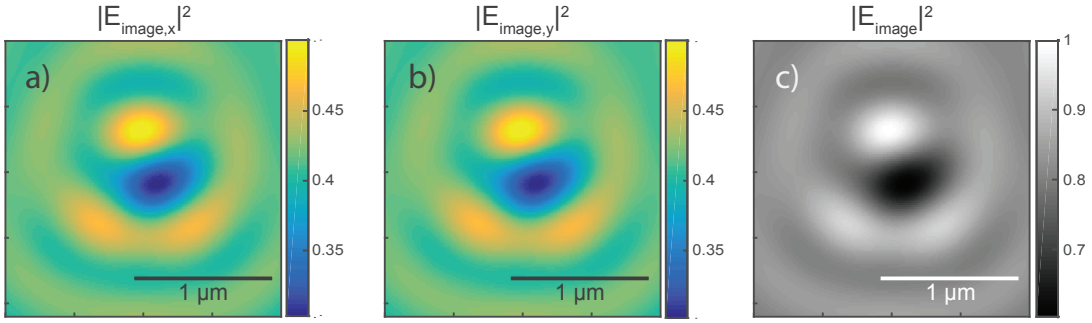

Figure 3.3: Electric field in the image plane of a DIC microscope considering a spherical scatterer. All graphs are normalized relatively to the max of $|\mathbf{E_{image}}|^2$. The characteristic of the system modelled are presented in table 3.1.

The calculated DIC's image is represented in the figure 3.3. As before, only the resultant data from the MATLAB script implemented during this work is shown but the results agree with the Dr P. R. T. Munro's data.

The multiple steps and validation procedure that were implement and made allows to have confidence about the results of the code developed. This way, it is possible to have confidence on the results advent from the ABV model and its application to a DIC microscope's model.

3.2 Samples preparation and characterization

To characterize the SLB impact experimentally it was elaborate two different systems and then study the respective DIC's image. Ideally, the only difference between the systems should be the shell anisotropy that cover the particles. The closest systems found it was considering silica spheres coated and uncoated with a SLB represented by the figure 3.4.

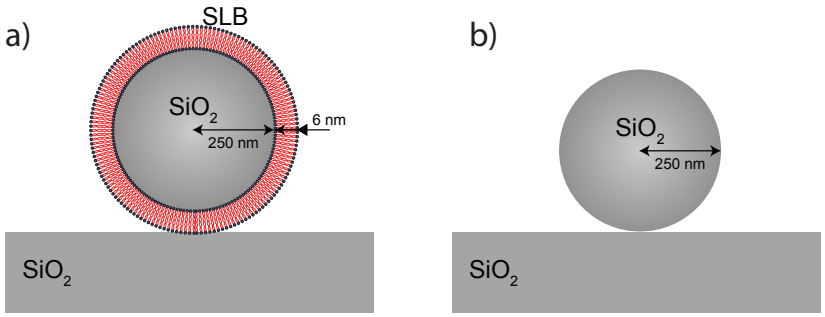

Figure 3.4: Representation of the expected anisotropic (a)) and isotropic (b)) geometries.

The systems of the figure 3.4 were chosen because the RI of silica is very similar to the anisotropic RI of the SLB. Considering a wavelength of 488 nm the RI are 1.4630 [52] for silica and the parallel and normal RI of the SLB are 1.45 and 1.46, respectively [9]. This factor allows to consider that the differences between the images of these two systems is due to the anisotropy itself and not to the change of the RI.

It is also important to specify that the thickness of the SLB is much smaller that the radius of the silica sphere hence it is valid to approximate that the change in the particle radius does not impact the light interaction.

The last factor that makes this system ideal for this work is that is known in literature procedure to create these samples with high accuracy regarding their proprieties.

Some part of the work regarding the sample preparation and characterization was made by Dr A. Miranda. Each part made by her is properly warned.

The first step to elaborate the samples represented in figure 3.4 consists in creating the silica spheres itself. This was achieve using the Stöber method with slight modifications [53]. This method allows the creation of silica sphere with a small distribution of radius which is important to ensure that the changes in the images are relatively to the anisotropy and not to the radius dispersion. The protocol is available in annex I.1 and was followed by Dr A. Miranda.

The paragraph before mentioned how the silica spheres were created. For the creation of the coated spheres it was first elaborated liposomes and then joined with the respective silica spheres in the conditions reported in literature [54]. As for the silica sphere, the detailed protocol is available in annex I.2 and was elaborated by Dr A. Miranda.

For observation under the microscope, a variable quantity of coated/uncoated silica sphere suspensions were deposited in an IBIDI dishes and left at room temperature

overnight undisturbed. These were then cleaned with calcium buffer solution prior to microscope observation. During the observation, it was used special DIC's IBIDI lid.

It is important to specify that the study made during this work is independent of the particles density over the dishes as long as the spheres are far apart. The density is only important to avoid the formation of cluster and to facilitate the image's analysis.

The two main points of the sample characterization is to ensure that the silica spheres have a low dispersion of radius and that the coated spheres have the respective and uniformly distributed SLB's shell. It is also important to calculate the radius of the spheres used and the thickness of the SLB to model the theoretical data according to the experimental parameters.

The size of the silica spheres was determined using Transmission Electron Microscopy (TEM) (section 3.2.1) and the study of the SLB shell using Cryo-Electron Microscopy (CryoEM) and zeta potential (sections 3.2.2 and 3.2.3 respectively).

3.2.1 Transmission electron microscopy analysis

TEM is a common technique to analyze systems at the nano scale. Principally to characterize geometries of non-living simples as the silica spheres used in this work. Due that it uses electrons, it can image systems much smaller that the diffraction limit of the light being ideal to analyse the silica spheres used in this work.

The goal is to use TEM to take images of the silica spheres that confirm their spherical shapes and allows the calculation of their radius. The images were capture by Dr A. Miranda using JEOL JEM 2100 microscope (JEOL USA, Inc., Peabody, United States) operated at 200 kV in carbon copper grids. The figure 3.5 a) and b) are TEM photographs without and with the respective analysis.

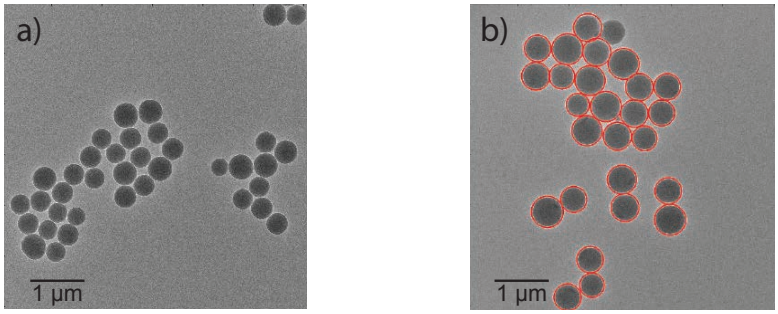

Figure 3.5: a) and b) are TEM photographs of the silica spheres. The figure b) consist in the analyzed image using the MATLAB script present in appendix B.1.

The respective statistical analysis of the TEM images was made by the author of this work. It consisted in the development of a MATLAB script which automatically calculate the radius dispersion of the spheres presented in the images. The code is available in appendix B.1. The author would like to acknowledge Sigworth for making his code to read .dm3 files available [55].

The results from the TEM analysis are presented in table 3.2.

Table 3.2: Results of the silica spheres radius using TEM images.

Number of spheres	Radius	Uncertainty
646	195 nm	18 nm

With the analysis of the TEM images it was possible to confirm the spherical shapes of the particles. The values of the radius dispersion calculated are higher that expecting since that the Stöber method usually has a low dispersion of the radius.

3.2.2 Cryo-electron microscopy analysis

With the recent advances in CryoEM, this technique is nowadays widely used in biophysics [56, 57]. The technique repose in the elaboration of TEM with samples at cryogenic temperatures which allows its application to biological samples contrary to the traditional TEM.

In this work CryoEM is used to verify the state of the SLB shell of the silica sphere as made in references [54, 58]. As for TEM images, the sample preparation and images acquisition were elaborated by Dr A. Miranda. Cryo samples were prepared using Vitrobot Mark IV (FEI, Hillsboro, United States) and analysed using JEOL JEM 2100 (JEOL USA, Inc., Peabody, United States) microscope operating at 200 kV, in carbon grids. A CryoEM photograph of a coated silica sphere is present in figure 3.6.

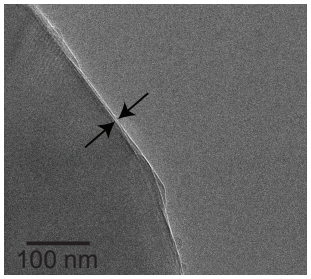

Figure 3.6: CryoEM photograph of a coated silica sphere.

By the analysis of the figure 3.6 it is possible to highlight the bright shell over the silica spheres. The table 3.3 has the average result for the multiple thickness measurements made in the CryoEM photographs. The images analysis was also made by Dr A. Miranda.

Table 3.3: Results of the SLB thickness using CryoEM images.

Number of measurements	Thickness	Uncertainty
6	7 nm	1 nm

The CryoEM results confirm the presence of the SLB over the silica spheres. The thickness value acquired also agrees with the value reported by the literature for a SLB [9].

3.2.3 Zeta potential

To characterize the proprieties of a double layer is highly common to measure the Zeta potential [59]. This chemistry technique is used in colloidal dispersions and it consist in measuring the potential in the interface particle-solution (more precisely in the slipping plane).

In literature, it is reported that the Zeta potential of silica spheres change if they are or not coated if a SLB [54]. Therefore, to confirm the presence of the SLB shell it was also measure the respective Zeta potentials. The experiment was made by Dr A. Miranda using Horiba Nano Particle Analyzer SZ-100 (Horiba Scientific, Kyoto, Japan). The average results for the coated and uncoated particles are presented in table 3.4.

Table 3.4: Results of the Zeta potential for the coated and uncoated spheres. The abbreviation N. Meas stands for number of measurements.

Uncoated particles			Coated particles		
N. Meas.	Zeta potential	Uncertainty	N. Meas.	Zeta potential	Uncertainty
9	−54 mV	1 mV	9	−11 mV	2 mV

The results obtained for both spheres agree with the results of Veneziano et al. [54]. Hence, the Zeta potential also validates the presence of the SLB shell over the silica spheres.

By the multiple characterization steps made to the sample it is then validate that the samples agree with what was expected. The geometries of the samples obtained are represented by the figure 3.7.

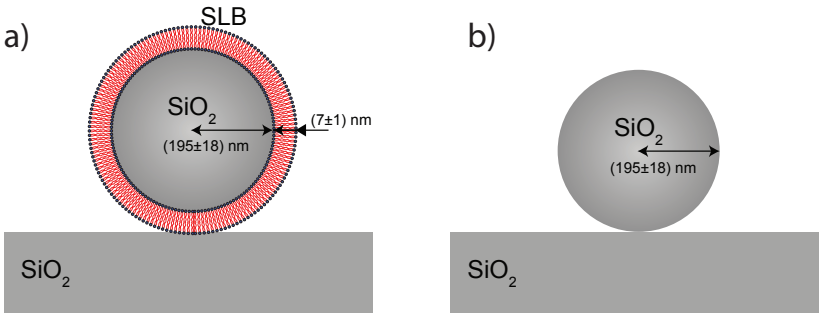

Figure 3.7: Representation of the obtained coated (a)) and uncoated (b)) geometries. The radius of the silica spheres was calculated throw TEM and the SLB thickness using Cryo-EM.

3.3 Optical systems

Until this point, it was characterized the samples used during this work. In this section, it is specified the equipments used to achieve the goals of this project.

To characterize the SLB impact in DIC microscopy it was used the microscope Zeiss LM780 (Carl Zeiss Microscopy GmbH, Jena, Germany). The study was made in two DIC strands: the traditional Nomarski DIC and the De Sérnamont DIC. Each of the setups are described in sections 3.3.1 and 3.3.2 respectively.

3.3.1 Nomarski differential interference constrast microscope

The traditional DIC origins from 1955 when Nomarski and Weill invented this type of microscopy [5]. Since then, it has been used principally in biology to observe almost transparent systems cells due that the image is highly sensible to changes in the optical path of the beams.

The Nomarski DIC setup used is represented by the figure 3.8.

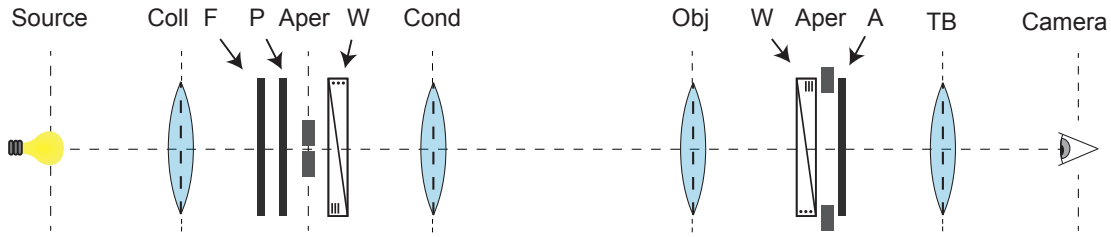

Figure 3.8: Schematic of the Nomarski DIC setup used in the experiments. The abbreviations stand for: Coll - Collector lens; F - Monochromatic filter; P - Polariser; Aper - Aperture; W - Wollaston prism; Cond - Condenser; Obj - Objective; A - Analyser; TB - Tube Lens.

As mentioned before, the DIC model of section 2.2 consists in a Nomarski DIC. Special attention was made to maximize the correspondence between the theoretical setup and the experimental. For that it was used a bright line singleband bandpass filter FF01-490/60-25 (Semrock Inc., New York, United States) to approximate the incident light to a monochromatic light. The condenser aperture was also used fully closed to provide an incident illumination that propagates parallel to the optical axis, as modelled in section 2.2.

The objective used consists in a water immersion objective ×40 with NA of 1.2 (Carl Zeiss Microscopy GmbH, Jena, Germany). The Wollaston prism in the back focal plane used is the respective one considering the objective used. The Charged Coupled Device (CCD) camera used was a 12 bits camera AxioCam MRm (Zeiss Microscopy GmbH, Jena, Germany).

3.3.2 De Sérnamont differential interference contrast microscope

The De Sérnamont DIC has the advantages that it is easily to use experimentally relatively to the Nomarski DIC. The difference lies in the De Sérnamont compensator inserted in the back focal plane of the microscope. A schematic of this DIC strand is available in figure 3.9.

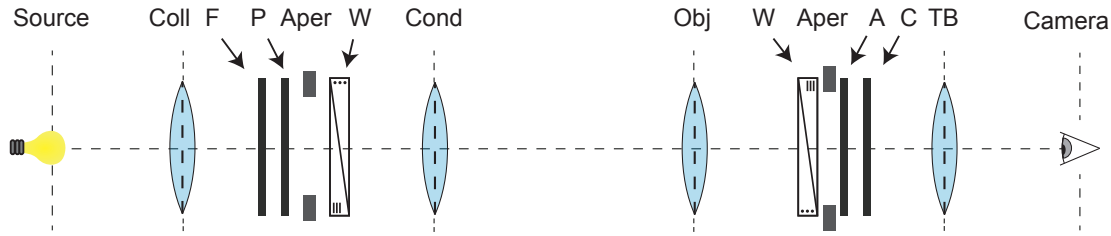

Figure 3.9: Schematic of the De Sérnamont DIC setup used in the experiments. The abbreviations stand for: Coll - Collector lens; F - Monochromatic filter; P - Polariser; Aper - Aperture; W - Wollaston prism; Cond - Condenser; Obj - Objective; A - Analyser; C - De Sérnamont Compensator; TB - Tube Lens.

Comparing the figure 3.9 and 3.8 it is possible to see the difference between the systems used. As mentioned before, the principal difference is the insertion of the De Sérnamont compensator in the back focal plane.

The DIC contrast changes with the induction of the bias. In Nomarski DIC the bias is controllable by shifting the Wollaston prism relatively to the optical axis (section 2.2.3.1). An easier way to achieve and control the bias is throw the insertion of the De Sérnamont compensator in the back or front focal plane [60]. In literature, it is not really consent the ideal bias that maximize the contrast of the image [8, 15, 61, 62].

The other difference relatively of the Nomarski setup used in this work is that the condenser's aperture is fully open so the incident light is focused by the condenser which has a NA of 0.55. The rest of the components are the same that used for Nomarski DIC.

3.4 Image analysis

During this section, it is discussed how the DIC image were analyzed in order to quantify the anisotropic effect. The goal is to determine the histogram of the individual spheres. In this section, it is explained step by step the procedure to arrive to the respective histogram.

It was developed a small Graphical User Interface (GUI) under MATLAB to make the image analysis using MATLAB image toolbox. This GUI allows the user to remove the background according with the explanation bellow and also enables the user to make multiple crops over single spheres. Then the user can easily generate the histogram of all crops and make the respective fit. The author want to acknowledge Yeh for making available his MATLAB script to read *.lsm files [63].

The figure 3.10 represents the main steps of the image analysis to arrive to the image characterization.

The image analysis overview represented by the figure 3.10 shows without going in detail the principal steps: first it is required to remove the background (figure 3.10 b)) so that the spheres data is not hidden by the background (in the histogram) then it is required to make individual crops to each sphere (figure 3.10 c)). In this step, it is

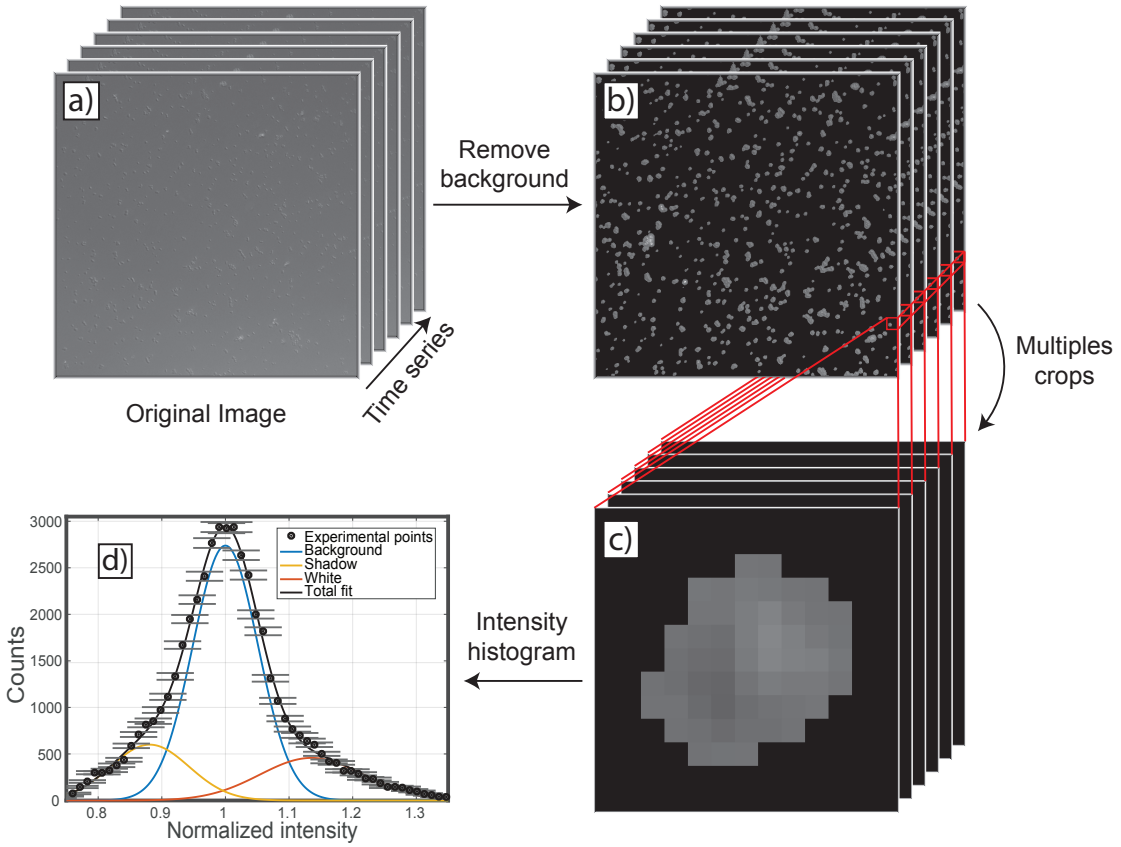

Figure 3.10: Schematic of the main steps of the image analysis. a) represents the original time series images taken from the microscope; b) represents the respective time series images a) without the background; c) represents a crop of a silica sphere from the images b); d) represents the histogram of a large number of crops as image c).

required to just select individual and not considering the data from clusters. To acquire quantitative data it is then calculated the histogram of all crops to make the respective fits. More detail about each step is explained in the next paragraphs.

The figure 3.10 also suggests that the data obtained in the microscope consist in a time series of photographs. Using time series instead of a single image allows to consider the time fluctuations of the image (noise) in the analysis making the study more precise.

3.4.1 Zones of interest

Keeping in mind the main steps showed in figure 3.10 the first step consists in removing zones without interest of the image. The figure 3.11 represents how this was achieved.

Using figure 3.11 as a guidance it is in the next paragraphs explained the algorithm chosen to remove the zones without interest. Analysing the figure 3.11 a) is possible to see that big changes in pixels intensity (relatively to its neighbours) only occurs in the presence of spheres. That means, that the background is consistent with its neighbours. Hence creating the gradient image, it is possible to obtain the localization of the spheres

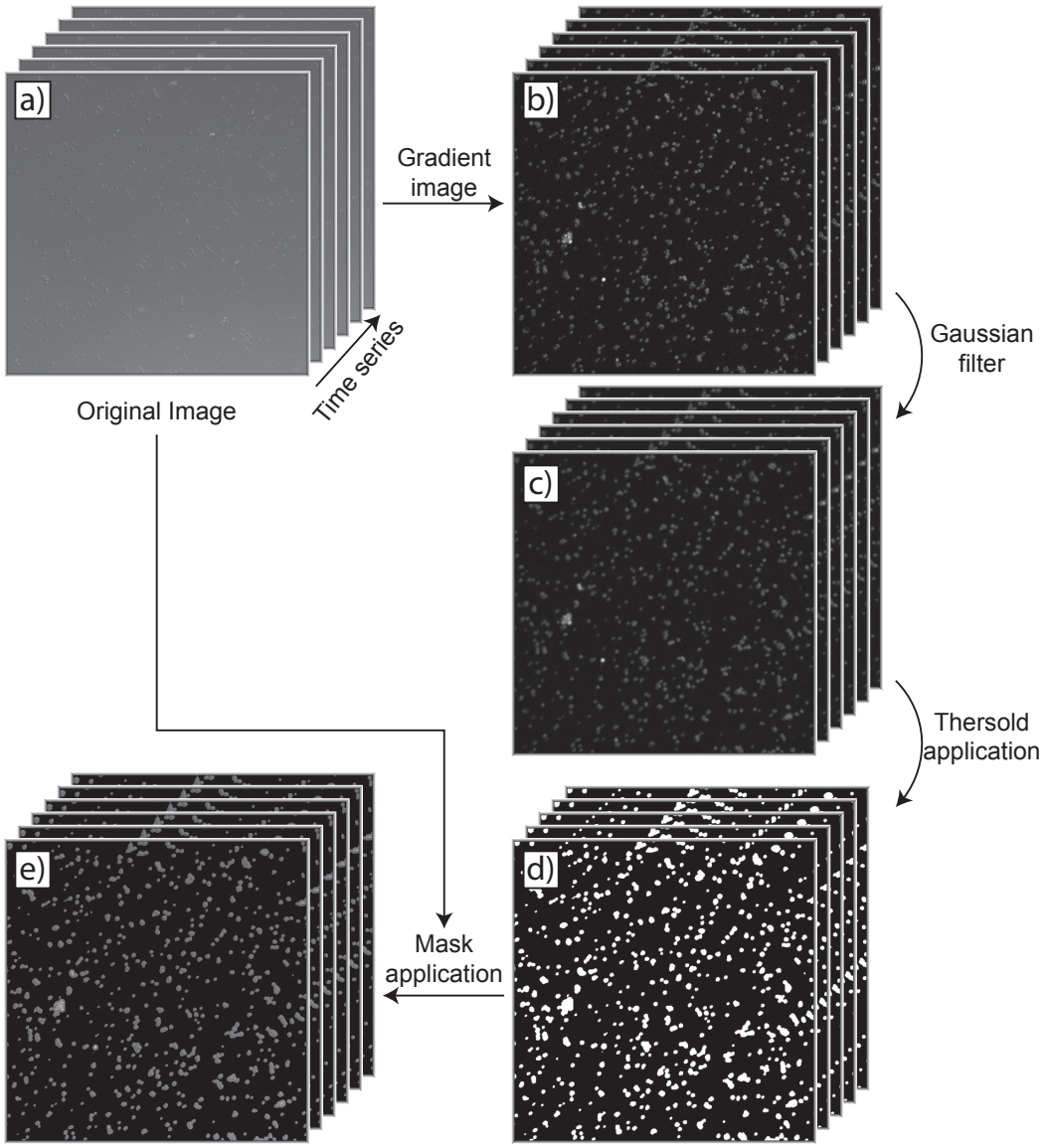

Figure 3.11: Schematics of the multiple steps to remove the zones without interest from the original time series images. a) represents the original time series taken from the microscope; b) is the gradient magnitude of the images a); c) represents the images b) after the application of a Gaussian filter; d) represents the images c) after the application of a threshold converting the images to masks (logical image); e) represents the combination of the images a) and e).

(figure 3.11 b)).

At the gradient image it is then applied a Gaussian filter which has two purposes: first it decreases the intensity of isolated peaks (can be in the background zone) and principally it slightly increase the radius of the spheres zone.

The figure 3.11 c) contains now the information about the localization of the zone of interest. At this point is necessary to create a mask image (logical image) with this information. This can be done by applying a threshold to the figure 3.11 c) which origins the figure 3.11 d).

An important point is that the analysis has to be done in the original image without any filter or alterations. Therefore, using the figure 3.11 d) as a mask to the original figure 3.11 a) it is finally arrived to the figure 3.11 e) which has the original intensity of the microscope's image but fully black in the background.

The algorithm developed and used during this work to remove the background is available in appendix B.2.

3.4.2 Individual sphere

Taking the masked images created as explained in the section above it is now required to extract crops from the image containing isolated spheres. The GUI developed has done to facilitate this process allowing to make small crops in the principal image in a relatively fast way. The figure 3.12 is a schematic of the process from the image without background to a single sphere histogram.

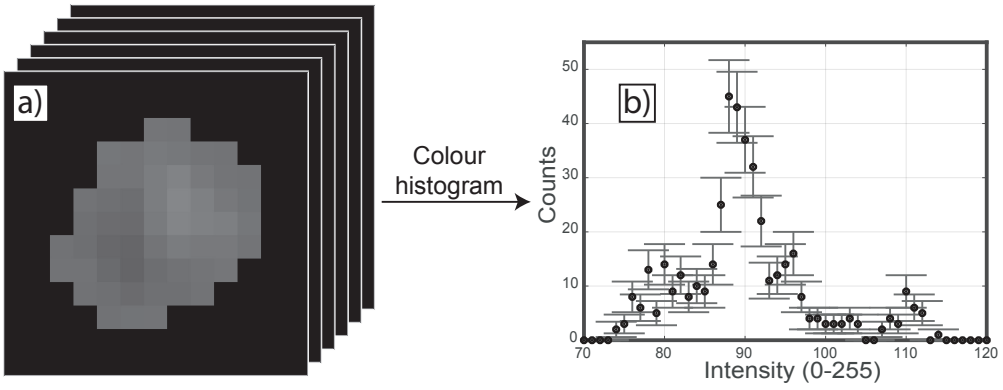

Figure 3.12: Schematic of the image analysis for a single sphere. a) represents the crop of an individual sphere; b) is the histogram of the images a). It is considered a time series of 10 frames.

Making a small crop over a silica sphere in the image without background (figure 3.10 b)) it results in the figure 3.12 a). This image gives the intensity of the pixels that form the sphere's image. One of the goals of this work is to then compare these pixels of the coated and uncoated silica spheres. For this purpose, it is important to make the histogram of the respective image, represented in figure 3.12 b), to get some quantitative data.

A analysis over multiple spheres is required to get some confidence on the results. An histogram considering multiple crops of spheres is represented in figure 3.10 d). To compare then the components of the coated and uncoated spheres it is required to fit the experimental data.

As it is characteristic of a DIC's image, it is possible to see in figure 3.12 a) a shadow and white shape. Therefore it was assumed pertinent that the histogram's fit should be done to three Gaussian functions: one for the shadow, other to the background and at last to the white component. The quantitative values of the fitted parameter are represented normalized relatively to the background peak as in figure 3.10 d).

3.4.3 Distance between shadow and white peaks

As already mentioned, a DIC's image consists in the superposition of the white and shadow part of the image which are both separated by a well-defined bias. This last one is defined principally by the Wollaston prisms that are used. Since that it is another propriety of the image it is also pertinent to see if the anisotropy has an effect on it.

The process to calculate the distance between the white and shadow part (Γ) is represented in figure 3.13.

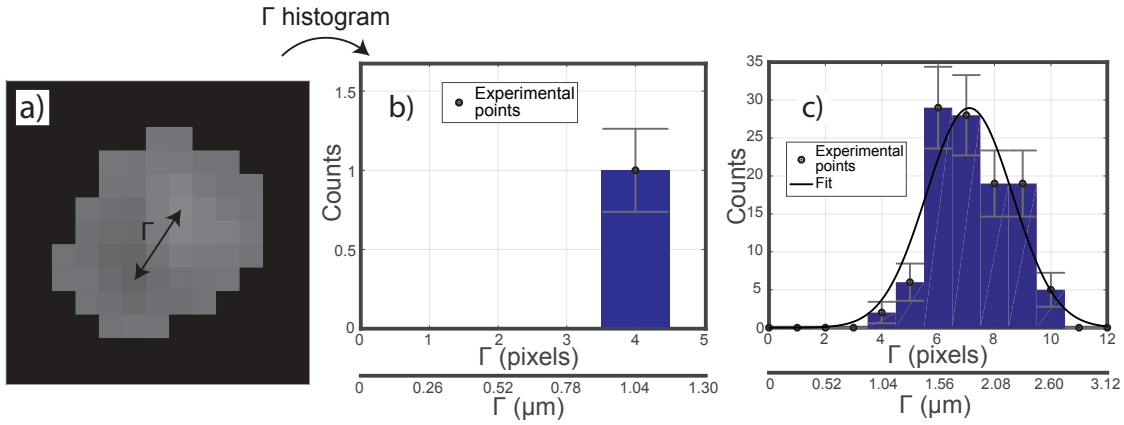

Figure 3.13: Schematic of how it is calculated the distance between the shadow and white part. The origins of the arrow of a) represent the darker and brighter pixels. b) represents the Γ histogram of the image a). c) is a Γ histogram of a large number of spheres with the respective Gaussian fit.

As figure 3.13 suggests the distance Γ is measured by considering the distance between the brighter and darker pixel of the sphere crop. Considering a huge number of crops, like for the intensity histogram, it is possible to arrive to Γ distribution which can be then fitted to a Gaussian curve (figure 3.13 c)). For the calculation of Γ it is just considered the first frame of the time series.

Finally the analysis protocol is complete: with it is possible to arrive to some quantitative parameters of the DIC's image. And they can be used to compare the coated

and uncoated sphere's images to then evaluate the effect of the SLB in the DIC's image formation.

Chapter 4

Results and discussion

This chapter owns all results acquired in this work more specifically, it is divided in two section were it is firstly explained the SLB anisotropy impact in the ellipsometry angles Ψ and Δ and then the SLB impact in the DIC image formation process.

4.1 Ellipsometry results

In this section, it is presented the results of modelling where it is studied the influence of the SLB anisotropy in the scattered far field. A scientific article to a peer review journal already had been submitted with the results presented in this section [64].

Considering an ABV which represents a liposome above a cell there are two anisotropic materials: the SLB that covers the vesicle and the SLB above the substrate. Therefore, to quantify how SLB affects the scattering proprieties it is introduced two different geometries which are presented in figure 4.1.

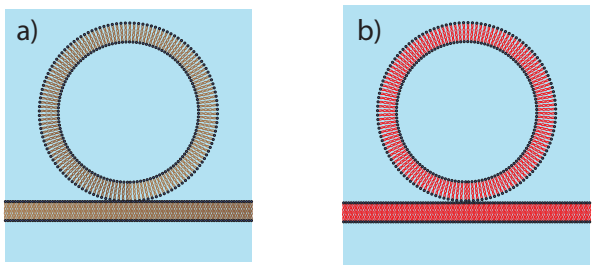

Figure 4.1: Representation of the geometries used to quantify the anisotropy effect. a) - Isotropic Thin Film with an Isotropic Shell (ITFIS) and b) - Anisotropic Thin Film with an Anisotropic Shell (ATFAS). The brown SLB represents an isotropic material with RI given by equation 2.11 and the red SLB represents a SLB with its real optical proprieties.

The model Isotropic Thin Film with an Isotropic Shell (ITFIS) (figure 4.1 a)) is here

introduced as a reference to compare the results with the anisotropic case. Comparing the data between the models ITFIS and Anisotropic Thin Film with an Anisotropic Shell (ATFAS) (figure 4.1 b)) gives impact of the anisotropy in a specific data.

Using the definitions of the ellipsometry angles it is quantified how the SLB anisotropy affects the scattered far field. It is considered the light is being analysed in the reflected specular condition and were calculated using SCATMECH classes developed during the work.

If otherwise noted, all default parameters of the model used in this section are listed in table 4.1.

Table 4.1: Default simulation ellipsometry parameters. The nomenclature agrees with figure 2.6 b).

Model parameter	Value	Model parameter	Value
θ_i	70°	λ	488 nm
M	1 µm^{-2}	$N_s = n_i = N_{sphere}$	1.335
r_{sphere}	95 nm	$d^{tf} = d^{co}$	5 nm
$N_{\perp}^{tf} = N_{\perp}^{co}$	1.46	$N_{\parallel}^{tf} = N_{\parallel}^{co}$	1.45
$N_{avg}^{tf} = N_{avg}^{co}$	1.4533	δ	0 nm

Ellipsometry curves are traditionally made measuring the angles throw the AOI or the wavelength used. In the next sections are made the study of the anisotropy effect in both cases (sections 4.1.1 and 4.1.2). Then, it is analysed how the incident medium and substrate affects the anisotropy impact (section 4.1.3) and at last how the anisotropy impacts the endocytosis observation (section 4.1.4)

4.1.1 Resolving angle of incidence dependence

In the present section, it is presented the ellipsometry data modelled considering an AOI revolving measurement. The main goal is to quantify the anisotropic impact due to the SLB which is achieved comparing the ellipsometry curves from the models ATFAS and ITFIS. The results are illustrated by the figure 4.2.

AOI revolving ellipsometry angle Ψ (figure 4.2 a)) shows that the optical anisotropy becomes more pronounced for increasing the AOI with a ∼1° at AOI 30° discrepancy between anisotropy and the correspondingly isotropic model as compared to ∼3° at AOI 80°.

With the analysis of Δ over the AOI (figure 4.2 b)) it is highlighted that the value of AOI when Δ changes from ∼180° to ∼0° goes from ∼47° to ∼46° due to the anisotropy. The anisotropy also impacts at higher AOI but this depends on the particle radius.

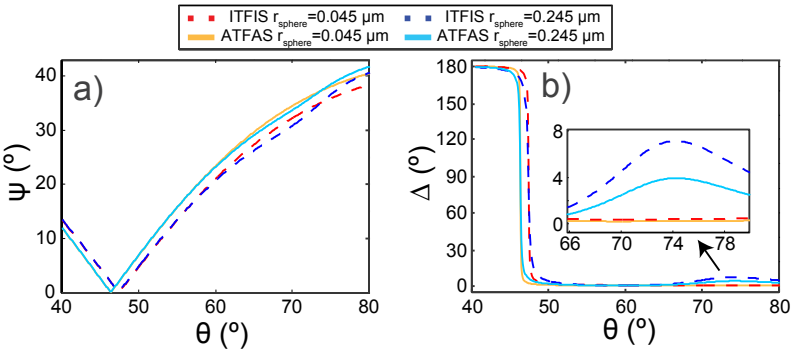

Figure 4.2: Resolving AOI ellipsometry angles Ψ (a)) and Δ (b)) of the models ITFIS and ATFAS considering radii of 50 nm and 250 nm. The other simulation parameters are presented in table 4.1.

4.1.2 Resolving wavelength dependence

Spectroscopic ellipsometry is made measuring the angle Ψ and Δ throw the incident light wavelength. Figure 4.3 depicts spectroscopic ellipsometry curves considering the geometry ITFIS and ATFAS allowing the quantification of the anisotropy impact.

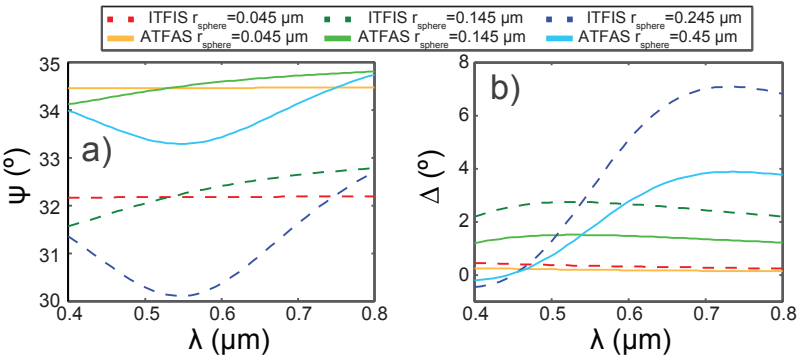

Figure 4.3: Resolving wavelength ellipsometry angles Ψ (a)) and Δ (b)) of the models ITFIS and ATFAS considering radii of 50 nm, 150 nm and 250 nm. The other simulation parameters are presented in table 4.1.

Spectroscopic ellipsometry modelling data shows that, considering small particles with a small radius, Ψ (figure 4.1 a)) has an offset around ~2.5° due to the anisotropy. This offset start to be non-constant if it is considered bigger particles.

Very similar behaviour occurs with Δ but with it, the oscillation due to the anisotropy is much bigger when compared with the initial offset. Indeed, considering a radius of 50 nm the constant offset its around ~0.3° while that, with particles radius of 250 nm the maximum of the anisotropy impact is around ~3° at a wavelength of 0.7 µm.

There are many obstacles to measure experimentally the results from figures 4.2 or 4.3 as the sample polydispersity, vesicle aggregation, Poisson statistic of the particle density and the difficulties of having well defined isotropic and anisotropic shells around a perfectly homogeneous core and other sample homogeneities. However, figures 4.2

and 4.3 show the capacity of small values of anisotropy to modify the phase and amplitude of the reflected waves.

4.1.3 Changing incident medium and substrate

In this section is study how the incident medium and the substrate of the geometry influence the anisotropic effect. For this study it is not used the ABV model but it is just considered a substrate with a thin film above, as represented by figure 4.4.

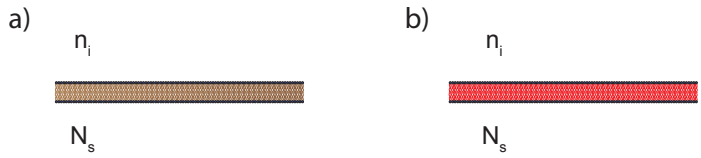

Figure 4.4: Models used to quantify the influence of the substrate and the incident medium in the anisotropic effect. a) - Isotropic Thin Film (ITF) model; b) - Anisotropic Thin Film (ATF) model. The brown SLB represents an isotropic material with RI given by equation 2.11 and the red SLB represents a SLB with its real optical proprieties.

The figure 4.4 shows the models used for this study. The principle is the same that for the figure 4.1, it is used the Isotropic Thin Film (ITF) model (figure 4.1 a)) as reference to compare with the Anisotropic Thin Film (ATF) model (figure 4.1 b)) which represents the anisotropic case.

Some of the data in this study is represented in the form of the ellipsometry angles differences D_Ψ and D_Δ for AOI resolved ellipsometry measurements. They are both defined by equation 4.1 and 4.2, respectively.

$$D_\Psi = \sum_{i=1}^{n} \frac{|\Psi_{ATF}(\theta_i) - \Psi_{ITF}(\theta_i)|}{n} \tag{4.1}$$

$$D_\Delta = \sum_{i=1}^{n} \frac{|\Delta_{ATF}(\theta_i) - \Delta_{ITF}(\theta_i)|}{n} \tag{4.2}$$

To study the substrate and incident medium influence it was made a numerical study where it was changed the incident medium and the substrate and measured the ellipsometry angles differences D_Ψ and D_Δ.The figure 4.5 represents the respective study.

Figure 4.5 depicts modelling results D_Ψ and D_Δ for different substrate and incident medium. Each pixel of the figure 4.5 a) and b) corresponds to an curve AOI resolving ellipsometry curve. In figure 4.5 a) and b) it is possible to distinct three regions according to the impact of the SLB anisotropy being strong, weak and negligible, respectively: 1) $N_\perp^{tf} \sim N_\perp^{tf} \sim N_{avg}^{tf}$, 2) $N_\perp^{tf} \sim N_\parallel^{tf} \nsim N_{avg}^{tf}$ and 3) $N_\perp^{tf} \nsim N_\parallel^{tf}$.

The three example of figures 4.5 c) and d) correspond to the curves marked in figures 4.5 a) and b). Example 2) correspond to the case of a SLB in an aqueous media being possible to conclude that the small anisotropy of a lipid bilayer has a relatively significant impact in the reflected scattering polarization properties.

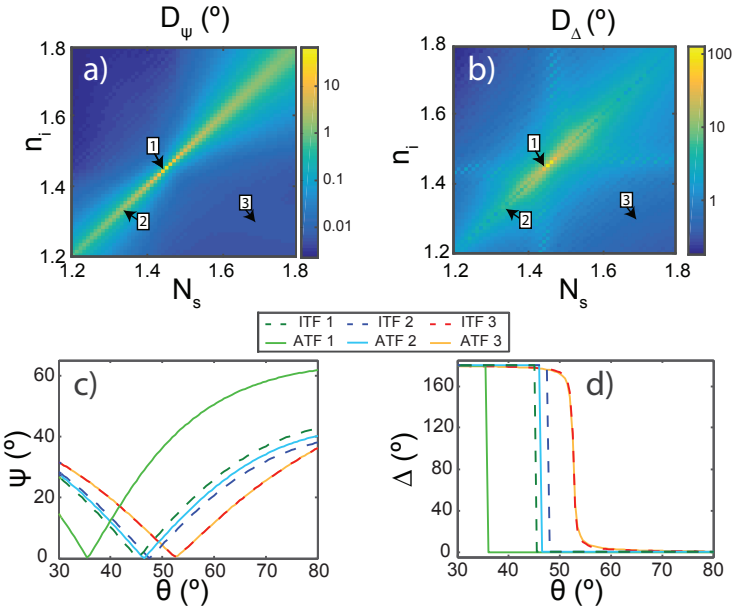

Figure 4.5: D_Ψ (a)) and D_Δ (b)) for AOI resolved ellipsometry from 30° to 80° for different values of incident and substrate RI; AOI resolved Ψ (c)) and Δ (d)) profiles considering ATF and ITF geometries.

It should, however, be noted that the zone 1) represents the case of an homogeneous sample, so while the effect under investigation becomes larger it becomes increasingly challenging to observe experimentally.

4.1.4 Endocytosis model ellipsometry results

The results presented above suggests that SLB anisotropy has a significant impact considering the endocytosis geometry. The figure 4.6 is the evolution of the ellipsometry angles when the distance δ increases. To quantify the anisotropic impact, it is represented the data for the model ITFIS and ATFAS.

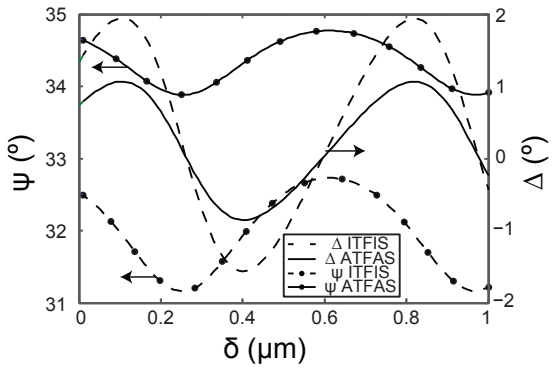

Figure 4.6: Ellipsometry angle Ψ and Δ of a liposome above a SLB for varying distance between the liposome and SLB δ. The isotropic and anisotropic data are considering the ITFIS and ATFAS models, respectively.

The Ψ and Δ curves present in figure 4.6 exhibits a sinusoidal-like behavior with a period of $\sim 700\,nm$. This behavior occurs due to the constructive and destructive interference between the light reflected at the top of the particle and at the substrate.

Comparing the isotropic and anisotropic curves of figure 4.6 it is possible to notice that the SLB anisotropy induces a constant shift of $\sim 2°$ in Ψ. Contrary to Δ curves where the anisotropic impact consists in decreasing the sinusoidal amplitude around $\sim 0.5°$.

As the studies presented before, the figure 4.6 also confirms that the SLB anisotropy has a big impact in the reflected scattered field, unless in the conditions studied.

4.2 Differential interference contrast images

Results from the SLB impact in DIC microscopy are presented in this section. As planned for this work, in section 4.2.1, it is presented experimental and theoretical data to evaluate the SLB impact and the effect of its anisotropy. At last, though the numerical implementation, it is studied the observation of endocytosis using DIC microscopy (section 4.2.2).

A manuscript to a peer review journal with the results from this section is in preparation [65]

4.2.1 Supported lipid bilayer impact

This section discuss in detail the SLB impact on the DIC image formation process. For this purpose it is compared theoretical and experimental data of three geometries based on the figure 3.7 of page 41. Figure 4.7 illustrated the three geometries used in this section.

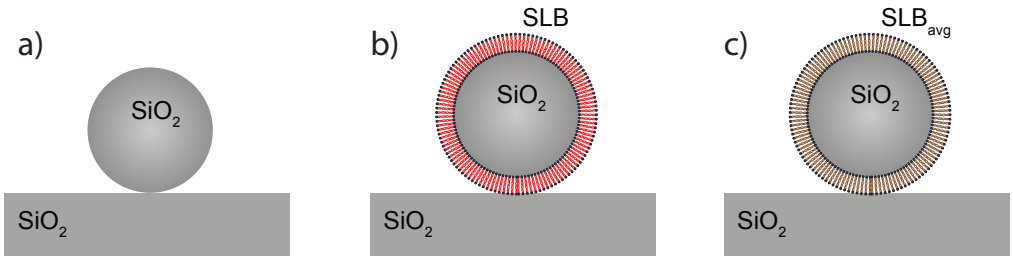

Figure 4.7: Geometries used to quantify the effect of a SLB and its anisotropy in DIC. a) represents uncoated silica spheres (geometry NC), b) represents the coated silica spheres (geometry C) and c) represents the coated silica spheres considering the average RI (geometry C_{avg}).

The same rational than for the geometries used in ellipsometry is applied: the difference between the geometry NC and C is due to the presence of the SLB while the difference between the geometry C and C_{avg} is due at the SLB anisotropy. It is important to enhance that the while the geometries NC and C are available experimentally the geometry C_{avg} is only theoretical.

Considering that the goal is to compare the theory with the experiment it is provide in table 4.2 the DIC and sample parameters that match the experimental setup used.

Table 4.2: Default simulation parameters of the experimental setup used considering the sample from figure 4.7. The denomination agrees with the figures 2.6 b), 2.10, 2.16 and 2.17 of pages 13, 21, 29 and 30.

Model parameter	Value	Model parameter	Value
$\mathbf{E_i}$	(0.7071, 0.7071, 0)	λ	488 nm
$N_{\parallel}^{co}$	1.45	r_{sphere}	195 nm
$N_{\perp}^{co}$	1.46	d^{co}	7 nm
$N_s = N_{sphere}$	1.463	β	40
n_i	1.333	$\theta_i = \phi_i$	0 rad
α_{obj}	$\frac{\pi}{3}$ rad	x_s	200 nm
Φ_b	$\frac{\pi}{4}$ rad	γ	$\frac{3\pi}{4}$ rad
δ	0 nm		

Unfortunately, even after contacting Zeiss to get more information about some DIC parameters, some data as x_s and Φ_b had to be considered the typically used in this type of microscopy.

It is first discussed the results of the SLB impact in the theoretical results (section 4.2.1.1) and then the experimental data and respective analysis is presented (section 4.2.1.2).

4.2.1.1 Numerical results

The utilization of the DIC model associated with the ABV model allows the theoretical characterization of the anisotropy throw numerical simulations. Throw this section, it is analysed the SLB impact theoretically starting by the effect in the objective's electric far field and then its impact in the image in multiple configurations.

Far field impact

As explained in section 2.2.3, the modulation of a DIC is made considering two independent orthogonally polarized beams and their interference in the image plane. Therefore, each of the beam has its respective objective's far field. The figure 4.8 represents the far field of the x and y beams considering the NC and C geometries of figure 3.7.

Figure 4.8 depicts the SLB impact on the far field. There are two main conclusion from this figure: first the fact that the far field intensity increases around 15% due to the SLB anisotropy (comparing figure 4.8 a) with b) and d) with e)). Then the figures 4.8 c) and e) allow to conclude that the SLB impact is more important when considering small value of θ_{obj}. This shows that possibly the image is more susceptible to the SLB in microscope with low NA objectives.

Image impact

In the paragraphs above it was quantified the anisotropy effect in the objective far field. At this point, it is then propagate the electric field over the DIC optical system to calculate

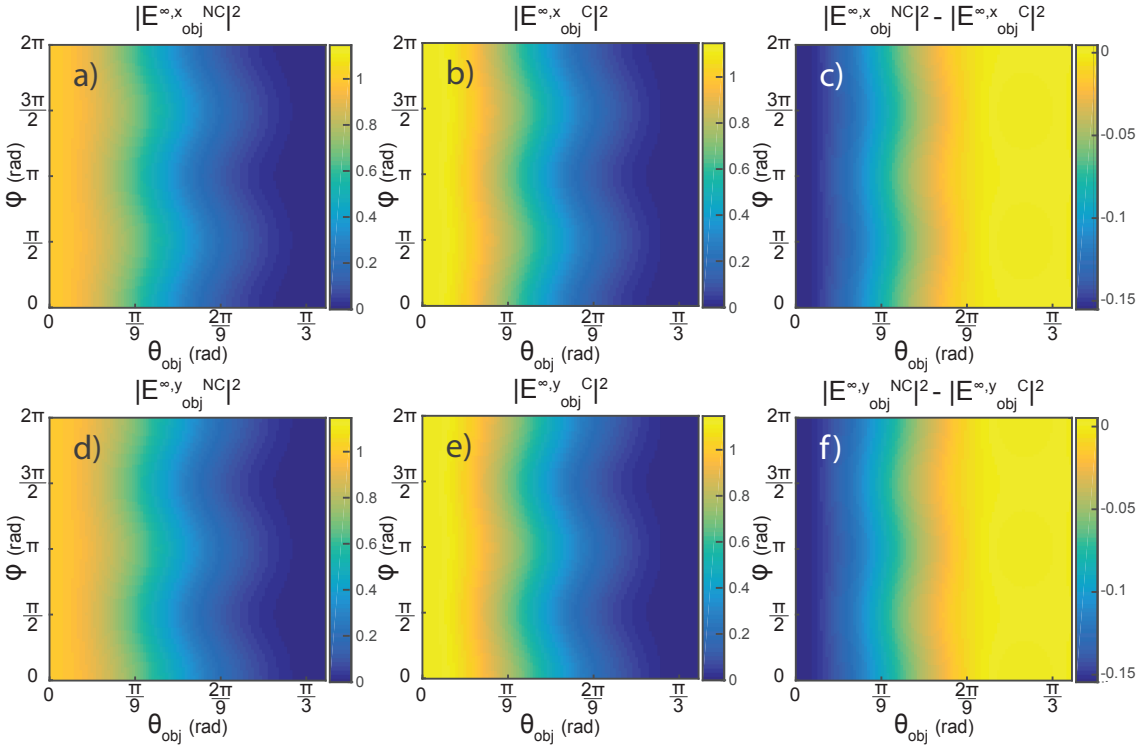

Figure 4.8: Objective's far fields considering the NC (a) and d)) and C (b) and e)) geometries of figure 3.7 for the x (a), b) and c)) and y (d), e) and f)) polarized beams. c) and f) represent the difference between the NC and C case. All graphs are normalized relatively to the respective NC maximum $|\mathbf{E_{obj}}^{\infty NC}|^2$. The simulation parameters are represented in table 4.2.

the resultant image. This way it is possible to quantify SLB impact in the image plane which is represented by figure 4.9 considering an objective with 1.2 NA.

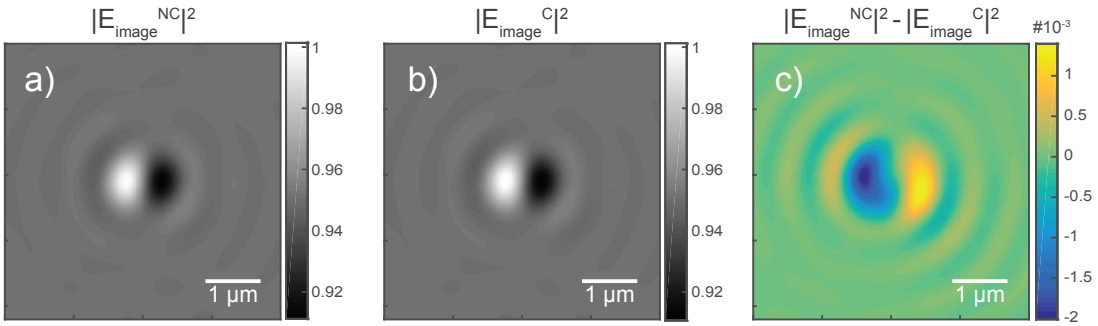

Figure 4.9: Theoretical DIC image of NC and C geometries considering a high NA objective. c) represents the difference between the NC (a)) and the C (b)) images. All graphs are normalized relatively to $|\mathbf{E_{image}}^{NC}|^2$ maximum. The simulation parameters are represented in table 4.2.

Visually there is no difference between the images of figure 4.9 a) and b). But making the differences between the images a) and b) of figure 4.9 it results in c) which shows that the anisotropy induces very small changes considering this system. From these results

it is possible to conclude that the SLB impact (around 10^{-3}) is impossible to analyse considering that the usual cameras scales are between 0 and 255.

However , from the far field results illustrated by figure 4.8 and as notice before, it suggests that the SLB impact is bigger considering small values of θ_{obj}. Therefore, an analysis considering a DIC microscope with a objective with small NA (0.1736) is illustrated in figure 4.10.

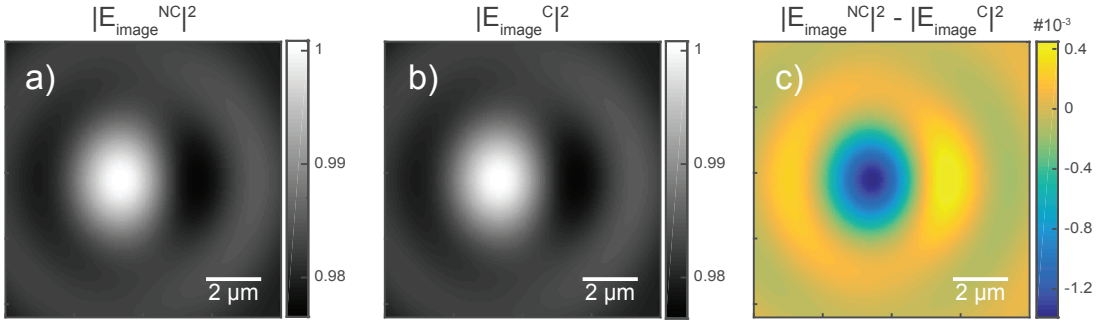

Figure 4.10: Theoretical DIC image of NC and C geometries considering a low NA objective. c) represents the difference between the NC (a)) and the C (b)) images. All graphs are normalized relatively to $|\mathbf{E_{image}}^{NC}|^2$ maximum. The simulation parameters are represented in table 4.2.

Figure 4.10 a) and b) shows the resultant image of the NC and C geometries. Comparing these figures with the figure 4.9 a) and b) it is clear the reduction of the resolution. The dependence of the microscope resolution with the objective and condenser NA is very well known in optics [66]. Another particularity is the decrease of the contrast (color scale) of the image.

The SLB impact shown by figure 4.10 c) is smaller than in figure 4.9 c) which does not agree with the prevision. But, even if in terms of intensity difference the impact is smaller, in term of image contrast it is bigger. That means that taking into account the contrast using a small NA objective, which is five times lower that with high NA, the relative intensity variations due to the SLB is around two times bigger than using high NA objective.

Further work could be to investigate how the condenser NA influence the SLB impact. In the case that the SLB impact increases when the incident light is not propagating normal to the optical axis, it could be used an annular ring in the front focal plane to measure the SLB impact.

Bias influence

The next paragraphs study throw the DIC model if the bias used affects how SLB impacts the image formation. To evaluate this it is here introduced the term Ω defined by equation 4.3.

$$\Omega = \sum_x \sum_y ||\mathbf{E_{image}}^{NC}(x,y)|^2 - |\mathbf{E_{image}}^{C}(x,y)|^2| \tag{4.3}$$

,where $|\mathbf{E_{image}}^{NC}|^2$ and $|\mathbf{E_{image}}^{C}|^2$ are the normalized intensity relatively to $|\mathbf{E_{image}}^{NC}|^2$ maximum of the image considering the NC and C geometries, respectively.

To quantify the impact of the bias it was determined Ω changing the bias used between $\frac{-\pi}{2}$ rad to $\frac{\pi}{2}$ rad. Figure 4.11 illustrates the respective graph.

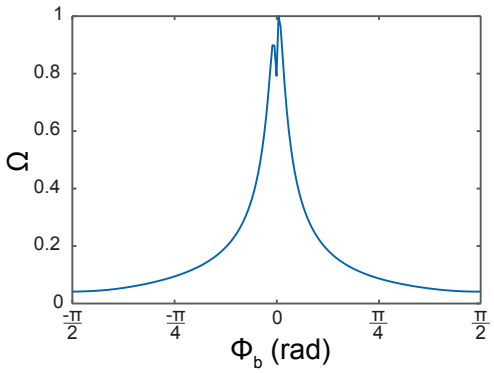

Figure 4.11: Relation between the bias of the DIC microscope and the SLB impact. The data is normalized relatively to the respective maximum.

The graph of the figure 4.11 shows that the bias used has a particular and significant impact regarding how the SLB affects the image formation. Indeed, at small values of bias the SLB has a much bigger impact in the DIC images contrary to when the bias is around $\pm\frac{\pi}{2}$ rad.

Considering that the figures 4.9 and 4.10 are for a bias of $\frac{\pi}{4}$ rad, the figure 4.11 suggests that it is possible to increase the SLB impact around ten times using a bias around $\frac{\pi}{100}$ rad. The respective images, considering a bias of $\frac{\pi}{100}$ rad, are represented in figure 4.12.

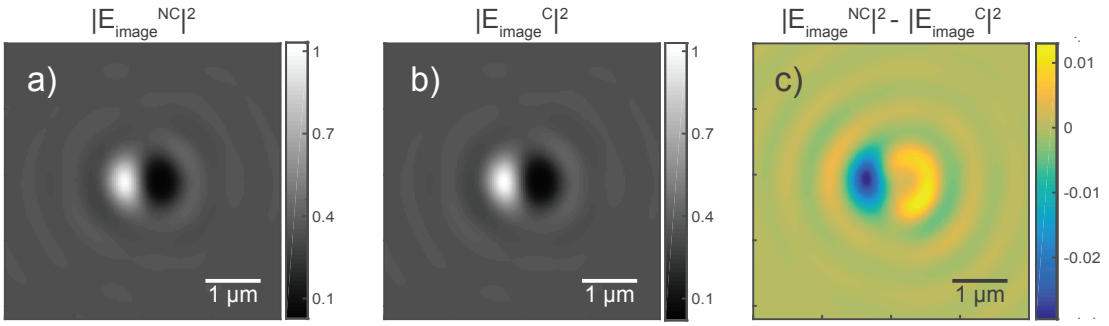

Figure 4.12: Theoretical DIC image of NC and C geometries considering a bias of $\frac{\pi}{100}$ rad. c) represents the difference between the NC (a)) and the C (b)) images. All graphs are normalized relatively to $|\mathbf{E_{image}}^{NC}|^2$ maximum. The other simulation parameters are represented in table 4.2.

Figure 4.12 depicts DIC theoretical images of the NC and C geometries considering a small bias. One of the conclusions from this image is that small values of bias generate much bigger contrast for the system in study. Indeed, in figure 4.12 a) and b) the contrast is around ten times bigger than in figure 4.9 a) and b).

The second conclusion is that the SLB impact is relatively high considering this setup. Figure 4.12 c) shows variations in intensity around 3% which can already be detected using an 8 bits camera ($\frac{1}{256}$=0.0039). Also important is that the SLB increases the contrast of the image, in other words, the shadow becomes darker and the white part becomes brighter.

One goal of this work is to quantify how anisotropy impacts the image formation. In this chapter, it was only quantified the impact of a SLB. Figure 4.13 presents two DIC theoretical images considering the geometries C and C_{avg} and the respective difference between them.

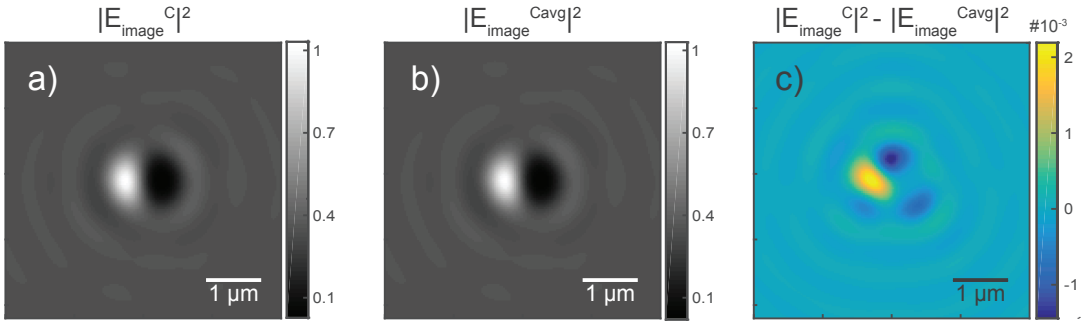

Figure 4.13: Theoretical DIC images to quantify the impact of the SLB anisotropy in the images. a) is the image of the geometry C, b) is the image of the geometry C_{avg} and c) is the intensity difference between a) and b). All graphs are normalized relatively to $|\mathbf{E_{image}}^{NC}|^2$ maximum (figure 4.12 a)). The respective parameters of the simulation, in exception of Φ_b=$\frac{\pi}{100}$ rad, are presented in table 4.2.

Figure 4.13 a) and b) show two DIC images considering the SLB as an anisotropic and isotropic material, respectively. Then, the intensity difference between them is represented by figure 4.13 c). Visually, it is not possible to see the differences between figure 4.13 a) and b). Indeed, figure 4.13 shows that the anisotropic impact is only around 10^{-3}. Even if it would be possible to create a sample as geometry C_{avg} an 8 bits camera would not be precise enough to measured such small differences, being necessary a 16 bits camera.

4.2.1.2 Experimental results

The data obtained experimentally during this work is presented in this section. Having in mind what mentioned in section 3.2, it is discussed the results of the C and NC geometries (figure 3.7 of page 41) on two DIC strands: Nomarski and De Sérnamont DIC.

Nomarski differential interference contrast

The images and respective analysis of the C and NC images are presented bellow. The results of this section were obtained as a blind test: that means that the author did not knew if the sample that he was analysing/imaging was coated or uncoated until the analysis was complete. This way it was avoided that the author influences the results.

The analysis of the SLB impact has made with the samples presented in table 4.3. Each of the sample was made in duplicate (a and b).

Table 4.3: Composition of the samples analysed in Nomarski DIC.

Sample	Silica spheres	Liposomes	Buffer Ca^{2+}
1 a&b	1 µL	100 µL	~1.9 mL
2 a&b	1 µL	Uncoated	~2 mL
3 a&b	1 µL	1000 µL	~1 mL
4 a&b	5 µL	100 µL	~1.9 mL
5 a&b	5 µL	Uncoated	~2 mL
6 a&b	5 µL	1000 µL	~1 mL

Two Nomarski DIC images from an uncoated and a coated sample are illustrated in figure 4.14.

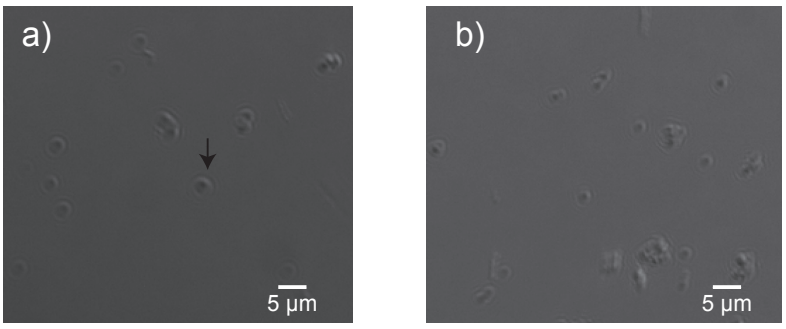

Figure 4.14: Nomarski DIC images of the samples 2b (a)) and 1a (b)).

Figure 4.14 depicts two example of DIC images that were analysed in this work. It is possible to see small isolated spheres which are pertinent to the study presented and some agglomerates which were ignored in the analysis. The small background is due to the small amount of bias induced in the system. It is also highlighted the interferences fringes, that are pointed by the arrow, which are associated to the plane wave illumination used.

Even with multiple cleaning process sometimes the spheres tend to form too much aggregates which makes impossible the analysis of the sample. The samples 3a, 4b and 5b were not analysed due to this reason.

Considering the samples from table 4.3, the results from the analysis of their images (explained in section 3.4) are available in table 4.4.

Table 4.4: Parameters of the Gaussian fits of each sample from table 4.4 measured using Nomarski DIC. All intensity values are normalized relatively to the background Gaussian center. The abbreviations N. Sph., Sha., cen. and Whi. stand for Number of spheres, Shadow, Gaussian center and White.

Sample	N. Sph.	Sha. cen.	Sha. FWHM	Whi. cen	Whi. FWHM	Γ cen.	Γ FWHM
1a	64	0.826	0.125	1.169	0.124	9.88 px	2.24 px
1b	37	0.732	0.185	1.293	0.194	9.62 px	2.82 px
2a	97	0.873	0.147	1.135	0.157	10.40 px	2.33 px
2b	48	0.815	0.198	1.131	0.216	8.91 px	1.48 px
3b	61	0.929	0.159	1.232	0.124	9.11 px	2.26 px
4a	97	0.788	0.313	1.229	0.250	10.10 px	2.36 px
5a	81	0.799	0.170	1.269	0.170	10.80 px	3.82 px
6a	66	0.824	0.216	1.120	0.263	8.79 px	1.92 px
6b	97	0.760	0.134	1.251	0.134	10.02 px	2.70 px

The figure 4.15 shows the dispersion of the fitted parameters considering if the sample in study is coated or uncoated.

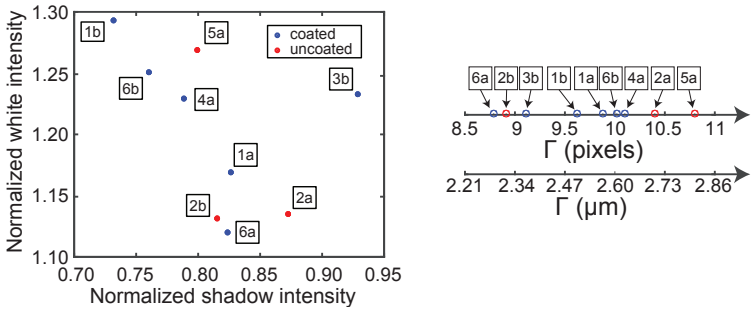

Figure 4.15: Dispersion graphs of the intensities and Γ considering uncoated and coated silica spheres. a) represents the shadows and white normalized intensities and b) represents the Γ.

The analysis of figure 4.15 suggests that the SLB does not has a enough impact to be detectable in DIC. Indeed, the results shows that the experimental oscillations (comparing sample 1a with 1b, 2a with 2b or 6a with 6b) is much bigger than any other difference between the particles.

These experimental oscillations can be justified due to illumination oscillations. Indeed, the DIC background images present a gradient over the images, therefore the localization of the spheres on the images influences the results. Another experimental oscillation is related to the proximity of the spheres to the dish border. Experimentally when the image is taken closer to the border the background intensity increase having an impact on the results.

The radius dispersion of the silica sphere (195±18 nm) is also a justification for the non-uniformity of the results when analysing the similar samples. The relative high pixelization of the image when related with the size of the spheres also has an impact of the results repeatability.

An interesting point to analyse is the viability of fitting the color histogram to a sum

of three Gaussian curves. Generally, the three Gaussian centers are very close to each other which generate a big uncertainty in the fits.

With the separation of the results from table 4.4 considering the coated and the uncoated geometry it is calculated the average values of the Gaussian centers for each geometry. The values are presented in table 4.5.

Table 4.5: Average Gaussian centers Nomarski results considering coated and uncoated spheres.

	Shadow center	White center	Γ center
Uncoated	0.83±0.04	1.18±0.07	2.6±0.3 µm
Coated	0.81±0.07	1.21±0.07	2.5±0.2 µm

The average results shows what was already mentioned before: the SLB impact is much lower that the experimental oscillation which can be seen by the high uncertainty of the results. As a conclusion, experimentally this work has not able to detect the effect of the SLB, therefore its impact in Nomarski DIC image formation is relatively small compared with the experimental oscillations.

De Sérnamont differential interference contrast

The next paragraphs present and discuss the experimental data acquired in De Sérnamont DIC. The De Sérnamont compensator in the back focal plane was adjusted to the value of 5° which was the value with the best contrast.

As for Nomarski DIC, the samples consist in a mix of silica spheres coated and uncoated with a SLB. The characteristics of the multiple samples used are presented in table 4.6.

Table 4.6: Composition of the samples analysed in De Sérnamont DIC.

Sample	Silica spheres	Liposomes	Buffer Ca^{2+}
1 a&b	5 µL	Uncoated	~2 mL
2 a&b	5 µL	Uncoated	~2 mL
3 a&b	5 µL	100 µL	~1.9 mL
4 a&b	5 µL	1000 µL	~1 mL

An example of two De Sérnamont DIC pictures from the coated and uncoated geometry are presented in figure 4.16.

Figure 4.16 depicts two DIC images of a sample without (figure 4.16 a)) and with (figure 4.16 b)) a SLB. Due to the bias used in the experiment the background is much higher that in previous study where it was used Nomarski DIC. The image resolution is also bigger relatively to the Nomarski image which is associated to the utilization of the condenser aperture fully open (with a NA of 0.55). The interferences fringes from figure 4.14 disappear since that the plane wave illumination is not being consider for these images.

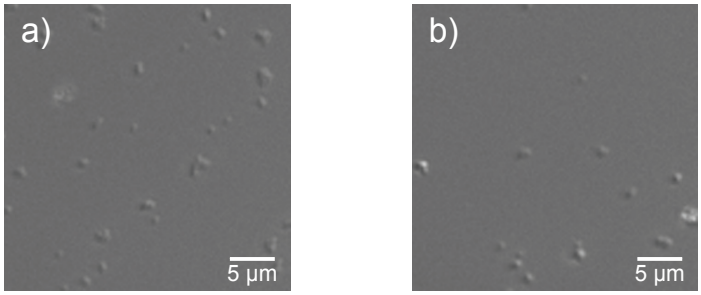

Figure 4.16: De Sérnamont DIC pictures of the sample 1b (a)) and 4a (b)).

Visually, it is not possible to detect any differences between the two images associated to the SLB presence therefore, proceeding with the analysis explained in section 3.4, it is possible to arrive to the quantitative data presented in table 4.6.

Table 4.7: Parameters of the Gaussian fits of each sample from table 4.4 measured using De Sérnamont DIC. All intensity values are normalized relatively to the background Gaussian center. The abbreviations N. Sph., Sha., cen. and Whi. stand for Number of spheres, Shadow, Gaussian center and White.

Sample	N. Sph.	Sha. cen.	Sha. FWHM	Whi. cen	Whi. FWHM
1a	88	0.864	0.149	1.164	0.087
1b	122	0.839	0.109	1.168	0.171
2a	108	0.910	0.066	1.101	0.104
2b	196	0.875	0.192	1.129	0.217
3a	171	0.882	0.135	1.164	0.135
3b	156	0.879	0.081	1.156	0.218
4a	137	0.851	0.155	1.229	0.185
4b	269	0.900	0.127	1.151	0.191

Figure 4.17 represents the dispersion graphs of the Gaussian center of table 4.7 allowing a better visualization of the results.

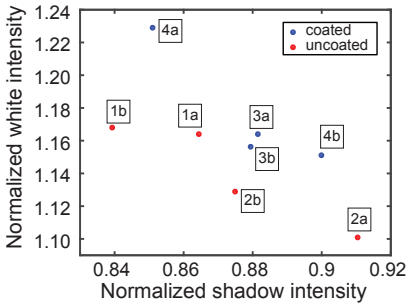

Figure 4.17: Dispersion graphs of the shadow and white intensities considering uncoated and coated silica spheres measured using De Sérnamont DIC.

The conclusions from the graph of figure 4.16 are very similar from the ones taken from the Nomarski study. Indeed, once more, the experimental oscillations is much bigger than the influence of the SLB in the image. The same justifications than before

can be used: not constant background, the radius dispersion of the silica spheres, the pixelization and the fitting protocol.

The average values for the uncoated and coated spheres are represented in table 4.8.

Table 4.8: Average Gaussian centers from De Sérnamont results considering coated and uncoated spheres.

	Shadow center	White center
Uncoated	0.87±0.03	1.14±0.03
Coated	0.89±0.02	1.17±0.04

The average results shows that the experimental oscillations is much bigger that any changes due to the SLB. As a conclusion, to quantify the effect of the SLB it would be required a much precise and accurate experimental protocol.

4.2.2 Imaging of endocytosis model

Multiple studies regarding the endocytosis are presented in this section: as a start it is evaluated the anisotropy impact in the image formation (section 4.2.2.1) and at last it is presented multiple frames of endocytosis using DIC (section 4.2.2.2).

4.2.2.1 Anisotropic impact

The quantification of the anisotropic impact considering the endocytosis geometry is presented in this section. For this purposed it was used the same rational that in section 4.1.4 considering a reference sample with an average RI. The numerical results are presented in figure 4.18.

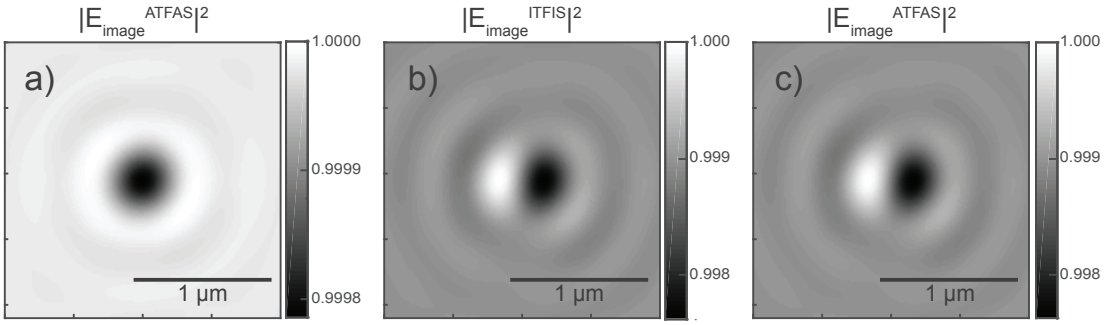

Figure 4.18: Theoretical images considering endocytosis geometry. a) represents a wide field microscopy image considering the anisotropic case; b) and c) are DIC images not considering and considering the anisotropy of the SLB (ITFIS and ATFAS, respectively). Graph a) is normalized relatively to the respective $|\mathbf{E_{image}}^{ATFAS}|^2$ maximum while graphs b) and c) are normalize relatively to $|\mathbf{E_{image}}^{ITFIS}|^2$ b) maximum. The parameter of the geometry modeled are available in table 4.1.

Figure 4.18 a) depicts a wide field image of the endocytosis geometry while the figures 4.18 b) and c) represent a DIC image. Comparing both cases it is possible to highlight

the fact that DIC microscopy has ten times more contrast than the traditional wide field microscopy (comparing the color bars). This is the reason why DIC is highly used in biology where almost transparent sample (as the geometry in study) are commonly analysed. Even using DIC microscopy the contrast of this geometry is very small being hard to observe experimentally.

The difference between the figures 4.18 b) and c) is the anisotropy impact. Therefore, it is possible to see that the respective impact is negligible in the DIC image formation. This can look contrary to the conclusions from section 4.1.4 that the effect in the far-field was important. But, even if the geometry is the same, the analysis is made in two very different systems. In section 4.1.4 it was study the reflection mode which, for this geometry, has Fresnel coefficients very close to zero. Therefore, a minimal change in any of Fresnel coefficients (in terms of absolute value) generates a big shift in the ellipsometry angles. Contrary to what it is being study in this section, where the Fresnel coefficients are very close to the unity then it is needed big alterations of the Fresnel coefficients to generate a significant impact in the far field, and then in the image.

4.2.2.2 Endocytosis dynamics

Multiple simulated DIC images of a liposome approaching a cell is studied in this section to evaluate the changes in the frames due to the distance between the cell and the liposome (δ). Figure 4.19 illustrates the respective frames considering that the focus plane is constantly in the center of the liposome.

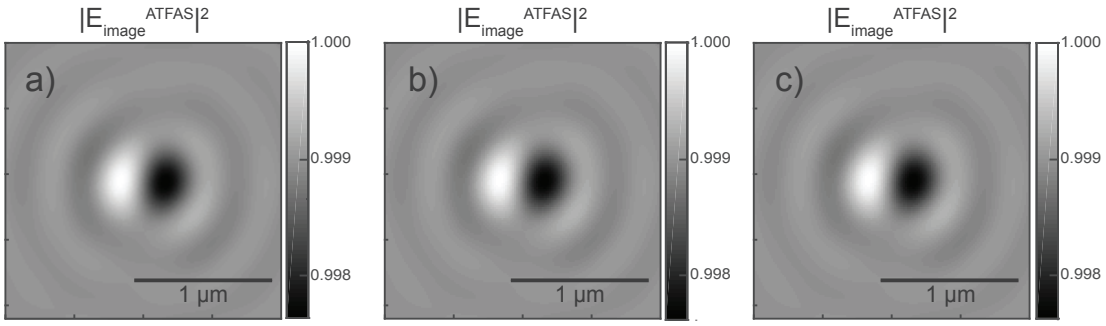

Figure 4.19: Multiple endocytosis DIC images with the approach of the liposome to the cell. For the graphs a), b) and c) the distance δ is respectively 0 nm, 100 nm and 1000 nm. The focus of the image is constantly in the center of the sphere. All graphs are normalized relatively to $|\mathbf{E_{image}}^{ATFAS}|^2$ a) maximum.

As depicted by the multiple frames of the figure 4.19, there is no observable changes in the image due to liposome approach. As explained in section 2.1.4, the solution of the ABV model ($\mathcal{J}^{sphere}$) is a constituted by the scattered light by the particle and the light scattered from the interaction between the scattered light and the substrate. Since that the first component is not depended on the substrate it does not depend on the distance between the substrate and the sphere. Therefore only the second component is depended

on the distance δ and, since that the geometry is almost transparent, this component has not a significant impact in the final solution. Figure 4.20 justified this statement.

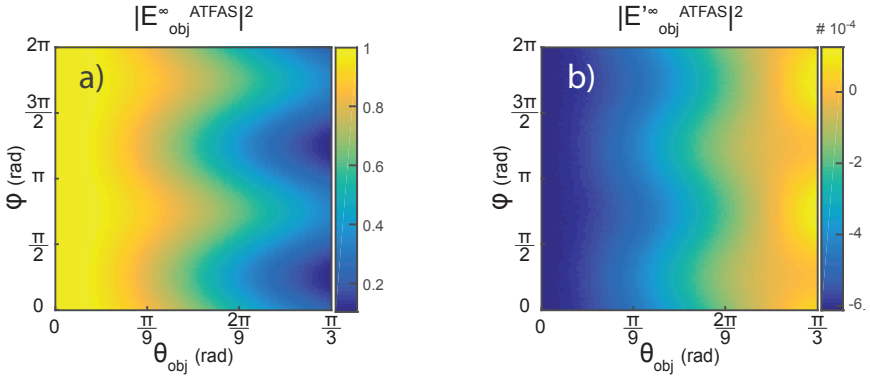

Figure 4.20: Far field considering endocytosis geometry with δ=0 nm. a) represents the total far field considering the endocytosis geometry. b) represents the far field just considering the field originated from the interaction liposome cell. Both graphs are normalized relatively to a) maximum. For display purposes the incident field is not being considered in these graphs.

The far fields illustrated in figures 4.20 a) and b) shows the small impact of the field originated from the interaction liposome cell has. Indeed the field originated from the interaction (figure 4.20 b)) is ten thousands times weaker that the field directly scattered by the liposome (figure 4.20 a)). Therefore the Mie solution (not considering the interaction sphere-substrate) and the ABV solution are practically equal for the geometry in study.

In the previous ellipsometry results section, more precisely in figure 4.6, a sinusoidal shape appears in the ellipsometry angles when the distance δ changes. As mentioned before, this due that in reflection mode the relative phase between the incident field and scattered field changes with the distance δ (factor $e^{iqk'\cos(\theta_i)}$ in equation 2.30, page 15). In the transmission case the relative phase between incident and scattered light is independent of δ thus the sinusoidal shape does not appear. Future work could be to evaluate the same geometry using DIC in reflection mode where it can be possible to see the approach of the liposome due to this sinusoidal shape.

Until this point, the study was made considered that the microscope is focused in the center of the liposome. The next frames correspond to the same geometry ATFAS but considered that the focus is at a fixed distance r_{sphere} from the cell. This is represented by figure 4.21.

The DIC images illustrated in figure 4.21 shows a way of following the approach of a liposome to the cellular membrane. However the theoretical image are just depended of the distance between the plane in focus and the sphere and not to the distance between the cellular membrane and the liposome. That means that, theoretically, the image of a liposome 200 nm above the cellular membrane with the focus at 100 nm is identical to an image of a liposome 500 nm above the cellular membrane with the focus at 400 nm from the cell membrane.

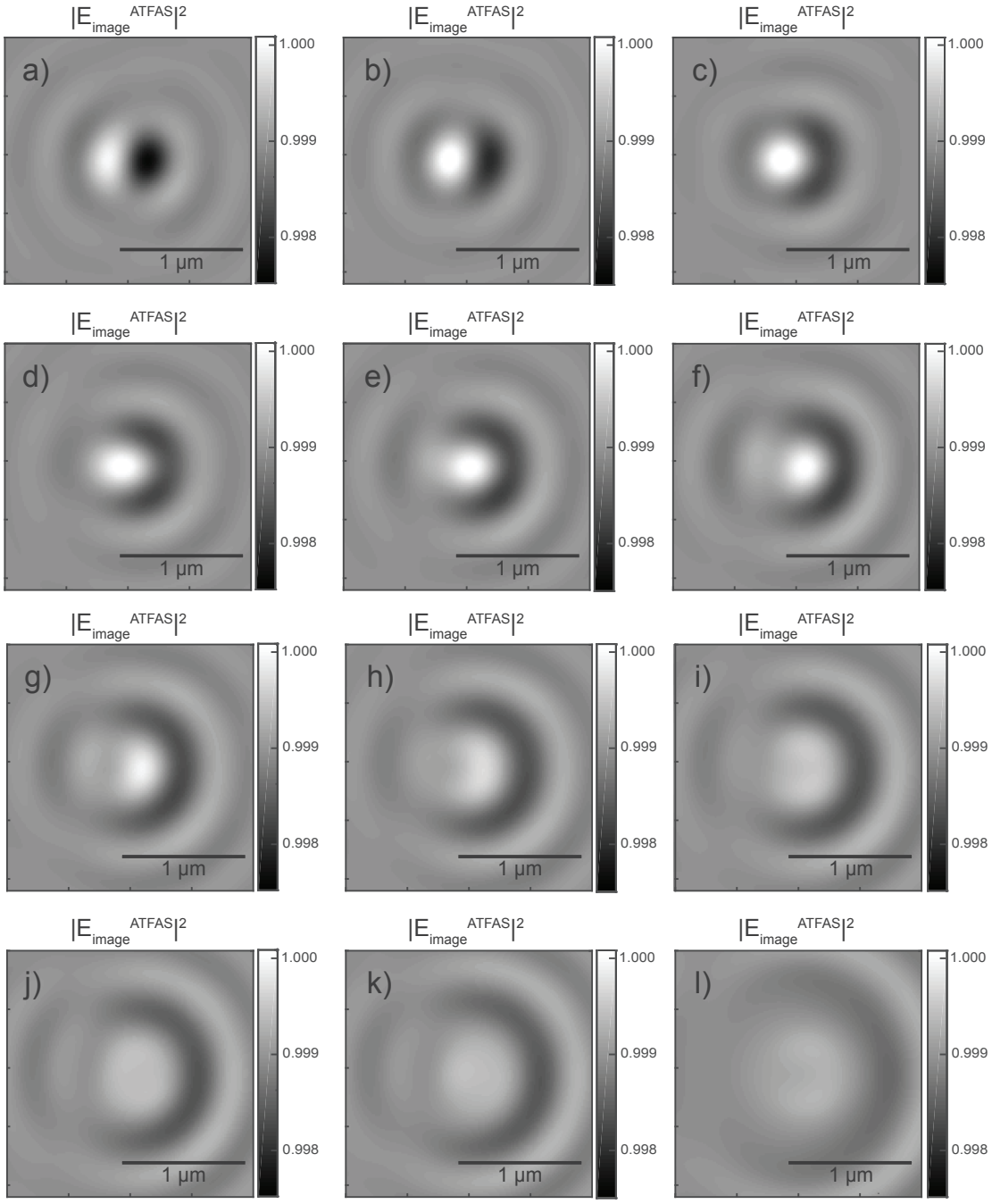

Figure 4.21: Multiple endocytosis DIC images with the approach of the liposome to the cell. For the graphs a), b), c), d), e), f), g), h), i), j), k) and l) the distance δ is respectively 0 nm, 100 nm, 200 nm, 300 nm, 400 nm, 500 nm, 600 nm, 700 nm, 800 nm, 900 nm, 1000 nm and 1500 nm. The focus of the image is constantly at 100 nm from the cellular membrane. The color scale is constant through the frames. All graphs are normalized relatively to a) maximum.

For the reasons explained above it is not possible to monitor the approach of a liposome to a cell using wide field microscopy. The modulation made during this work consist in a rough approximation of endocytosis and future work could be to apply a Finite Difference Time Domain (FDTD) method [67] to modulate the invaginations that occurs in endocytosis. With this approach, it would be possible to study with much more detail the endocytosis approach and even make theoretical validation of the images obtained, for example, on reference [2].

Chapter 5

Conclusions and future perspectives

In this work, it was investigated how small values of optical anisotropy can alter significantly the far field of optical scattering, thereby influencing microscopy image formation. Namely, such optical anisotropy is known to be caused by lipid bilayers forming the boundary of *eukaryotic* cells and vesicles. It was obtained this conclusion through the extension of a scattering model for a sphere near a substrate known as the BV solution to light scattering. In order to understand how this alteration in light scattering is influencing the microscopic image formation it was integrated scattering model developed with an exact model for DIC microscopy, based on the work of Munro and Török [15]. Finally, it was tried to validate theoretical results experimentally by coating silica spheres with a lipid bilayer and observing them through Nomarski and Dé Sernamont DIC microscopy.

Firstly, are presented results of the optical anisotropy impact considering the endocytosis geometry in the electric far field. For quantifications purpose the data was presented in form of the ellipsometry angles Ψ and Δ. This modelling results proves that small amounts of optical anisotropy alter significantly the phase and polarization of the scattered light. Indeed, for the geometry studied, the anisotropy impact must be taken in account to rigorously model this type of data since that the changes can be around $\sim 3°$ in Ψ and Δ.

The main results presented are theoretical and experimental DIC images. Throw theory, it was showed that the presence of a SLB can have a significant impact in DIC images if it is considered the appropriate bias. It was also proved that the changes in the image are due to the increase of the total radius of the particle and the changes of the optical proprieties and not due to the SLB optical anisotropy, which has a negligible impact considering the experimental setups used nowadays. Experimentally, it was tried to detect the presence of the SLB in silica sphere without success. Indeed, the changes that occurs in the measured images are smaller than the experimental oscillations. Many reasons can

be presented to justify the experimental oscillations since the radius dispersion of the silica sphere to the background variations passing by the big pixelization of the images.

A video-DIC of endocytosis is also presented in this dissertation. The results indicate that the main contribution to the observation of endocytosis with DIC originates from the moving into focus of a lipid vesicle and that the contribution due to the interaction vesicle-cell is negligable non-detectable to the image formation process. Regarding how optical anisotropy affects the image formation in the endocytosis geometry the results show that the impact is minimum in the configuration studied. Indeed, consider a SLB as an isotropic material seems a reasonable approximation for this case. As a conclusion regarding the SLB anisotropy impact in DIC, the precision of the experiment made nowadays are insufficient to require the consideration of the SLB as an anisotropic material.

This work answers many question that were still pendent in the optics community and have its continuation was the potential to answer much more. Indeed, with small updates in the DIC model it could be studied the influence of high NA condenser in the anisotropic impact. It would also be possible to study its impact in other microscopies as phase contrast, dark field microscopy, etc... with small changes in the model developed.

Another pertinent study would be to apply the endocytosis geometry to a reflection DIC. In this work it was proved that the phase changes of the reflected light on the top of the particle and at the substrate could induces alterations that could be enough to monitor the liposome approach. However, experimentally the high transmissivity of the geometry would certainly be a problem to provide enough contrast to get an image. The utilization of the FDTD could also be used to modulate the invaginations of the cell membrane but this would origin computational problems due to the Yee cell size required [67].

This work was already presented in three international conferences being the respective information available in appendixes C.1 to C.3 and the ellipsometry results were already submitted in a scientific journal [64] with the respective submitted manuscript in appendix C.4. Another manuscript to a peer review journal about the impact of the SLB in DIC microscopy is in preparation [65].

Bibliography

[1] A. Sharma and U. S. Sharma. "Liposomes in drug delivery: Progress and limitations." *International Journal of Pharmaceutics* 154.2 (August 1997), pp. 123–140.

[2] J. H. Hines, S. Henle, L. P. Carlstrom, M. Abu-Rub, and J. Henley. "Single vesicle imaging indicates distinct modes of rapid membrane retrieval during nerve growth." *BMC biology* 10.1 (2012), p. 4.

[3] Nikon Instruments Inc. *Introduction to Fluorescence Microscopy | MicroscopyU*. URL: https://www.microscopyu.com/techniques/fluorescence/introduction-to-fluorescence-microscopy (visited on 09/21/2017).

[4] F. H. Smith. *Interference microscope*. 1952.

[5] G. Nomarski and A. R. Weill. "Application à la métallographie des méthodes interférentielles à deux ondes polarisées." *Rev. Metall* 2 (1955), pp. 121–128.

[6] D. J. Goldberg and D. W. Burmeister. "Stages in axon formation: Observations of growth of Aplysia axons in culture using video-enhanced contrast-differential interference contrast microscopy." *Journal of Cell Biology* 103.5 (1986), pp. 1921–1931.

[7] J. M. Aletta and L. a. Greene. "Growth cone configuration and advance: a time-lapse study using video-enhanced differential interference contrast microscopy." *The Journal of neuroscience : the official journal of the Society for Neuroscience* 8.4 (1988), pp. 1425–1435.

[8] R. D. Allen, N. S. Allen, and J. L. Travis. "Video-enhanced contrast, differential interference contrast (AVEC-DIC) microscopy: A new method capable of analyzing microtubule-related motility in the reticulopodial network of allogromia laticollaris." *Cytoskeleton* 1.3 (1981), pp. 291–302.

[9] A. Miranda and P. A. A. De Beule. "Microscopic thin film optical anisotropy imaging at the solid-liquid interface." *Review of Scientific Instruments* 87.4 (2016).

[10] S. Chowdhury, W. J. Eldridge, A. Wax, and J. Izatt. "Refractive index tomography with structured illumination." *Optica* 4.5 (2017), pp. 537–545.

[11] E. Wolf. "Three-dimensional structure determination of semi-transparent objects from holographic data." *Optics Communications* 1.4 (1969), pp. 153–156.

[12] A. Anantharam, B. Onoa, R. H. Edwards, R. W. Holz, and D. Axelrod. "Localized topological changes of the plasma membrane upon exocytosis visualized by polarized TIRFM." *Journal of Cell Biology* 188.3 (2010), pp. 415–428.

[13] C. J. R. Sheppard and T. Wilson. "Fourier imaging of phase information in scanning and conventional optical microscopes." *Philosophical Transactions of the Royal Society of London A: Mathematical, Physical and Engineering Sciences* 295.1415 (1980), pp. 513–536.

[14] C. J. Cogswell and C. J. R. Sheppard. "Confocal differential interference contrast (DIC) microscopy: including a theoretical analysis of conventional and confocal DIC imaging." *Journal of Microscopy* 165.1 (1992), pp. 81–101.

[15] P. R. Munro and P. Török. "Vectorial, high numerical aperture study of Nomarski's differential interference contrast microscope." *Optics Express* 13.18 (2005), p. 6833.

[16] E. Wolf and B. Richards. "Electromagnetic diffraction in optical systems." *Royal Society of London* (1959), pp. 349–357.

[17] E. Wolf. "Electromagnetic Diffraction in Optical Systems. I. An Integral Representation of the Image Field." *Proceedings of the Royal Society A: Mathematical, Physical and Engineering Sciences* 253.1274 (1959), pp. 349–357.

[18] P. A. Bobbert, J. Vlieger, and R. Greef. "Theory of light reflection from a substrate sparsely seeded with spheres: Comparison with an ellipsometric experiment." *Thin Solid Films* 164.C (July 1988), pp. 63–67.

[19] P. A. Bobbert and J. Vlieger. "Light scattering by a sphere on a substrate." *Physica A: Statistical Mechanics and its Applications* 137.1-2 (July 1986), pp. 209–242.

[20] P. A. A. De Beule. "Surface scattering of core–shell particles with anisotropic shell." *Journal of the Optical Society of America A* 31.1 (2014), p. 162.

[21] D. Viegas, E. Fernandes, R. Queirós, D. Y. Petrovykh, and P. De Beule. "Adapting Bobbert-Vlieger model to spectroscopic ellipsometry of gold nanoparticles with bio-organic shells." *Biomedical Optics Express* 8.8 (2017), pp. 3538–3550.

[22] P. Török, P. Varga, Z. Laczik, and G. R. Booker. "Electromagnetic diffraction of light focused through a planar interface between materials of mismatched refractive indices: an integral representation." *JOSA A* 12.2 (1995), pp. 325–332.

[23] H. Fujiwara. *Spectroscopic Ellipsometry Principles and Applications*. Vol. 158. 6. 1997.

[24] F. L. McCrackin, E. Passaglia, R. R. Stromberg, and H. L. Steinberg. "Measurement of the thickness and refractive index of very thin films and the optical properties of surfaces by ellipsometry." *J. Res. Nat. Bur. Sec. A* 67 (1963).

[25] M. R. Baklanov, K. P. Mogilnikov, V. G. Polovinkin, and F. N. Dultsev. "Determination of pore size distribution in thin films by ellipsometric porosimetry." *Journal of Vacuum Science & Technology B: Microelectronics and Nanometer Structures Processing, Measurement, and Phenomena* 18.3 (2000), pp. 1385–1391.

[26] R. M. A. Azzam and N. M. Bashara. *Ellipsometry and polarized light*. North-Holland. sole distributors for the USA and Canada, Elsevier Science Publishing Co., Inc., 1987.

[27] Z. Salamon and G. Tollin. "Optical anisotropy in lipid bilayer membranes: coupled plasmon-waveguide resonance measurements of molecular orientation, polarizability, and shape." *Biophysical journal* 80.3 (2001), pp. 1557–1567.

[28] R. Horvath and J. J. Ramsden. "Quasi-isotropic analysis of anisotropic thin films on optical waveguides." *Langmuir* 23.18 (August 2007), pp. 9330–9334.

[29] M. Born and E. Wolf. *Principles of optics: Electromagnetic Theory of Propagation, Interference and Diffraction of Light*. Elsevier, 1999, pp. 1–952.

[30] D. J. De Smet. "Ellipsometry of anisotropic thin films." *Journal of the Optical Society of America* 64.5 (1974), p. 631.

[31] G. Mie. "Beiträge zur Optik trüber Medien, speziell kolloidaler Metallösungen." *Annalen der physik* 330.3 (1908), pp. 377–445.

[32] C. F. Bohren and D. R. Huffman. *Absorption and scattering of light by small particles*. John Wiley & Sons, 2008.

[33] P. Török, T. Wilson, P. D. Higdon, and R. Juskaitis. "Optimising the image contrast of conventional and confocal optical microscopes imaging finite sized spherical gold scatterers." October (1998), pp. 335–341.

[34] B. Lange and S. R. Aragón. "Mie scattering from thin anisotropic spherical shells." *The Journal of Chemical Physics* 92.8 (1990), pp. 4643–4650.

[35] O. Haeberlé, M. Ammar, H. Furukawa, K. Tenjimbayashi, and P. Török. "Point spread function of optical microscopes imaging through stratified media." *Optics Express* 11.22 (2003), pp. 2964–2969.

[36] Sketchfab. *Animal Cell by 16-404 - download 3D scene*. URL: https://sketchfab.com/models/015fad6b2ef845b0911b7681d2006412 (visited on 09/07/2017).

[37] L. Novotny. *Principles of Nano-Optics*. Vol. 1. 4. 2006.

[38] M. R. Foreman and P. Török. "Computational methods in vectorial imaging." *Journal of Modern Optics* 58.5-6 (2011), pp. 339–364.

[39] J. W. Goodman. *Introduction to Fourier optics*. Roberts and Company Publishers, 2005.

[40] L. M. E. Wolf. *Optical Coherence and Quantum Optics*. Cambridge university press, 1995.

[41] M. W. Davidson and M. Abramowitz. "Optical microscopy." *Encyclopedia of imaging science and technology* (2002).

[42] P. B. Johnson and R. W. Christy. "Optical Constants of the Noble Metals." *Physical Review B* 6.12 (December 1972), pp. 4370–4379.

[43] D. J. Innes and A. L. Bloom. "Design of optical systems for use with laser beams." *Spectra-Physics Laser Technical Bulletin* 5 (1966), pp. 1–10.

[44] S. B. Mehta and C. J. R. Sheppard. "Partially coherent image formation in differential interference contrast (DIC) microscope." 16.24 (2008), pp. 2185–2199.

[45] D. L. Lessor, J. S. Hartman, and R. L. Gordon. "Quantitative surface topography determination by Nomarski reflection microscopy. I. Theory." *J. Opt. Soc. Am.* 69.2 (1979), pp. 357–366.

[46] The MathWorks Inc. *Vectorization - MATLAB & Simulink*. URL: https://www.mathworks.com/help/matlab/matlab%7B%5C_%7Dprog/vectorization.html (visited on 08/10/2017).

[47] T. A. Germer. *NIST SCATMECH: Polarized light scattering C++ class library*.

[48] J. H. Kim, S. H. Ehrman, G. W. Mulholland, and T. A. Germer. "Polarized light scattering by dielectric and metallic spheres on silicon wafers." *Applied optics* 41.25 (2002), pp. 5405–5412.

[49] T. A. Germer. "Simulations of optical microscope images." *Proceedings of SPIE* 6152 (2006), pages.

[50] K. von Laven. *Grid Sphere - File Exchange - MATLAB Central*. URL: https://www.mathworks.com/matlabcentral/fileexchange/28842-grid-sphere (visited on 08/12/2017).

[51] N. Teanby. "An icosahedron-based method for even binning of globally distributed remote sensing data." *Computers & Geosciences* 32.9 (November 2006), pp. 1442–1450.

[52] I. H. Malitson. "Interspecimen Comparison of the Refractive Index of Fused Silica." *Journal of the Optical Society of America* 55.10 (October 1965), p. 1205.

[53] K. Nozawa, H. Gailhanou, L. Raison, P. Panizza, H. Ushiki, E. Sellier, J. P. Delville, and M. H. Delville. "Smart Control of Monodisperse Stöber Silica Particles: Effect of Reactant Addition Rate on Growth Process." *Langmuir* 21.4 (February 2005), pp. 1516–1523.

[54] R. Veneziano, G. Derrien, S. Tan, A. Brisson, J.-M. Devoisselle, J. Chopineau, and C. Charnay. "One Step Synthesis of Gold-Loaded Radial Mesoporous Silica Nanospheres and Supported Lipid Bilayer Functionalization: Towards Bio-Multifunctional Sensors." *Small* 8.23 (2012), pp. 3674–3682.

[55] F. Sigworth. *Read .dm3 and .dm4 image files - File Exchange - MATLAB Central*. URL: https://www.mathworks.com/matlabcentral/fileexchange/43005-read-dm3-and-dm4-image-files (visited on 08/12/2017).

[56] X.-C. Bai, I. S. Fernandez, G. McMullan, and S. H. W. Scheres. "Ribosome structures to near-atomic resolution from thirty thousand cryo-EM particles." *eLife* 2 (February 2013), e00461.

[57] D. Lyumkis, J.-P. Julien, N. de Val, A. Cupo, C. S. Potter, P.-J. Klasse, D. R. Burton, R. W. Sanders, J. P. Moore, B. Carragher, I. A. Wilson, and A. B. Ward. "Cryo-EM Structure of a Fully Glycosylated Soluble Cleaved HIV-1 Envelope Trimer." *Science* 342.6165 (2013).

[58] S. Mornet, O. Lambert, E. Duguet, and A. Brisson. "The Formation of Supported Lipid Bilayers on Silica Nanoparticles Revealed by Cryoelectron Microscopy." *Nano Letters* 5.2 (February 2005), pp. 281–285.

[59] R. J. Hunter. *Zeta potential in colloid science : principles and applications*.

[60] Nikon Instruments Inc. *de Sénarmont Bias Retardation in DIC Microscopy | MicroscopyU*. URL: https://www.microscopyu.com/techniques/dic/de-s%C3%A9narmont-bias-retardation-in-dic-microscopy (visited on 09/07/2017).

[61] R. D. Allen, N. S. Alien, and J. L. Travis. "Video Enhanced Contrast, Differential Interference Contrast (AVEC-DIC) Microscopy: A New Method Capable of Analyzing MicrotubuIe-Related Motility in the Reticulopodial Network of Allogromia laticollaris." 302 (1981), pp. 291–302.

[62] B. J. Schnapp. "Viewing single microtubules by video light microscopy." *Methods in enzymology* 134 (1986), pp. 561–573.

[63] C. Y. Yeh. *Zeiss Laser Scanning Confocal Microscope LSM file reader - File Exchange - MATLAB Central*. URL: https://www.mathworks.com/matlabcentral/fileexchange/46892-zeiss-laser-scanning-confocal-microscope-lsm-file-reader (visited on 08/14/2017).

[64] D. Marques, A. Miranda, A. G. Silva, P. R. T. Munro, and P. A. A. De Beule. "On the influence of lipid-induced optical anisotropy for the bioimaging of exo-or endocytosis with interference microscopic imaging (Submitted)." *Journal of microscopy* (2017).

[65] D. Marques, A. Miranda, A. G. Silva, P. R. T. Munro, and P. A. A. De Beule. "In preparation" (2017).

[66] E. D. Salmon and P. Tran. "High-resolution video-enhanced differential interference contrast (VE-DIC) light microscopy." *Methods in cell biology* 56 (1998), pp. 153–184.

[67] A. Taflove and S. C. Hagness. *Computational electrodynamics: the finite-difference time-domain method*. Artech house, 2005.

[68] D. Marques, A. Miranda, A. G. Silva, P. R. T. Munro, and P. A. A. De Beule. *Optical scattering and microscopic imaging of cellular exo- and endocytosis*. URL: http://programme.exordo.com/nanop2017/delegates/presentation/9/ (visited on 09/19/2017).

APPENDIX A

CONVENTIONS, NOMENCLATURE AND COORDINATE SYSTEMS

This chapter introduces the reader to the coordinate systems, nomenclature and conventions used in this dissertation.

A.1 Spherical coordinates

The spherical coordinates are considered as (r, θ, ϕ) - figure A.1.

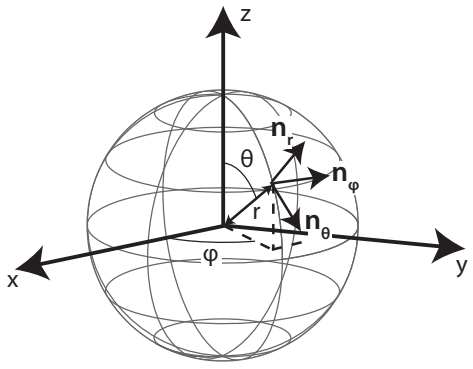

Figure A.1: Representation of the spherical coordinate system used in this dissertation.

The respective unitary vectors are defined by the equations A.1 to A.3.

$$\mathbf{n_r} = \sin\theta\cos\phi\ \mathbf{n_x} + \sin\theta\sin\phi\ \mathbf{n_y} + \cos\theta\mathbf{n_z} \tag{A.1}$$

$$\mathbf{n}_\theta = \cos\theta\cos\phi\ \mathbf{n_x} + \cos\theta\sin\phi\ \mathbf{n_y} - \sin\theta\mathbf{n_z} \tag{A.2}$$

$$\mathbf{n}_\phi = -\sin\phi\mathbf{n_x} + \cos\phi\mathbf{n_y} \tag{A.3}$$

A.2 Cylindrical coordinates

The cylindrical coordinates are considered as (ρ, ϕ, z) - figure A.2.

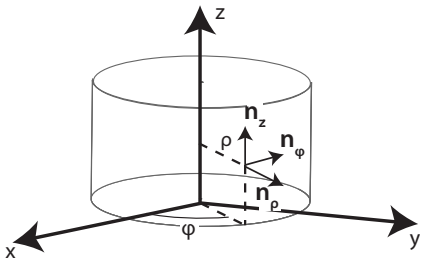

Figure A.2: Representation of the cylindrical coordinate system used in this dissertation.

And the unitary vectors are represented in equations A.4 to A.6.

$$\mathbf{n}_\rho = \cos\phi\ \mathbf{n_x} + \sin\phi\ \mathbf{n_y} \tag{A.4}$$

$$\mathbf{n}_\phi = -\sin\phi \mathbf{n_x} + \cos\phi \mathbf{n_y} \tag{A.5}$$

$$\mathbf{n_z} = \mathbf{n_z} \tag{A.6}$$

A.3 Light conventions

Throw this manuscript the light was considered using the physics convention. More information regarding the differences between the physics and optics conventions is available in appendix 2 of reference [23].

The Jones vectors are represented using the right-handed basis set (s, p, k) where s is the component perpendicular to the POI, p is the component parallel to the POI and k is the direction of propagation which is perpendicular to the previous.

A.4 Nomenclature

The following nomenclature is used in this manuscript:

- N represents the RI with the imaginary component (which can be null);
- n represents a RI where the imaginary component is null;
- **a** represents the vector a;
- $\mathscr{A}$ represents the matrix a;
- $\mathbf{n_a}$ represents the versor of the component a;
- $\mathbf{a}^\infty$ represents an electric a which is in the far field condition;
- $\hat{\mathbf{a}}$ represents the angular spectrum of a;

Appendix B

Image analysis

B.1 Transmission electron microscopy analysis

In this appendix, it is presented the Matlab script developed during this work to calculate the radius of the spheres present in TEM images (listing B.1). For this work it was applied to calculate the radius of the silica spheres and the respective uncertainty.

Listing B.1: Matlab script developed to calculate the radius dispersion from the TEM images.

```
%>%>%%%
```

```
%>%>%%%
```

```
6
7   input = squeeze(input);
8
9   %Creation of the gradient image using prewitt method
10  grad = imgradient(input,'prewitt');
11
12  %Creation of the Gaussian filter specifications
13  filter = fspecial('gauss', [5, 5], 2);
14  %Application of the Gaussian filter to the gradient image
15  filteredImage = imfilter(uint8(grad),filter);
16
17  %Application of the threshold to create the mask
18  mask = filteredImage > threshold;
19
20  %Application of the mask calculated before on the original image
21  output = uint8(uint8(mask) .* uint8(input));
22 end
```

Appendix C

Conferences and scientific article

C.1 NANOP 2017

The work was also presented in an oral presentation by Dr. Pieter A. A. De Beule at Nanophotonics and Micro/Nano Optics (NANOP) International Conference 2017 that happened from 13 to 15 September in Barcelona, Spain. The respective abstract and presentation are available at reference [68].

C.2 XIX. Annual Linz Winter Workshop

Preliminary results of this dissertation were present by the author in the XIX Annual Linz Winter Workshop "Advances in Single-Molecule Research & Nanoscience" from 3 to 6 February 2017 at Linz, Austria in a poster communication. The poster is available in the next page.

Optical scattering of cellular exo- and endocytosis

Dylan Marques[a], Adelaide Miranda[b], Ana G. Silva[a], Pieter A. A. De Beule[b]

[a] Departamento de Física, Faculdade de Ciências e Tecnologia, Universidade Nova de Lisboa, Campus de Caparica, Caparica, 2829-516, Portugal
[b] Applied Nano-Optics Laboratory, International Iberian Nanotechnology Laboratory, Braga 4715-330, Portugal (pieter.de-beule@inl.int)

Motivation

Nowadays, to study cellular biological process as endocytosis are used techniques that require external fluorescent agents. *In-vivo* detection of exo- and endocytosis represent a great challenge to image capture technology due to the speed of the event, the size of the lipid vesicles and optical contrast available.

Differential Interference Contrast (DIC) microscopy has the advantage that allows label-free imaging. However, in order to understand the DIC microscopic image formation process it is necessary to investigate how much and in which way optically anisotropic structures scatters the light.

Previous work has been done by P. A. A. De Beule quantifying the anisotropic effect of a vesicle coated with a SLB above an isotropic substrate [1].

Theory

In 1986, Bobbert et *al.* solved the Maxwell's equations for a substrate seeded with spheres that is known as Bobbert-Vlieger model [2] and it is represented in the figure 1.

The reflectivities of these systems can be calculated by the equation 1 for p and s waves.

$$R_{p,sTot} = r_{p,sSub}(\theta_0)e^{2iq\cos(\theta_0)} + \frac{2\pi iN}{k\cos(\theta_0)} r_{p,sPar}(r_{p,sSub}) \quad (1)$$

Where $r_{p,sSub}$ is the reflectivity from a substrate with an anisotropic thin film and $r_{p,sPar}$ is the reflectivity from the particle which depends of the substrate reflectivity [3].

Endocytosis, a process in which a cell membrane fuses with vesicles by engulfing them, can be conceptualized as a core-shell particle approaching a substrate (intracellular medium, essentially water).

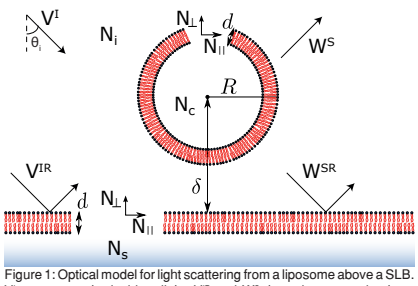

Figure 1: Optical model for light scattering from a liposome above a SLB. V^I represents the incident light, V^{IR} and W^S the substrate and sphere reflection, respectively and W^{SR} the reflection of W^S by the substrate.

Results

As a reference, all components of the model are considered isotropic with the refractive index given by equation 2.

$$N_{avg}^2 = \frac{2N_{\parallel}^2}{3} + \frac{N_{\perp}^2}{3} \quad (2)$$

The anisotropic effect is defined by $\delta\psi = \psi - \psi_{avg}$ and $\delta\Delta = \Delta - \Delta_{avg}$, D_ψ and D_Δ are defined by equation 3.

$$D_{\psi,\Delta} = \sum_{\theta_0=\theta_i}^{\theta f} |\psi,\Delta_{Ani} - \psi,\Delta_{avg}| \quad (3)$$

One of the goals of this work is to demonstrate that it is possible to monitor the approaching of vesicles to a cellular membrane using ellipsometry. To confirm this, simulations which are represented in the figure 2, have been made changing the distance between the cellular membrane (substrate) and the vesicles (spheres).

Analising the data, it is possible to notice the periodicity of the results, which is due to the constructive and destructive interference of the light reflected at the substrate and at the top of the spheres.

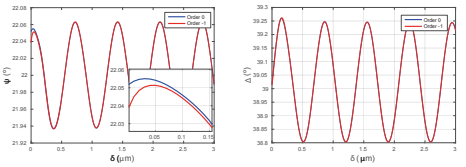

Figure 2: Δ and ψ as a function of the distance between liposomes and the SLB (considering a spheres density of 1 μm^{-2}).

Incident medium and substrate

Simulations have been done to check the impact of the substrate (N_s) and incident medium (N_i) on the anisotropy effect.

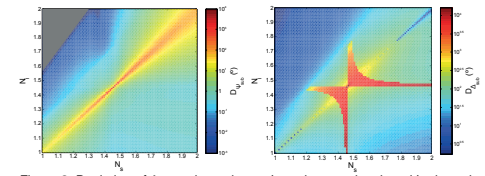

Figure 3: Deviation of Δ_{sub} and ψ_{sub} due at the anisotropy in a logarithmic scale of a SLB above a substrate (N_s) in an incident medium (N_i).

The images above show that values in the condition N_s=N_i have bigger shift between the anisotropic and the isotropic and the maximum is in the point $N_s = N_i \simeq N_{avg}$.

ψ and Δ as function of λ

In figure 4, it is quantified the anisotropic effect in a ellipsometry experiment changing the wavelength.

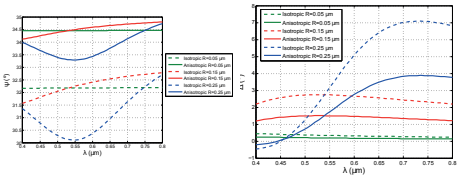

Figure 4: Difference in Δ and ψ due the SLB anisotropy in function of the λ.

For the results above, it is possible to conclude that, for this experiment, the anisotropic effect induced an offset in y axis (ψ or Δ).

ψ and Δ as function of AOI (θ_0)

Simulations to quantify the anisotropy on a ellipsometry experiment as function of the Angle Of Incidence (AOI) are presented in figure 5.

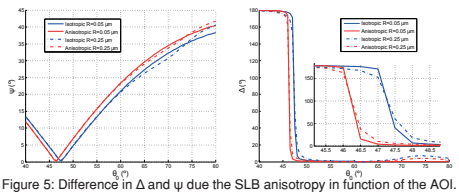

Figure 5: Difference in Δ and ψ due the SLB anisotropy in function of the AOI.

For these ellipsometry measurements, the anisotropy effect can be observed by an offset in the AOI and changed with the particle radius.

Conclusions

Through application of an extension to the Bobbert-Vlieger solution of particle scattering near a substrate, we have proven that the induced optical anisotropy by small density of lipids (1 μm^{-2}) alter the far-field optical scattering properties for a liposome above a lipid bilayer, representative for cellular and endocytosis. One can therefore expect lipid optical anisotropy to be and important contributing factor to image formation in DIC microscopy.

Further work

Many models for DIC microscopy rely on isotropic samples, albeit a full vectorial model adequate for high Numerical Aperture (NA) objective formation has been developed taking in account the full vectorial nature of the electromagnetic field near imaging focus [4].

Future work will therefore focus on the prediction of DIC image formation of anisotropic samples.

References

[1] P. A. A. De Beule, Surface scattering of coreshell particles with anisotropic shell, Journal of the Optical Society of America A 31 (1) (2014) 162.
[2] P. Bobbert, J. Vlieger, R. Greef, Light reflection from a substrate sparsely seeded with spheres - comparison with an ellipsometric experiment, Physica A: Statistical Mechanics and its Applications 137 (1-2) (1986) 243-257.
[3] P. A. Bobbert, J. Vlieger, Light scattering by a sphere on a substrate, Physica A: Statistical Mechanics and its Applications 137 (1-2) (1986) 209-242.
[4] Munro, Peter RT, and Peter Török. "Vectorial, high numerical aperture study of Nomarski's differential interference contrast microscope." Optics express 13.18 (2005): 6833-6847.

Acknowledgment

The author acknowledges International Iberian Nanotechnology Laboratory (INL) for the financial support and the possibility to carry out the work at INL facilities.

FACULDADE DE CIÊNCIAS E TECNOLOGIA
UNIVERSIDADE NOVA DE LISBOA

INTERNATIONAL IBERIAN NANOTECHNOLOGY LABORATORY

C.3 19^{th} IUPAB congress and 11^{th} EBSA congress

The author also presented some results in a poster format in the 19^{th} International Union of Pure and Applied Biophysics (IUPAB) congress and 11^{th} European Biophysical Societies Association (EBSA) congress which happened from 19 to 21 July 2017 in Edinburgh, Scotland. The poster is available in the next page.

Optical scattering and microscopic imaging of cellular exo- and endocytosis

Dylan Marques[a, b], Adelaide Miranda[b], Ana G. Silva[a], Peter Munro[c], Pieter A. A. De Beule*[b]

[a] Departamento de Física, Faculdade de Ciências e Tecnologia, Universidade Nova de Lisboa, Campus de Caparica, Caparica, 2829-516, Portugal
[b] Applied Nano-Optics Laboratory, International Iberian Nanotechnology Laboratory, Braga 4715-330, Portugal
[c] Department of Medical Physics and Biomedical Engineering, University College London, Malet Place, Gower Street, London, WC1E 6BT, United Kingdom
* Corresponding author: pieter.de-beule@inl.int

Motivation

The study of cellular biological process such as endocytosis employs techniques that require exogenous fluorescent labels. In-vivo detection of exo- and endocytosis is very challenging for current imaging technology due to the speed of the event, the small size of the lipid vesicles and th optical contrast available.

Differential Interference Contrast (DIC) microscopy has the advantage of allowing label-free imaging. However, in order to understand DIC microscopic image formation, it is necessary to investigate the way in which optically anisotropic structures scatters the light.

Most current optical models consider only isotropic samples. Based on a vectorial model [1], in this work it is calculated the influence that weakly anisotropic scatterers (such as a lipid bilayer) have on DIC image formation. We also compare the simulated results with experiment.

Endocytosis

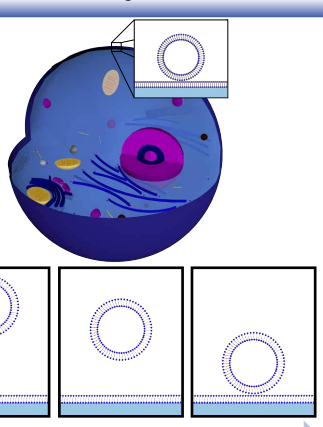

Time

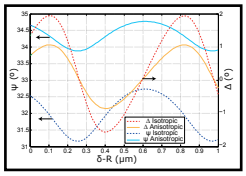

Conclusion

Through experimental and theoretical results, we quantified the impact that small amounts of anisotropy (Δn=0.01) has in DIC's image formation. In particular, for the system studied the lipid's anisotropy does not have a big impact in the image.

It was also proven the impact that considering anisotropy in the far field of endocytosis has. Further work will consist in incorporate endocytosis in a DIC's model to quantify the anisotropy effect in the respective image formation.

References

[1] Peter RT Munro and Peter Török. "Vectorial, high numerical aperture study of Nomarski's differential interference contrast microscope." Optics Express 13.18 (2005): 6833-6847, 2005.
[2] Veneziano, Remi, et al. "One Step Synthesis of Gold Loaded Radial Mesoporous Silica Nanospheres and Supported Lipid Bilayer Functionalization: Towards Bio Multifunctional Sensors." Small 8.23 (2012): 3674-3682.
[3] Nozawa, Koh, et al. "Smart control of monodisperse Stöber silica particles: effect of reactant addition rate on growth process." Langmuir 21.4 (2005): 1516-1523.

Acknowledgment

The author acknowledges International Iberian Nanotechnology Laboratory (INL) for the financial support and the possibility to carry out the work at INL facilities.

De Sérnamont DIC

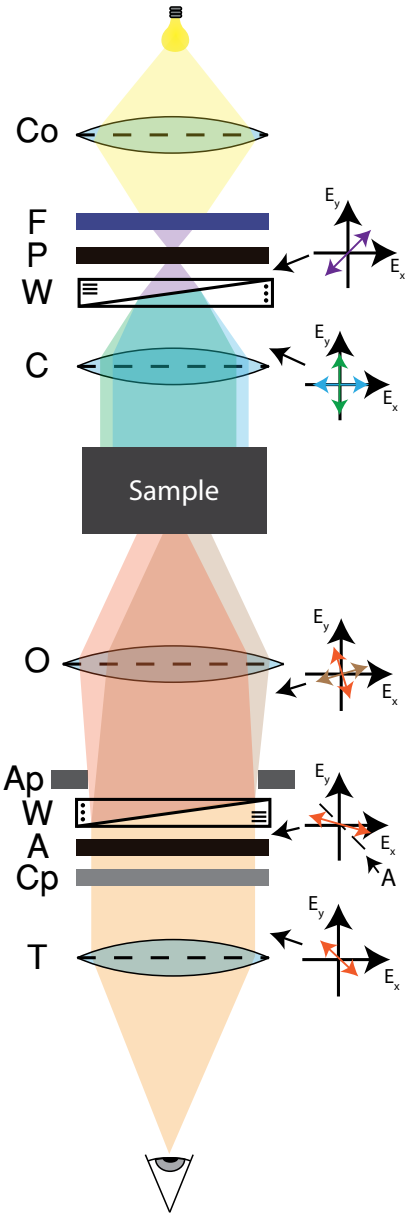

Co - Collector lens;
F - Monochromatic filter;
P - Polarizer; **W** - Wollaston prism;
C - Condenser; **O** - Objective;
Ap - Aperture; **A** - Analyzer;
Cp - De Sénarmont Compensator;
T - Tube lens;

Anisotropy effect

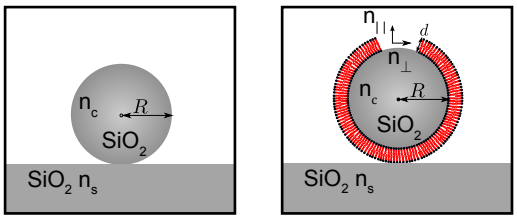

Sample preparation/validation [2,3]

Zeta potential	Zeta potential
(-54 ± 1) mV	(-11 ± 2) mV

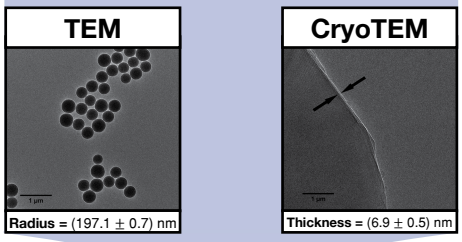

Results

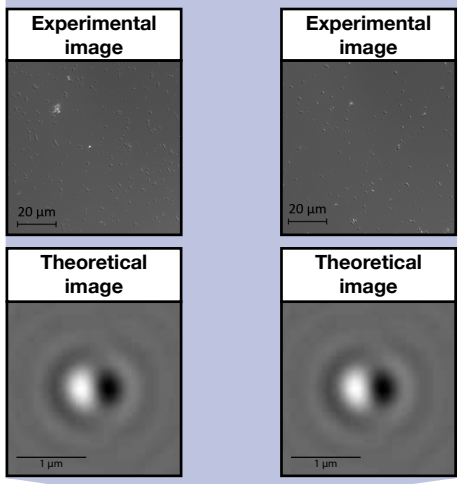

Image treatment

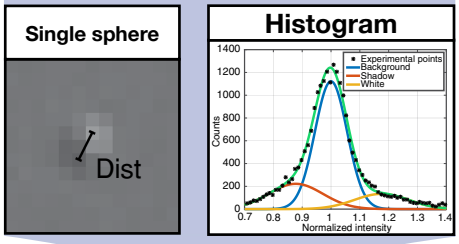

	With lipids		Without lipids	
	Experimental	Theoretical	Experimental	Theoretical
White	1.17 ± 0.03	1.1010	1.15 ± 0.01	1.0980
Shadow	0.88 ± 0.01	0.9011	0.85 ± 0.01	0.9015
Dist	(2.31 ± 0.05) μm	0.375 μm	(1.92 ± 0.03) μm	0.375 μm

FACULDADE DE CIÊNCIAS E TECNOLOGIA UNIVERSIDADE NOVA DE LISBOA

INTERNATIONAL IBERIAN NANOTECHNOLOGY LABORATORY

UCL

C.4 Scientific article

The scientific article submitted to Journal of microscopy with the ellipsometry results of this work is available in the next pages [64].

ORIGINAL ARTICLE

Journal Section

On the influence of lipid-induced optical anisotropy for the bioimaging of exo -or endocytosis with interference microscopic imaging

Dylan Marques[1,2] | Adelaide Miranda PhD[2] | Ana G. Silva Prof[1] | Peter R. T. Munro PhD[3] | Pieter A. A. De Beule PhD[2]

[1]Departamento de Física, Faculdade de Ciências e Tecnologia, Universidade Nova de Lisboa, Campus de Caparica, Caparica, P-2829-516, Portugal

[2]Applied Nano-Optics Group, Department of Life Sciences, International Iberian Nanotechnology Laboratory, Braga 4715-330, Portugal

[3]Department of Medical Physics and Biomedical Engineering, University College London, Malet Place, Gower Street, London, WC1E 6BT, United Kingdom

Correspondence
Pieter De Beule PhD, Applied Nano-Optics Group, Department of Life Sciences, International Iberian Nanotechnology Laboratory, Braga, 4715-330, Portugal
Email: pieter.de-beule@inl.int

Funding information
Norte2020, Norte's Regional Operational Programme 2014-2020, Grant Number: NORTE-01-0145-FEDER-000019

Some implementations of interference microscopy imaging use digital holographic measurements of complex scattered fields to reconstruct three-dimensional refractive index maps of weakly scattering, semi-transparent objects, frequently encountered in biological investigations. Reconstruction occurs through application of the object scattering potential which assumes an isotropic refractive index throughout the object. Here, we demonstrate that this assumption can in some circumstances be invalid for biological imaging due to the presence of lipid-induced optical anisotropy. We show that the nanoscale organization of lipids in the observation of cellular endocytosis with polarized light induces a significant change in far field scattering. We obtain this result by presenting a general solution to Maxwell's equations describing light scattering of core-shell particles near an isotropic substrate covered with an anisotropic thin film. This solution is based on an extension of the Bobbert-Vlieger solution for particle scattering near a substrate delivering an exact solution to the scattering problem in the near field as well as far-field. By applying this

solution to study light scattering by a lipid vesicle near a lipid bilayer, whereby the lipids are represented through a biaxial optical model, we conclude through ellipsometry concepts that effective amounts of lipid-induced optical anisotropy significantly alter far field optical scattering in respect to an equivalent optical model that neglects the presence of optical anisotropy.

The taking in of matter by a living cell by invagination of its membrane to form a vacuole, *i.e.* endocytosis, and the process of vesicles budding off membranes for the transport of membrane bound secretory vesicles to the extracellular matrix, *i.e.* exocytosis, exemplify fundamental processes in biology. *In-vivo* detection of both exo- and endocytosis represents a formidable challenge to image capture technology due to the speed of the event, the size of the lipid vesicles and optical contrast available. Polarization resolved Total Internal Reflectance Fluorescence Microscopy (TIRFM) has been proven a powerful technique for the dynamic (Anantharam et al. (2010)) observation of exocytosis. In particular, TIRFM has proven capable of characterizing localized topological changes of the plasma membrane upon exocytosis. Within a different context (Hines et al. (2012)) illustrated how combined fluorescence confocal microscopy and video Differential Interference Contrast (DIC) microscopy data can jointly contribute to the study of dynamic membrane remodelling processes during nerve growth.

The image formation process of biological cells in widefield white light optical microscopy can be expected to be influenced by structured optical anisotropy caused by lipid membranes (Miranda and De Beule (2016)). An effective relation between the amount of lipid membrane optical anisotropy and optical microscopy images remains elusive and phase sensitive microscopy techniques such as *e.g.* interference microscopy imaging approaches can be expected to depend on lipid optical anisotropy, although it is not entirely clear how. Such Label-free imaging techniques have an advantage over fluorescence microscopy since they do not require the introduction of highly stable fluorescent molecules capable of reporting vesicle tracking. Furthermore, the scattering cross-sections encountered when performing label free imaging are typically several orders of magnitude higher than that of fluorescence microscopy. DIC is a widely used interference microscopy technique that makes use of orthogonal orientations of linearly polarized light to measure the interference of light originating from sample locations separated by a well-defined shear distance. It allows one to derive a linear phase map of the sample (Arnison et al. (2004)). However, providing a meaningful biophysical understanding of the contrast origin in such a phase map remains challenging (Popescu et al. (2006)). In order to fully predict the DIC microscopic image formation process, and thus link it to the state of the imaged object, it is necessary to investigate how light is scattered by optically anisotropic structures.

Here, we present the formal solution, satisfying Maxwell's equations, for light scattered by core-shell particle with an optically biaxial shell above an isotropic substrate covered with an anisotropic thin film. With apply this solution to the case of light scattering by a liposome above a lipid bilayer, embedded in an aqueous environment, taking into account the lipid induced optical anisotropy. Furthermore, we study how light scattering by such samples alters due to the presence of optical anisotropy, with the help of ellipsometric concepts. Our numerical simulations detail how far-field light scattering during cellular exo- and endocytosis is perturbed by the presence of lipid-induced optical anisotropy.

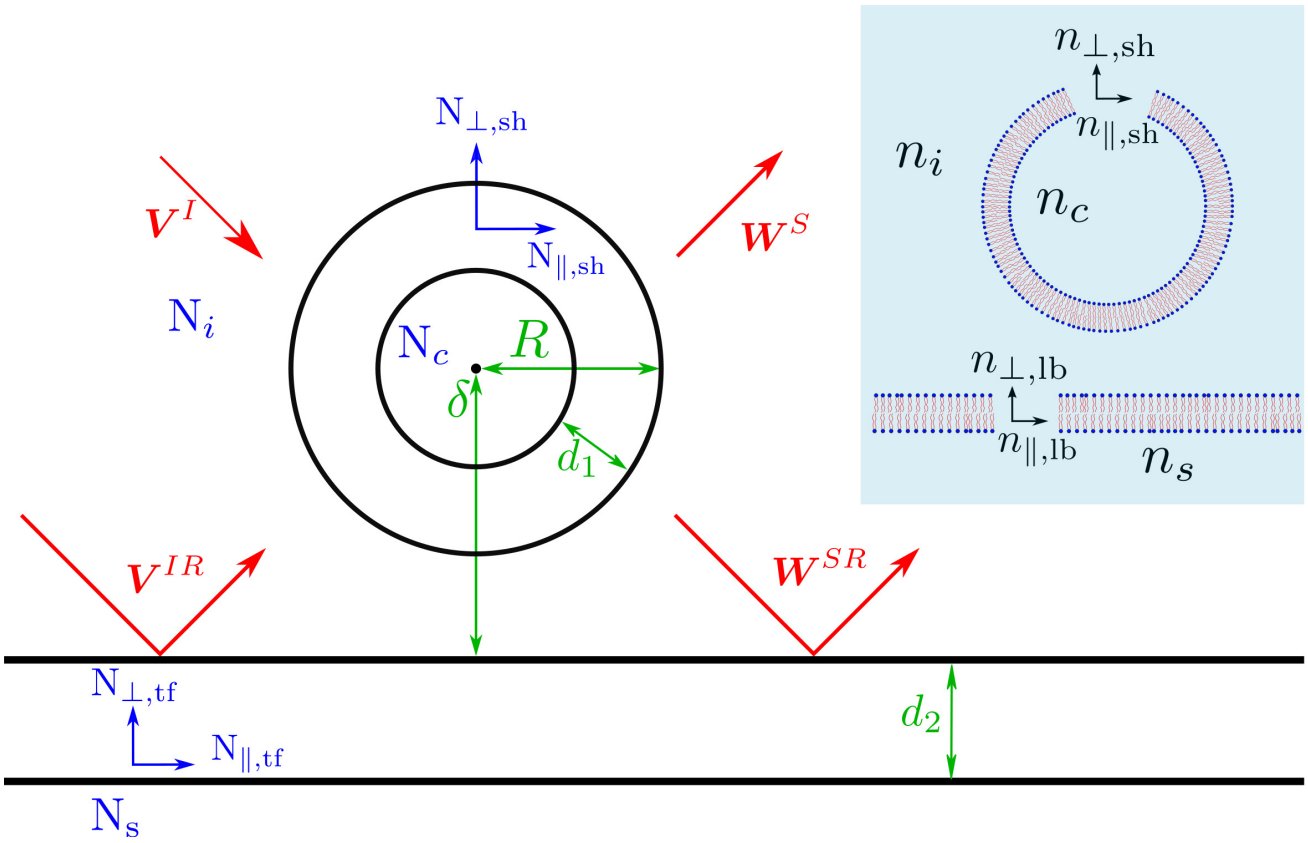

FIGURE 1 Light scattering of a core-shell particle with an optically biaxial shell near a substrate covered with an optically biaxial thin film. The electromagnetic waves represented by spherical Debye potentials are represented in red; geometrical dimensions are indicated in green and RI regions indicated in blue. The top right insert represent an equivalent model for a lipid vesicle above a lipid bilayer.

1 | LIGHT SCATTERING OF A LIPOSOME SUSPENDED ABOVE A LIPID MEMBRANE

Figure 1 depicts the general system to which we present an analytical solution: a core-shell particle consisting of a solid isotropic core characterized by the complex optical constant N_c and biaxial shell represented by complex optical constants $\mathrm{N}_{\perp,\mathrm{sh}}$ and $\mathrm{N}_{\parallel,\mathrm{sh}}$, suspended in an isotropic medium (N_i) near a substrate (N_s) covered by a biaxial thin film ($\mathrm{N}_{\perp,\mathrm{tf}}$ and $\mathrm{N}_{\parallel,\mathrm{tf}}$). Further parameters considered in our model system are overall particle radius R, particle to thin film distance δ, shell thickness d_1 and thin film thickness d_2. The solution satisfying Maxwell's equation for light scattered by a sphere near a substrate was presented by Bobbert and Vlieger in 1986 (Bobbert and Vlieger (1986)) and subsequently evaluated experimentally through ellipsometry by Bobbert *et al.* (Bobbert et al. (1986)) Their method relies on the formal solution represented by

$$\mathbf{W}^\mathbf{S} = (1 - \mathbf{B} \cdot \mathbf{A})^{-1} \cdot \mathbf{B} \cdot \left(\mathbf{V}^\mathbf{I} + \mathbf{V}^\mathbf{IR}\right), \tag{1}$$

whereby the incident and reflected waves are represented by spherical Debye potentials $\mathbf{V}^\mathbf{I}$, $\mathbf{V}^\mathbf{IR}$, $\mathbf{W}^\mathbf{S}$, and $\mathbf{W}^\mathbf{SR}$ as indicated in figure 1. Matrices **A** and **B** characterize reflection of spherical waves by the substrate and light scattering by the particle respectively. This solution was originally applied to solid spheres on an isotropic substrate. Using the

T-matrix approach, this has been extended to axisymmetric and even arbitrary shape particles (Wriedt and Doicu (1998); Doicu et al. (2000)). Also, non-homogeneous particles with isotropic and biaxial coatings (Kim et al. (2002); De Beule (2014)) have been considered. It should be noted that a simplified approximate solution has been presented by Videen (Videen (1991, 1992)), also applied in reference (Wriedt and Doicu (1998)), assuming that the scattered field reflecting off the surface and interacting with the particle is incident upon the surface at near-normal incidence. However, great care should be exercised by application of this approximation, especially for metallic particles, as pointed out by (Kim et al. (2002))

In order to establish the solution for the scattered light depicted in figure 1 we extend the solution presented in reference (De Beule (2014)) by modifying the Fresnel reflection coefficients contained within matrix **A** with the Fresnel reflection coefficient for a substrate covered with a biaxial anisotropic thin film (Fujiwara (2005)). Here, we evaluate the solution for the total light reflected from a surface density of identical core-shell particles as detailed by Bobbert *et al.* (Bobbert et al. (1986)). The numerical simulations reported below have been obtained by extending the implementation of the Bobbert-Vlieger theory found in the SCATMECH library developed by Thomas A. Germer (Germer (2015)).

A suitable optical model for cellular exo- or endocytosis representing a liposome above a lipid bilayer in an aqueous environment is represented in the top right of figure 1. The main difference with the general model is that the attenuation coefficient for all media, *i.e.* lipids and aqueous medium, is considered zero: the complex valued optical constant N therefore reduces to the real valued Refractive Index (RI) n. It should be noted that in this investigation the RI are considered non-dispersive. For the biaxial model an average RI is defined according to

$$N_{avg}^2 = \frac{2N_{\parallel}^2}{3} + \frac{N_{\perp}^2}{3} \tag{2}$$

Unless otherwise stated, all default parameters as illustrated in 1 for the modelling of sparsely seeded core-shell particles on a surface according to reference (Bobbert et al. (1986)) are listed in table 1.

TABLE 1 Default simulation parameters.

Model parameter	Value	Model Parameter	Value
θ	70°	λ	0.488 µm
$\mathcal{S}$	1 µm^{-2}	$n_i = n_s = n_c$	1.333
$n_{\parallel,\mathrm{sh}} = n_{\parallel,\mathrm{lb}}$	1.450	$n_{\perp,\mathrm{sh}} = n_{\perp,\mathrm{lb}}$	1.460
$n_{avg,\mathrm{sh}} = n_{avg,\mathrm{lb}}$	1.453	$d_{1,2}$	5 nm

In this work, we use ellipsometry concepts to link observable properties of scattered light with the microscopic optical properties of the sample. Ellipsometry typically determines the amplitude ratio of light reflected off a sample polarized parallel and perpendicular to the plane of incidence . This ratio is typically defined as

$$\tan \Psi(\lambda, \theta)\, e^{-i\Delta(\lambda,\theta)},$$

and is determined entirely by ellipsometry angles Ψ and Δ respectively

In this study, we are interested in the difference in scattering between an optical model based on an isotropic sample and an optical model taking into account the lipid induced optical anisotropy. Hence, we define ellipsometry

angles $\delta\Delta = \Delta - \Delta_{avg}$ and $\delta\Psi = \Psi - \Psi_{avg}$ as the differences ellipsometry angles for the anisotropic and isotropic (avg) optical models, respectively. In the isotropic (avg) case the ordinarily anisotropic refractive indices are all replaced by their corresponding average refractive index defined through equation 2. Furthermore, we define the ellipsometry angle differences D_Ψ and D_Δ for Angle Of Incidence (AOI) resolved ellipsometry measurements at incident angles θ_1, $\theta_1 + \delta\theta, \ldots, \theta_1 + n\delta\theta$.

$$D_\Psi = \sum_{i=1}^{n} \frac{\left|\Psi(\theta_i) - \Psi_{avg}(\theta_i)\right|}{n} \tag{3}$$

$$D_\Delta = \sum_{i=1}^{n} \frac{\left|\Delta(\theta_i) - \Delta_{avg}(\theta_i)\right|}{n} \tag{4}$$

2 | RESULTS

Figure 2 depicts modelling results D_Ψ and D_Δ in absence of the liposome, *i.e.* based on the Fresnel reflection coefficients for an isotropic substrate covered with a biaxial thin film only. We can distinguish three distinct regions according to the impact of lipid film optical anisotropy being negligible, weak and strong, respectively: 1) $n_i \sim n_s \sim n_{avg,lb}$, 2) $n_i \sim n_s \nsim n_{avg,lb}$ and 3) $n_i \nsim n_s$. We observe a maximum for D_Ψ and D_Δ when $n_i = n_s = n_{avg,lb}$. The AOI resolved spectroscopic ellipsometry curves for Ψ and Δ underlying three example points in the above mentioned regions are shown in figure 2 (bottom left) and (bottom right) respectively. Given that aqueous media have a RI of $\sim$1.33, we can conclude that the small optical anisotropy of a lipid bilayer has a relatively significant impact on the far-field scattering polarization properties, in comparison to an isotropic model equivalent. It should, however, be noted that the overall reflected intensity drops to zero in zone one where $n_i \sim n_s \sim n_{avg,lb}$ since this represents a homogeneous sample, so while the effect under investigation becomes larger it becomes increasingly challenging to observe experimentally.

Ellipsometry modelling of liposomes with radii R of 50 nm, 150 nm and 250 nm above a lipid bilayer are illustrated in figure 3 for a wavelength (top) and AOI (bottom) resolved ellipsometry respectively. For spectroscopic ellipsometry the model predicts a $\sim$2.5° Ψ shift upon consideration of the lipid bilayer optical anisotropy for light scattering at an AOI 70°, largely independent of the liposome diameter. On the contrary, optical anisotropy has a progressively stronger impact on $\Delta(\lambda)$ for larger liposome diameters. From the AOI resolved ellipsometry Ψ angle, we note that the influence of lipid-induced optical anisotropy becomes more pronounced for increasing AOI with a $\sim$1° discrepancy between anisotropic and correspondingly isotropic averaged model at an AOI of 30° as compared to $\sim$3° at AOI 80°. Several obstacles might prevent the experimental observation of the theoretically predicted curves reported by figure 3, including sample polydispersity, vesicle aggregation, Poisson statistics of the particle density, capacity to obtain well defined isotropic and anisotropic shells around a perfectly homogeneous core and other sample homogeneities. However, figure 3 does indicate a significant capacity of a small 0.01 shell anisotropy modifying the phase of a transmitted wave which is critical for the observation with interference microscopic imaging.

Finally, we show in figure 4 the evolution of ellipsometry angles Ψ and Δ for liposomes with 100 nm radius for a change in liposome to lipid bilayer distance $\delta - R$, which express the change in scattering expected to occur over the course of an exo- or endocytosis process. In accordance with Figure 3, lipid-induced optical anisotropy induces a $\sim$2° shift in Ψ. Interestingly, the ellipsometry angle Δ exhibits a sinusoidal-like behaviour with a period of $\sim$700 nm and an amplitude of $\sim$1.5°. Inclusion of the lipid optical anisotropy reduces this amplitude to $\sim$1° while maintaining the sinusoidal period. Similarly to the discussion following figure 2, figure 4 suggests that optical anisotropy plays a role in the observation of cellular exo- or endocytosis with interference microscopic imaging.

3 | CONCLUSION

We have demonstrated that small values, *i.e.* 0.01, of lipid-induced optical anisotropy alter the far-field optical scattering properties for a liposome above a lipid bilayer with respect to a corresponding all isotropic optical model based on the corresponding average RI. We achieved this through an extension to the Bobbert-Vlieger solution of particle scattering near a substrate. This work effectively demonstrates that lipid optical anisotropy can be expected to play an important role in the microscopic observation of cellular exo- or endocytosis by phase sensitive interference microscopy imaging including DIC microscopy, more recently introduced approaches relying on digital holography referred to as Quantitative Phase Imaging (QPI) (Dunn and Zicha (1993); Cuche et al. (1999)) and tomographic phase microscopy (Jin et al. (2017)). For the latter, we believe that one should be cautious with the interpretation of refractive index maps obtained using prevailing reconstruction techniques which are based upon the concept of isotropic scattering potential introduced by (Wolf (1969)):

$$\chi(x, y, z) = \beta_0^2 \left[n^2(x, y, z) - n_m^2 \right],$$

where $\beta_0^2 = 2\pi/\lambda_0$ represents the propagation constant in free space, $n(x, y, z)$ the isotropic refractive index (RI) distribution of the object and n_m the refractive index of the surrounding medium. This formulation is derived by assuming an isotropic sample RI distribution and so the impact of an anisotropic sample RI is currently not understood. Additionally, we would like to point out that, provided lipid-induced optical anisotropy is known to be temperature dependant as reported for example by (Mashaghi et al. (2008)), our work concomitantly therefore predicts that image formation of cellular exo- or endocytosis can be temperature-dependant.

Future work will focus on the integration of our scattering model with high Numerical Aperture (NA), *i.e.* high resolution, objective image formation that has been developed taking into account the full vectorial nature of the electromagnetic field near imaging focus for DIC microscopy (Munro and Török (2005)). Hereby, we aim to provide a rigorous electromagnetic framework for the observation of small liposomal vesicles through video-DIC in real-time.

ACKNOWLEDGEMENTS

We would like to thank Dr. Thomas Germer for advice on using the SCATMECH polarization modelling library.

REFERENCES

Anantharam, A., Onoa, B., Edwards, R. H., Holz, R. W. and Axelrod, D. (2010) Localized topological changes of the plasma membrane upon exocytosis visualized by polarized TIRFM. *The Journal of Cell Biology*, **188**, 415–428.

Arnison, M. R., Larkin, K. G., Sheppard, C. J. R., Smith, N. I. and Cogswell, C. J. (2004) Linear phase imaging using differential interference contrast microscopy. *Journal of Microscopy*, **214**, 7–12.

Bobbert, P. and Vlieger, J. (1986) Light scattering by a sphere on a substrate. *Physica A: Statistical Mechanics and its Applications*, **137**, 209–242.

Bobbert, P., Vlieger, J. and Greef, R. (1986) Light reflection from a substrate sparsely seeded with spheres - comparison with an ellipsometric experiment. *Physica A: Statistical Mechanics and its Applications*, **137**, 243–257. URL: `http://linkinghub.elsevier.com/retrieve/pii/0378437186900737`.

Cuche, E., Bevilacqua, F. and Depeursinge, C. (1999) Digital holography for quantitative phase-contrast imaging. *Optics Letters*,

24, 291. URL: http://www.ncbi.nlm.nih.gov/pubmed/18071483{\%}5Cnhttps://www.osapublishing.org/abstract.cfm?URI=ol-24-5-291.

De Beule, P. A. A. (2014) Surface scattering of core–shell particles with anisotropic shell. *Journal of the Optical Society of America A*, **31**, 162.

Doicu, A., Eremin, Y. and Wriedt, T. (2000) Non-axisymmetric models for light scattering from a particle on or near a plane surface. *Optics Communications*, **182**, 281–288.

Dunn, G. A. and Zicha, D. (1993) Phase-Shifting Interference Microscopy Applied to the Analysis of Cell Behavior. *Cell Behaviour : Adhesion and Motility*, **47**, 91–106.

Fujiwara, H. (2005) *Spectroscopic ellipsometry: Principles and Applications*. Tokyo: Maruzen Co. Ltd.

Germer, T. A. (2015) SCATMECH: Polarized light scattering C++ class library. URL: http://physics.nist.gov/scatmech.

Hines, J. H., Henle, S. J., Carlstrom, L. P., Abu-Rub, M. and Henley, J. R. (2012) Single vesicle imaging indicates distinct modes of rapid membrane retrieval during nerve growth. *BMC Biology*, **10**, 4.

Jin, D., Zhou, R., Yaqoob, Z. and So, P. T. C. (2017) Tomographic phase microscopy: principles and applications in bioimaging [Invited]. *Journal of the Optical Society of America B*, **34**, B64. URL: https://www.osapublishing.org/abstract.cfm?URI=josab-34-5-B64.

Kim, J. H., Ehrman, S. H., Mulholland, G. W. and Germer, T. A. (2002) Polarized light scattering by dielectric and metallic spheres on silicon wafers. *Applied Optics*, **41**, 5405.

Mashaghi, A., Swann, M., Popplewell, J., Textor, M. and Reimhult, E. (2008) Optical anisotropy of supported lipid structures probed by waveguide spectroscopy and its application to study of supported lipid bilayer formation kinetics. *Analytical Chemistry*, **80**, 3666–3676. URL: http://pubs.acs.org/doi/abs/10.1021/ac800027s.

Miranda, A. and De Beule, P. A. A. (2016) Microscopic thin film optical anisotropy imaging at the solid-liquid interface. *Review of Scientific Instruments*, **87**, 043701. URL: http://scitation.aip.org/content/aip/journal/rsi/87/4/10.1063/1.4947258.

Munro, P. R. and Török, P. (2005) Vectorial, high numerical aperture study of Nomarski's differential interference contrast microscope. *Optics Express*, **13**, 6833.

Popescu, G., Ikeda, T., Dasari, R. R. and Feld, M. S. (2006) Diffraction phase microscopy for quantifying cell structure and dynamics. *Optics Letters*, **31**, 775.

Videen, G. (1991) Light scattering from a sphere on or near a surface. *Journal of the Optical Society of America A*, **8**, 483.

— (1992) Light scattering from a sphere on or near a surface: errata. *Journal of the Optical Society of America A*, **9**, 844.

Wolf, E. (1969) Three-dimensional structure determination of semi-transparent objects from holographic data. *Optics Communications*, **1**, 153–156. URL: http://www.sciencedirect.com/science/article/pii/0030401869900522http://linkinghub.elsevier.com/retrieve/pii/0030401869900522.

Wriedt, T. and Doicu, A. (1998) Light scattering from a particle on or near a surface. *Optics Communications*, **152**, 376–384.

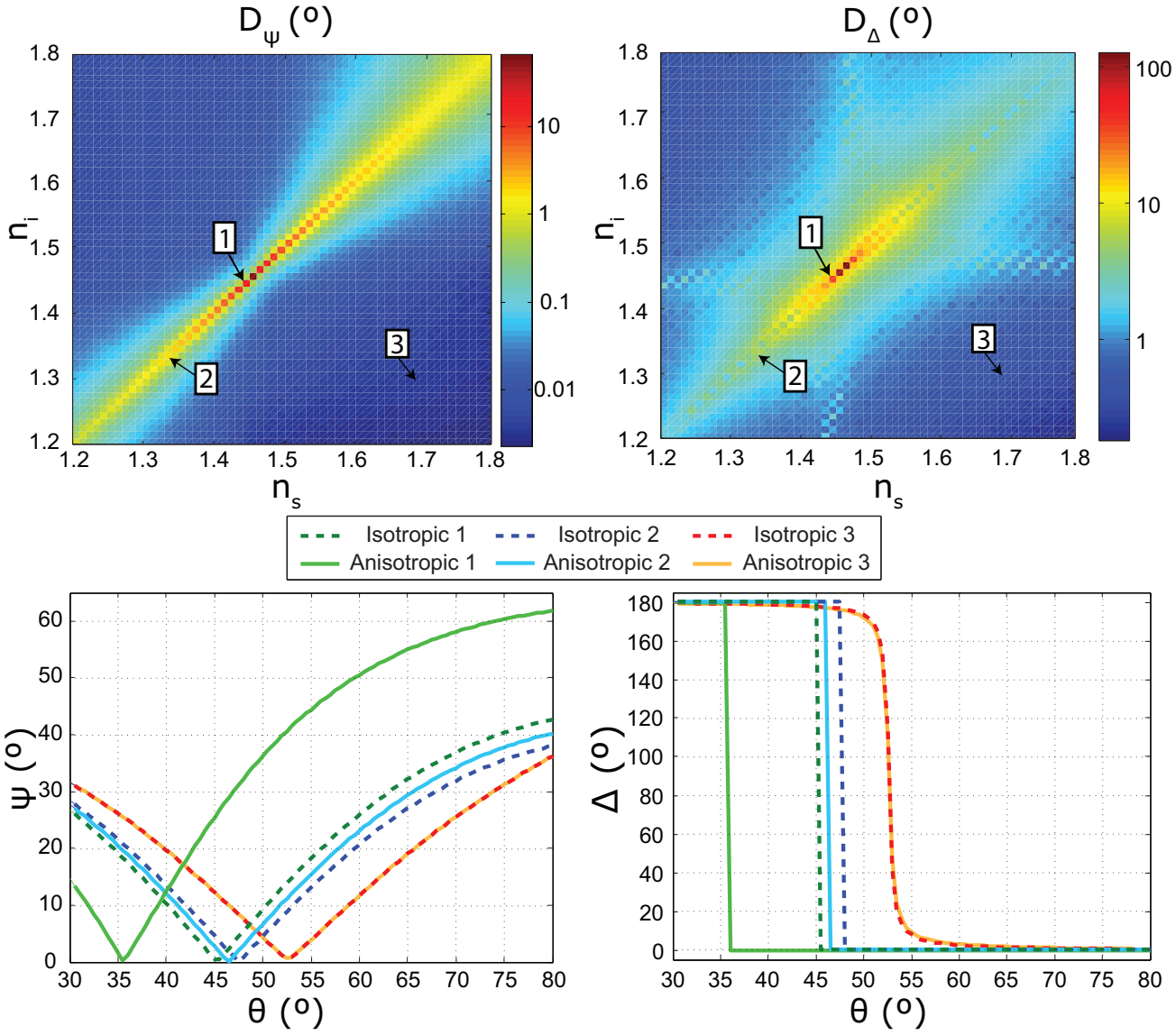

FIGURE 2 Optical modelling without presence of the lipid sphere: D_Ψ (top left) and D_Δ (top right) for AOI resolved ellipsometry from 30° to 80° for different values of the incident and substrate refractive indices respectively; AOI resolved Ψ (bottom left) and Δ (bottom right) profiles for anisotropic lipid thin film and the isotropic counterpart based on the average RI.

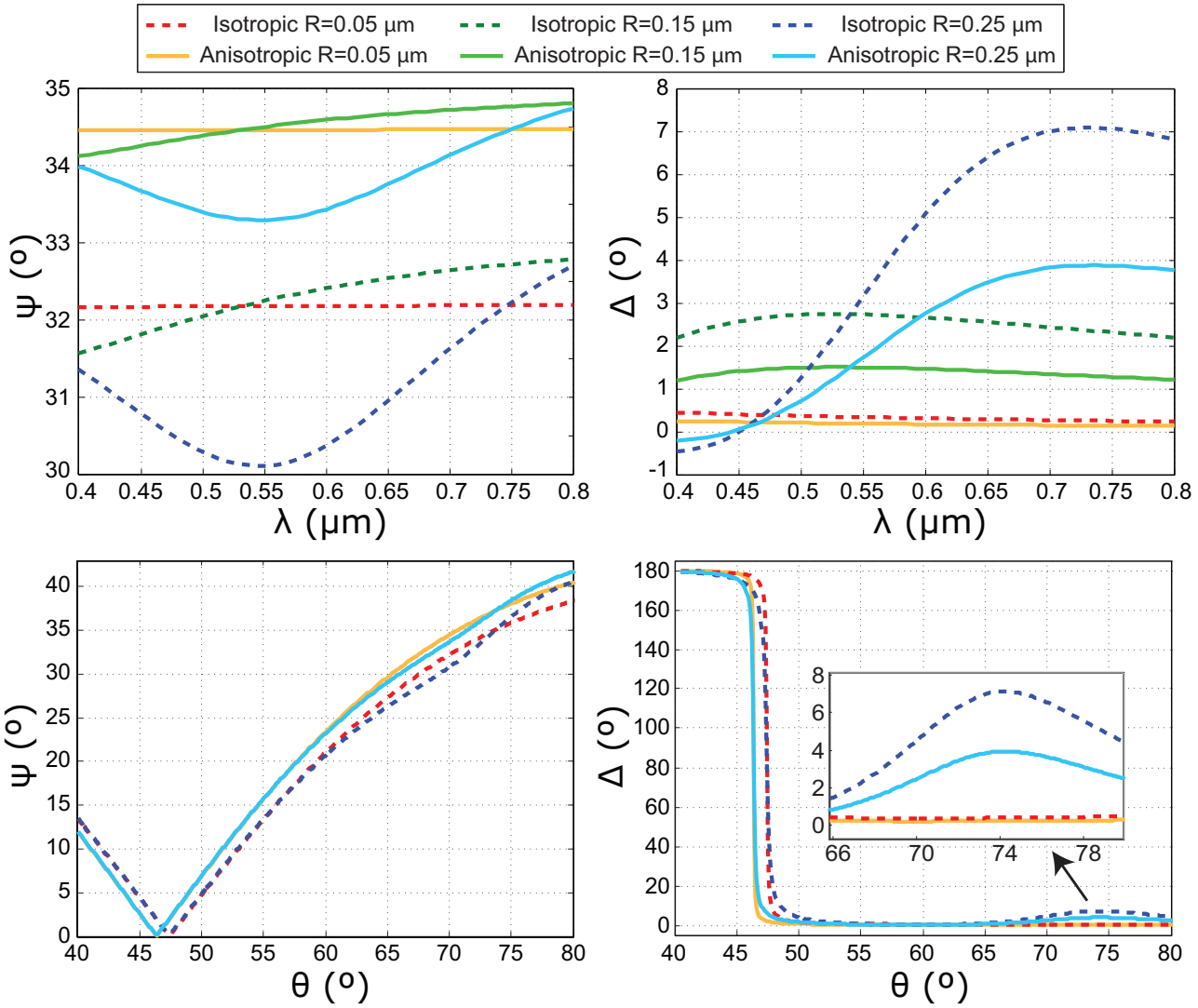

FIGURE 3 Ellipsometry angles Ψ (left) and Δ (right) for wavelength (top) and AOI (bottom) resolved ellipsometry of liposome with radii of 50 nm, 150 nm and 250 nm above a lipid bilayer ($\delta = R$). Results for R =0.15 μm have been omitted from the bottom graphs due to limited curve separation.

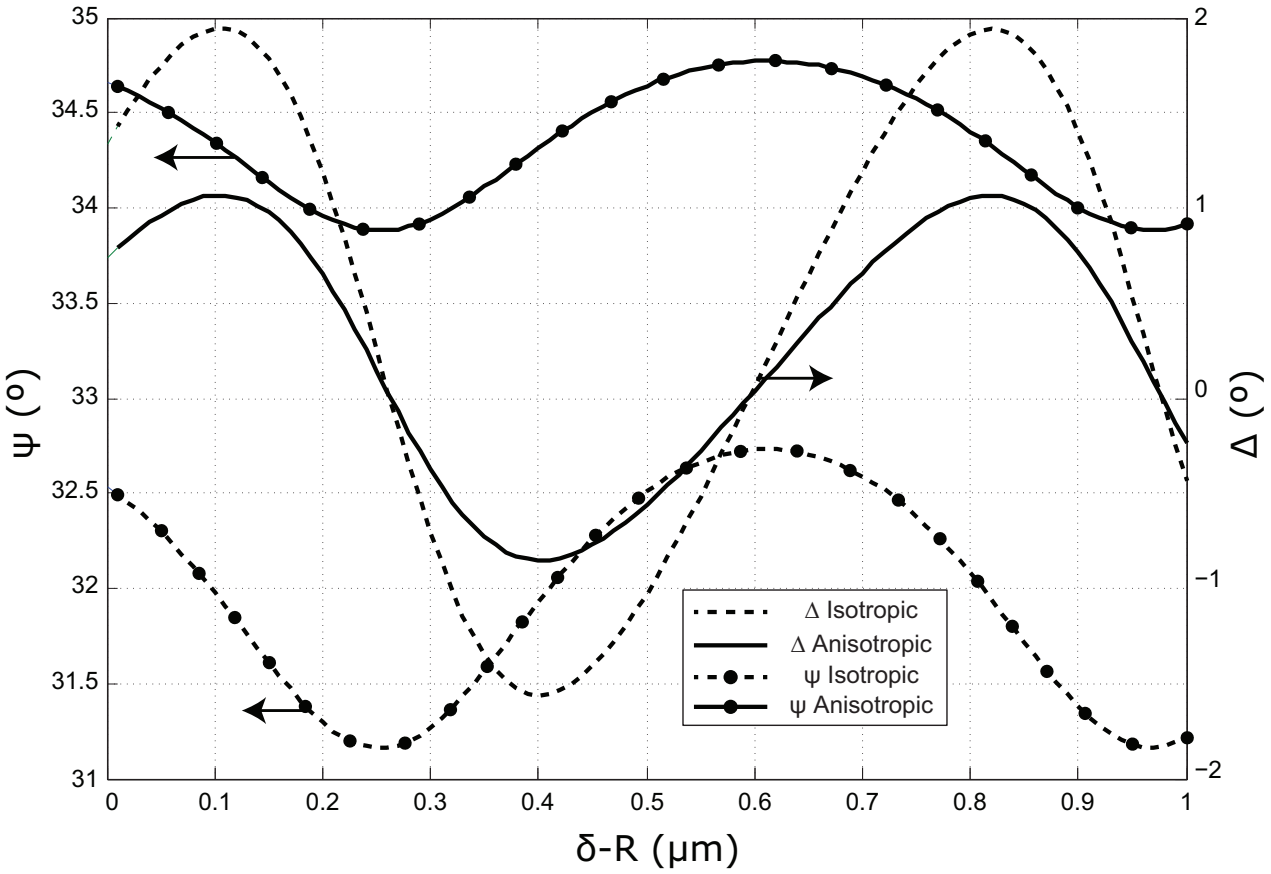

FIGURE 4 Ellipsometry angles Ψ and Δ of a liposome above a lipid bilayer for varying distance between the liposome and lipid bilayer $\delta - R$.

ANNEX I

EXPERIMENTAL PROTOCOLS

The present annex introduces the reader to the materials and experimental protocol followed by Dr A. Miranda to elaborate the coated and uncoated silica spheres used in this work. All samples were prepared with Milli-Q ultrapure water with conductivity of $18.2\,\Omega\,cm^{-1}$.

I.1 Silica spheres preparation

Materials

- Tetraethyl Orthoslication (TEOS), from Sigma-Aldrich (St. Louis, Missouri, United States);
- Ammonium Hydroxide (NH_4OH) 28%, from Sigma-Aldrich (St. Louis, Missouri, United States);
- Sodium Chloride (NaCl), from Sigma-Aldrich (St. Louis, Missouri, United States);
- N-(2-Hydroxyethil) piperazine-N-(2-ethanesulfonic acid) (HEPES), from Sigma-Aldrich (St. Louis, Missouri, United States);
- Calcium Chloride ($CaCl_2$), from Sigma-Aldrich (St. Louis, Missouri, United States);
- Milli-Q water

Protocol

Silica spheres were prepared using the Stöber method with slight modifications [53].

1. TEOS was mixed with a solution of NH_4OH and left to react at room temperature for 24 hours;

2. The particle suspension was centrifuged twice at 9000 rpm for 5 min with ethanol;
3. Then, it was centrifuged in Milli-Q water three times at 9000 rpm for 5 min;
4. The pellet was placed to dry under vacuum overnight;
5. The silica spheres obtained (0.7282 g) were resuspended in 45.5 mL of calcium buffer (150 mmol L^{-1} of NaCl, 10 mmol L^{-1} of HEPES and 2 mmol L^{-1} of $CaCl_2$);

I.2 Coated silica spheres preparation

Materials

- 1,2-dioleoyl-sn-glycero-3-phosphocholine (DOPC), from Avanti Polar Lipids, Inc. (Alabama, United States);
- 1,2-dioleoyl-sn-glycero-3-phospho-L-serine (DOPS), from Avanti Polar Lipids, Inc. (Alabama, United States);
- Silica spheres
- NaCl, from Sigma-Aldrich (St. Louis, Missouri, United States);
- HEPES, from Sigma-Aldrich (St. Louis, Missouri, United States);
- $CaCl_2$, from Sigma-Aldrich (St. Louis, Missouri, United States);

Protocol

1. DOPC and DOPS were mixed in the desired lipid ratio of 4:1 in chloroform, followed by gentle drying under a nitrogen stream and overnight vacuum drying to remove organic solvent traces;
2. Multilamellar Vesicles (MLVs) of the lipid mixture were obtained by resuspending the lipidic film in a freshly prepared calcium buffer (150 mmol L^{-1} of NaCl, 10 mmol L^{-1} of HEPES and 2 mmol L^{-1} of $CaCl_2$) in order to obtain a final concentration of 1 mg mL^{-1};
3. Frozen and thawed MLVs were obtained by repeating five time the following cycle: freezing the vesicles in liquid nitrogen, thawing the sample in a water bath at 25 °C and vortexing at 2000 rpm for 1 min;
4. Suspension was left undisturbed for 90 min at room temperature and extruded 12 times by Lipex Biomembranes extruder (Northern Lipids, Inc., Vancouver, Canada) through polycarbonate filters with different pores sizes (100 nm and 200 nm to produce Large Unilamellar Vesicles (LUVs);

5. 1 µL or 5 µL of silica spheres suspension were mixed with 100 µL or 1000 µL of LUVs suspension, vortexed for 1 min at 2000 rpm and left undisturbed in the fridge over-night;